

December 2017

Synthesis, Transport, and Thermoelectric Studies of Topological Dirac Semimetal Cd₃As₂ for Room Temperature Waste Heat Recovery and Energy Conversion

Tahereh A. Hosseini
University of Wisconsin-Milwaukee

Follow this and additional works at: <https://dc.uwm.edu/etd>

 Part of the [Electrical and Electronics Commons](#), and the [Nanoscience and Nanotechnology Commons](#)

Recommended Citation

Hosseini, Tahereh A., "Synthesis, Transport, and Thermoelectric Studies of Topological Dirac Semimetal Cd₃As₂ for Room Temperature Waste Heat Recovery and Energy Conversion" (2017). *Theses and Dissertations*. 1642.
<https://dc.uwm.edu/etd/1642>

This Dissertation is brought to you for free and open access by UWM Digital Commons. It has been accepted for inclusion in Theses and Dissertations by an authorized administrator of UWM Digital Commons. For more information, please contact open-access@uwm.edu.

SYNTHESIS, TRANSPORT, AND THERMOELECTRIC
STUDIES OF TOPOLOGICAL DIRAC SEMIMETAL CD_3AS_2 FOR
ROOM TEMPERATURE WASTE HEAT RECOVERY AND
ENERGY CONVERSION

by

Tahereh A. Hosseini

A Dissertation Submitted in
Partial Fulfillment of the
Requirements for the Degree of

Doctor of Philosophy
in Engineering

at

The University of Wisconsin – Milwaukee

December 2017

ABSTRACT

SYNTHESIS, TRANSPORT, AND THERMOELECTRIC STUDIES OF TOPOLOGICAL DIRAC SEMIMETAL Cd_3As_2 FOR ROOM TEMPERATURE WASTE HEAT RECOVERY AND ENERGY CONVERSION

by

The University of Wisconsin-Milwaukee, 2017
Under the Supervision of Professor Nikolai Kouklin

Rising rates of the energy consumption and growing concerns over the climate change worldwide have made energy efficiency an urgent problem to address. Nowadays, almost two-thirds of the energy produced by burning fossil fuels to generate electrical power is lost in the form of the heat. On this front, increasing electrical power generation through a waste heat recovery remains one of the highly promising venues of the energy research. Thermo-electric generators (TEGs) directly convert thermal energy into electrical and are the prime candidates for application in low-grade thermal energy/ waste heat recovery. The key commercial TE materials, e.g. PbTe and Bi_2Te_3 , have room temperature ZT of less than 1, whereas ZT exceeding 3 is required for a TEG to be economically viable. With the thermoelectric efficiency typically within a few percent range and a low efficiency-to-cost ratio of TEGs, there has been a resurgence in the search for new class of thermo-electric materials for developing high efficiency thermo-to-electric energy conversion systems, with phonon-glass electron-crystal materials holding the most promise.

Herein, we focus on synthesis, characterization and investigation of electrical, thermo-electrical and thermal characteristics of crystalline Cd_3As_2 , a high performance 3D topological Dirac semimetal with Dirac fermions dispersing linearly in k^3 -space and possessing one of the largest

electron mobilities known for crystalline materials, i.e. $\sim 10^4\text{-}10^5\text{cm}^2\text{V}^{-1}\text{s}^{-1}$. Suppression of carrier backscattering, ultra-high charge carrier mobility, and inherently low thermal conductivity make this semimetal a key candidate for demonstrating high, device-favorable S and in turn ZT .

In this work, a low-temperature vapor-based crystallization pathway was developed and optimized to produce free standing 2D cm-size crystals in Cd_3As_2 . Compared to the bulk crystals produced in previous studies, e.g. Piper-Polich, Bridgman, or flux method, Cd_3As_2 samples were synthesized over a considerably shorter time (only a few hours), were single crystals and highly stoichiometric. A high thermopower of up to $613\ \mu\text{V K}^{-1}$ and the electrical conductivity of $\sim 10^5\ \text{S/m}$ were registered within the temperature range of 300–400 K.

A 1ω -method based on the transfer function was applied to probe a thermal conductivity, k of Cd_3As_2 platelets. The results yield k of $\sim 2.4\ \text{W/m.K}$ in the confirmation that the thermal conductivity of Cd_3As_2 crystals is to approach the amorphous limit at the room temperature.

With its peak thermopower attained at the low temperature range of $\sim 300\text{-}400\ \text{K}$, high electrical conductivity and amorphous limit thermal conductivity, crystalline Cd_3As_2 grown via a low- T vapor based method demonstrates $ZT > 3$; the results confirm that as-produced Cd_3As_2 platelets hold a high promise and is another phonon-glass electron-crystal TE material for the development of next generation, high efficiency thermo-electric generators and refrigerators operating under normal conditions.

© Copyright by Tahereh Hosseini, 2017
All Rights Reserved

To My Beloved Parents
Dr. S. Ahmad Hosseini
and
Mrs. Felora Hojjati

TABLE OF CONTENTS

LIST OF FIGURES	vii
ACKNOWLEDGEMENTS	xi
CHAPTER	PAGE
1. Introduction to thermoelectric materials and devices	1
Thermoelectric materials for waste heat recovery	1
1.1 Thermo-electric generators vs. Carnot engines.....	3
1.2 Thermoelectricity, thermoelectric efficiency and ZT figure of merit	5
1.3 Enhancing ZT of thermoelectric materials	9
1.4 Emerging materials for thermoelectric applications	13
1.4.1 Topological materials for thermoelectric applications.....	16
1.4.2 Crystalline Cd ₃ As ₂ for thermoelectric applications.....	30
References.....	33
2. Synthesis, Structural, and Elemental characterization of crystalline Cd₃As₂ platelets	47
2.1 Background	47
2.1.1 Chemical Vapor Deposition technique.....	49
2.2 Experimental procedure	52
2.3 RESULTS AND DISCUSSION	53
2.3.1 Scanning Electron Microscopy of Cd ₃ As ₂ platelets	53
2.3.2 Energy Dispersive X-ray spectroscopy Cd ₃ As ₂ platelets	54
2.3.3 Micro-Raman spectroscopy	56
2.3.4 Transmission Electron Microscopy of Cd ₃ As ₂ platelets	57
References.....	59
3. Transport properties and Seebeck Coefficient Study of Cd₃As₂ Platelets	62
3.1 Experimental procedures	63
3.2 Results and discussions	64
3.2.1 T-dependent current-voltage measurements	64
3.2.2 T-dependent thermo-power characteristics	65
3.2.3 Calculation of the band inversion in Cd ₃ As ₂ using ambipolar heat transport model	68
References.....	72
4. Thermal conductivity measurement of Cd₃As₂ Platelets.....	74
4.1 1 ω -method for thermal conductivity measurement	77
4.2 Experimental procedure	84
4.3. Results and discussion	86
4.4. ZT-assessments	90
References.....	91
5. Summary and Future Work	94
Curriculum Vitae	97

LIST OF FIGURES

	PAGE
Figure 1-1. Potential waste heat broken down by the stream temperature range for waste heat recovery.....	2
Figure 1-2. Schematic diagram of a Carnot engine. The Carnot efficiency η_{max} is equal to the ratio of the useful work w , to the input heat Q_h	4
Figure 1-3. (a) Seebeck effect: electric potential formation in response to the temperature gradient applied along the materials. The polarity of the generated electric field depends on the type of the majority carriers in the materials as indicated by n-type (electrons) and p-type (holes) in the figure. (b) Schematic of a thermoelectric power generation module consisted of an n-type and p-type materials connected electrically in series but thermally in parallel.	6
Figure 1-4. The thermodynamic efficiency of thermoelectric materials with different ZT values and the typical efficiencies for Rankine and Stirling thermodynamic cycles in different thermal heating schemes as a function of Δt . The cold side temperature is assumed to be 298 k (25 o c). © 2014, Douglas Paul. Adapted from {thermoelectric energy harvesting, ICT - energy - concepts towards zero - power information and communication technology, Dr. Giorgos Fagas (ed.), Intech, doi: 10.5772/57092},	8
Figure 1-5. Normalized thermoelectric properties and ZT versus doping concentration at 300k for n-type $si_{80}ge_{20}$. Curves are calculated from a numerical model developed by the authors. In the figure k refers to thermal conductivity, s refers to the Seebeck coefficient, and σ refers to the electrical conductivity. Reprinted from [29] with permission. Copyright © 2009, Royal Society Of Chemistry.....	10
Figure 1-6. All-scale hierarchical architecture to achieve low lattice thermal conductivity down to theoretical limit. Reprinted from [33] with permission. Copyright © 2014, Royal Society Of Chemistry.....	11
Figure 1-7. Figure of merit ZT of current state of the art thermoelectric materials versus temperature. The dashed lines show the maximum ZT values for bulk state of the art materials, and the solid lines show recently reported ZT values, many of which were obtained in bulk nanostructured materials. ²⁹ reprinted from [29] with permission. Copyright © 2009, Royal society of chemistry.....	13
Figure 1-8. Classification of solids according to the conventional band theory. The electronic properties of materials depends on the existence of a finite band gap and the position of Fermi level with respect to the conduction and valance bands. In the conventional band theory, the energy dispersion relation $E(\vec{k})$ of solids assumes a quadratic form.....	18

Figure 1-9. (a) for a conventional band insulator, the energy of the valence band will always remain lower than that of the conduction band at all k points throughout the Brillouin zone (BZ), and the insulator is topologically trivial. (b) Schematic plot for the band inversion mechanism. Band inversion involves the energy order switching of low energy electronic bands around certain k points in the Brillouin zone. Assuming that the two bands do not couple when the SOC is absent, they must cross at certain k -points away from γ . In the presence of the spin-orbit coupling (SOC), the two bands will, in general, couple together and open up a gap at the crossing point. As a result, the system becomes an insulator. Reprinted from [105] with permission. Copyright © 2014, Materials Research Society.19

Figure 1-10. (a) two-dimensional electron system in a perpendicular external magnetic field b forming a quantum hall system; (b) the electronic band structure of a quantum hall system. A single edge state connects the valence band to the conduction band.....21

Figure 1-11. (a) the quantum-spin hall system can be viewed as two copies of the quantum hall system with an intrinsic effective magnetic field B_{eff} that points in the opposite directions for the up- and down- spin species. (b) The electronic band structure of a quantum spin hall system. Each quantum hall subsystem shares a single edge state resulting in a pair of edge-states in a zero magnetic field.....22

Figure 1-12. Schematic of a 3d topological insulator. 3D tis support protected Dirac-like propagating states on the surface while the inner part of the system behaves as an insulator. Reprinted from [143] with permission. Copyright ©2013 the physical society of japan.....24

Figure 1-13. (Left) plot of the dispersion relation, E_k , for the surface-states of a 3d TI. E_k takes the form of cone. (Right) example of the Kramer’s pair on a constant-energy line arrows illustrate the locking of momentum k and spin s vectors.24

Figure 1-14. A conceptual diagram of the electronic band structure in different phases. In a topological insulator an energy gap opens in the bulk region. In Dirac semimetals the bulk conduction and valence bands touch only at discrete (Dirac) points and disperse linearly along all three momentum directions leading to the formation of 3d Dirac fermions.....27

Figure 1-15. (a) carbon atoms in graphene form a honeycomb lattice with two atoms in the unit cell. The first Brillouin zone of the reciprocal lattice contains two nonequivalent Dirac points, k and k' . The relevant states at the Fermi level form two touching cones with the tips at k and k' . (b) each of the two equivalent carbon atoms within one unit cell of graphene contributes one cosine-shaped band to the electronic structure that cross exactly at the Fermi level forming a Dirac cone with a linear electronic dispersion. Reprinted from [171] with permission. Copyright ©2009 American physical society.28

Figure 1-16. Schematic electronic structures showing the location of 3d Dirac cones in the Brillouin zone in (a) cd_3as_2 , and (b) na_3bi . Reprinted from [178] with permission. Copyright ©2015 American physical society.29

Figure 1-17. Brillouin zone symmetry and 3d Dirac cone. (a) cd_3as_2 crystalizes in a tetragonal body center structure with space group of $i41cd$, which has 32 number of formula units in the unit cell. The tetragonal structure has lattice constant of $a \frac{1}{4} 12.670 \text{ \AA}$, $b \frac{1}{4} 12.670 \text{ \AA}$ and $c \frac{1}{4} 25.480 \text{ \AA}$. (b) the basic structure unit is a four corner-sharing cdas_3 -trigonal pyramid. Reprinted from [170] with permission. Copyright ©2013 American physical society (c) the bulk BZ and the projected surface BZ along the (001) direction. The red crossings locate at $(k_x, k_y, k_z) \frac{1}{4} (0, 0, 0.15(2p)/(c^*))$ ($c^* \frac{1}{4} c/a$). They denote the two special k points along the g z momentum space cut-direction, where 3d Dirac band-touching points are protected by the crystalline c_4 symmetry along the k_z axis. (d) the band structure of cd_3as_2 . A band inversion occurs around the γ -point with the s state (red solid cycle) lower than the p states, resulting in the nontrivial topology. The band structure is semimetallic with a band crossing along the γ -z direction. Reprinted from [186] with permission. Copyright © 2014, Rights managed by nature publishing group..31

Figure. 2-1. Schematic of the CVD furnace horizontal tube and T-profile..52

Figure 2-2. SEM images of the platelets grown by low- T CVD with panels a–c showing different stages of secondary platelet growth initiated along the sidewalls..54

Figure 2-3. Left: site-selected EDS spectra of cd_3as_2 platelets; middle: low-magnification SEM image of the platelet; right: cd composition taken along the main axis of the platelet.....55

Figure 2-4. Room-temperature Raman spectrum of Cd_3As_2 platelet; the inset shows Raman spectrum of the cd_3as_2 target.57

Figure 2-5. a,b) low- and high-resolution tem images of the platelet; c) a corresponding SAED pattern..58

Figure 3-1. Schematic of device configuration for transport measurements. The Cd_3As_2 platelet was placed across a $\sim 5 \text{ mm}$ gap formed by two in electrodes.63

Figure 3-2. The measurement setup used for thermopower (s) measurement of cd_3as_2 which consists of a cw-IR laser source, Janis closed-cycle cryostat system with optical access window operating under various vacuum conditions. The measurements were carried out at temperature range of $\sim 220\text{-}620 \text{ k}$ in vacuum. A t -differential of $\sim 5\text{k}$ was induced by illuminating one side of the sample with cw-1064 nm solid-state laser and the i - v data was collected at each temperature.64

Figure 3-3. a) Typical I – V characteristics of cd_3as_2 platelet (sample a) obtained in a temperature range of $\sim 220\text{-}620\text{k}$; b) electrical conductance vs. T for samples a and b. The monotonic decay of the conductance with t in both platelets is typical of both semimetals and degenerately doped semiconductors.65

Figure 3-4. The Seebeck coefficient was calculated by extracting the thermoelectric voltage from the I-V data collected from the sample while inducing a T-differential of $\sim 5\text{K}$ across the sample using cw-1064 nm solid-state laser.66

Figure 3-5. Magnitude of Seebeck coefficient vs. T . The $S < 0$ indicates that the samples were n-type doped in line with the reported results in previous studies. The dashed line is the ambipolar model fit to the experimental data of platelet B.....67

Figure 4-1. Illustration of the four-probe suspended wire (SW) configuration for measuring the thermal conductivity of a Cd_3As_2 platelet. The platelet is heat sunk to the glass substrate through the four electric contacts, but the part in between the two voltage contacts needs to be suspended, to allow the temperature variation. 82

Figure 4-2. The diagram of the experimental setup for measuring the 1ω voltage. A voltage source was used to approximate a current source.....85

Figure 4-3. The 1ω voltage across the platinum wire sample in a suspended wire (sw) configuration. The solid lines are the theoretical solution obtained from the best approximation to the actual transfer function, and the points are the experimental data at 300 k. From this data, the value of the thermal conductivity of platinum wire calculated to be $\sim 66.7 \text{ W/mK}$, compared with the literature reported value of 71.4 W/mK87

Figure 4-4. The 1ω voltage across the cd_3as_2 sample in a suspended wire (SW) configuration. The solid lines are the theoretical solution obtained from the best approximation to the actual transfer function, and the points are the experimental data at 300 K. From this data, the value of the thermal conductivity of platinum wire calculated to $\sim 2.4 \text{ W/mK}$. This value is well within the range reported in literature for thermal conductivity of crystalline Cd_3As_289

Figure 4-5. ZT versus t plot for platelets A and B considering a conservative thermal conductivity of $k \approx 8.0 \text{ w/km}$ based on previous studies. The ZT peaks for platelets A and B are around ~ 3.4 and ~ 0.2 respectively90

ACKNOWLEDGMENTS

This work would not have been possible without the support and courage I received from my advisor, my committee members, my beloved family, and my friends.

I would like to express my deepest gratitude to my advisor, Dr. Nikolai Kouklin, for his exemplary guidance, caring, patience, and for providing me with an excellent atmosphere for doing research. I would never forget my very first meeting with Dr. Kouklin in his office that started by my statement of interest in doing research in his lab and finished by a tour of his lab and a date to start my work. He made my dream of studying and doing research in the field of nanotechnology come true, and I definitely owe a major part of my academic and life achievements to him.

I would like to thank my committee members, Dr. Junhong Chen, Dr. Benjamin Church, Dr. Mahsa Ranji, and Dr. Chiu Law for their valuable insights and constructive feedback. I would also like to extend my appreciation to Professor Arash Mafi whose exemplary intellect and demeanor always inspired me, and his classes have been among the most enriching learning experiences I have had in my life. I also thank Dr. Steven Hardcastle for his experimental advice, and for making the Advance Analysis Facility accessible and user friendly.

My deepest and most heartfelt gratitude is to my beloved parents, Dr. S. Ahmad Hosseini and Mrs. Felora Hojjati for their endless, unconditional support, their loving encouragement, and for inspiring me to reach for my goals without hesitation. I would not have been able to reach this milestone in my life if it were not because of their ongoing confidence and devotion.

I am so grateful for my sisters, Saba and Tayyebah, for being always encouraging and supporting, for adding the delight of their presence to my life, and for being beside me through thick and thin.

My sincere appreciation goes to my partner in crime, my best friend, my husband Dr. Amin Mojtahedi, who has been always there for me. I am so glad that we shared every single moment of this journey and get to celebrate our accomplishments together. He never ceases to amaze me with his creative, bright, and deliberate mind.

I would also like to thank my friends and lab partners, Jacob Alward, Casey Marnocha, Niloufar Yavarishad, and Elaheh Kheieandish for their assistance and help throughout my PhD research.

At last, but not least, I would like to acknowledge the generous support of Johnson Controls Inc. for offering me a three-year research fellowship and for sponsoring my PhD research.

Chapter 1.

Introduction to thermoelectric materials and devices

Thermoelectric materials for waste heat recovery

The increasing rate of global energy consumption and the requirements for clean energy without the emission of additional greenhouse gases have sparked significant research into the alternative clean and renewable energy sources. In today's world, a full two-thirds of the fuel burned to generate power is lost in the form of heat^{1,2}. All heat-power conversion systems produce waste heat, which is fundamental to the laws of thermodynamics.^{3,4} Capturing this waste heat not only will lower the environmental pollution and save natural resources, but it will also reduce demand for the primary energy as more power output can be achieved at the same amount of fuel. A successful technical solution to the waste heat recovery problem is critically sensitive to the temperature of the waste heat as well as underlying economics, i.e. cost aspects. In general, the waste heat sources can be divided into high temperature (500—1200°C), medium temperature (250—500°C) and low temperature (80—250°C) ones.^{5,6,7}

As indicated in Fig. 1-1, almost 90% of the generated waste heat has a temperature below 650 °C, and only 10% falls within the high-temperature portion of the waste heat stream.

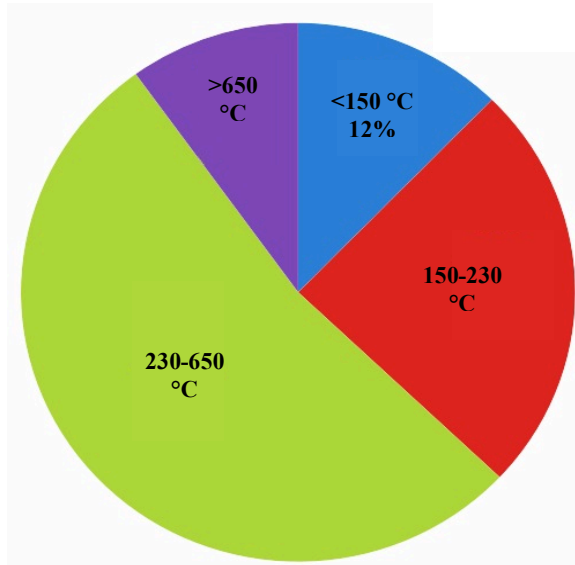


Figure 1-1. Potential waste heat broken down by the stream temperature range for waste heat recovery.

High temperature waste heat is often re-used to perform work, to heat up buildings and to drive industrial processes. The recovery of medium-temperature waste heat can be also done successfully^{8,9} by implementing external combustion engines¹⁰ (e.g. Stirling and Ericsson), Kalina Cycle^{11,12}, and through Organic Rankine Cycle (ORC)¹³⁻¹⁸. However, most of low-temperature waste heat is either discarded in cooling towers or directly to the atmosphere, or discharged into the sewer.⁵

The development of high efficiency thermoelectric materials is one of the important research directions for low-grade thermal energy/waste heat utilization. The thermoelectric effect refers to the phenomenon of the direct conversion of temperature differences to electric voltage and vice versa. Thermoelectric generators can be used for converting heat generated by many sources, such as power plants, solar radiation, automotive exhaust, and industrial processes, to electricity. Thermoelectric coolers can also be used to make refrigerators and other cooling systems. These solid-stated devices demonstrate several critical advantages over other power

generators as they are silent, very reliable, and compact/lightweight, which make them attractive for several niche deployments including transportation, space power generation¹⁹, electronics cooling, and thermo-voltaic cells. Yet, thermoelectric generators with typical efficiency of only ~5%–8% demonstrate poor efficiency-to-cost ratio, and the problem stems mainly from the poor conversion characteristics of the thermoelectric (TE) materials themselves. Therefore, improving thermoelectric efficiency becomes the key issue in this research field.

In the following sections, a more detailed review of thermoelectric materials is provided. The thermodynamic efficiency of TE generators with reference to Carnot efficiency is derived, and the methods and approaches to enhance the thermoelectric performance of materials are reviewed. In section 2, topological materials as an emerging class of matter in condensed matter physics are introduced, and their potential for thermoelectric applications is reviewed. Among the materials belonging to this class, the potential of crystalline Cd_3As_2 , the most stable Dirac semimetal, for high-performance thermoelectric applications is investigated and discussed.

1.1 Thermoelectric Generators vs. Carnot Engines

In order to discuss the thermodynamic efficiency of thermoelectric generators, first we need to review the Carnot cycle efficiency as it is the maximum efficiency for converting a given amount of thermal energy into work.^{20–22} The Carnot efficiency will set a maximum amount for any thermal system and will determine the scope for improving the efficiency of thermoelectric materials.

The Carnot cycle is a theoretical thermodynamic cycle consisting of two reversible isothermal processes and two reversible adiabatic processes.^{20,23–25} The reversibility of the processes in a

Carnot engine makes it the most efficient heat engine allowed by the second law of thermodynamics, and places constraints upon the direction of heat transfer and the attainable efficiencies of all heat engines. According to the second law of thermodynamics, (the Kelvin-Planck statement²⁴) it is impossible to extract an amount of heat Q_H from a hot reservoir and use it all to do work W . Some amount of heat Q_C must be exhausted to a cold reservoir. This precludes a perfect heat engine. The Carnot efficiency η_{max} is equal to the ratio of the useful work W , to the input heat Q_H . It can be also written in terms of the input temperature T_H and the exhaust temperature T_C . The schematic diagram of the Carnot engine and the equation for its efficiency are given in Fig. 1-2.

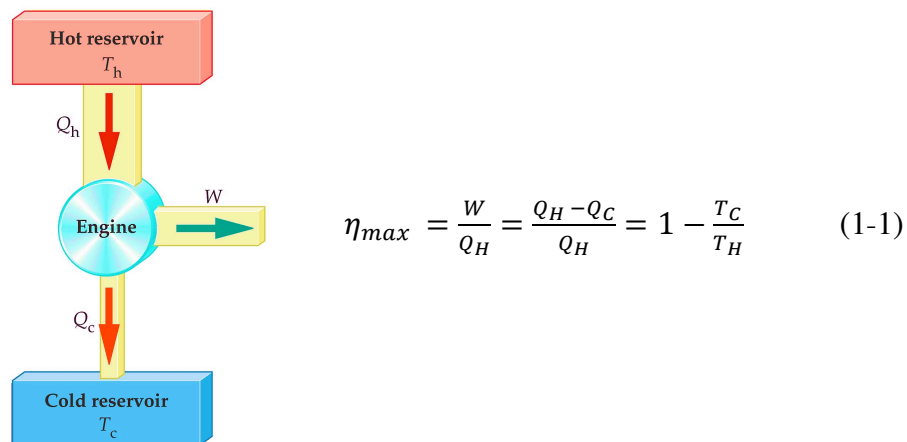


Figure 1-2. Schematic diagram of a Carnot Engine. The Carnot efficiency η_{max} is equal to the ratio of the useful work W , to the input heat Q_H .

As equation (1-1) implies, the efficiency of a heat engine is limited by the highest and the lowest temperature of the system. The minimum temperature is usually set by the air temperature at the inlet to the engine, and the maximum temperature in the cycle is limited by metallurgical conditions. For example, the blades of a gas turbine cannot sustain temperatures above 1300 K^{26,27}, and higher temperatures up to 1600 K can only be obtained with ceramic turbine blades. The need for materials that can withstand high temperatures will significantly increase the cost of

the system which will negatively affect the efficiency-to-cost ratio. Therefore, there is a compromise between the thermodynamic efficiency of a system and the economics involved.

The efficiency of waste heat recovery systems is also limited by the Carnot efficiency. The efficiency of power generation from waste heat is heavily dependent on the temperature of the waste heat stream. It is usually more economic to re-use the medium- to high-temperature portions of the stream (i.e. > 500 F°). Thermoelectric (TE) modules can provide solutions to many difficult thermal management problems especially in the case of small-scale applications where a low to moderate heat source must be handled. As will be discussed in the next section, the TE performance is routinely assessed based on the figure of merit, ZT . The larger the figure of merit, the better the efficiency of the thermoelectric cooler or power generator.

1.2 Thermoelectricity, ZT figure of merit, and the Thermoelectric efficiency

There are three well-known major effects involved in the thermoelectric phenomenon: the Seebeck, Peltier, and Thomson effects. The Seebeck effect, first discovered by Thomas Johann Seebeck in 1821, refers to the generation of an electromotive force by a temperature differential or gradient. When a temperature gradient ΔT is applied along a conductive material, the free charge carriers (such as electrons in metal or n-Si) at the hot side of the material have higher energy than the carriers at the cold side, causing a net diffusion of charge carriers to the cold side. As the hot charges diffuse away, eventually, there will be more mobile carriers at the cold side than the hot side and an electric field will form. At equilibrium (open circuit regime) the carrier diffusion rate from the hot side to the cold side will become equal to that from the cold side to the hot side due to this electric field. Thus, as illustrated in Fig. 1-3(a), in equilibrium an electrochemical potential will form in response to a temperature gradient along the slab. This

electrochemical potential is known as the Seebeck voltage; and the amount of voltage generated at temperature difference of 1 K is called the Seebeck coefficient, $S = \Delta V / \Delta T$. If the material is connected to a circuit, the electrochemical potential will drive a current that can be used to perform electrical work. This phenomenon is called “thermoelectricity”, and it is the basis of thermoelectric power generation. The Peltier effect is the reverse of the Seebeck effect – it refers to the temperature difference induced by voltage gradient. The Thomson effect relates the reversible thermal gradient and electric field in a homogeneous conductor.

A thermoelectric module requires two thermoelectric materials to function: an n-type and a p-type semiconductor. This is so that a continuous circuit can be made whereby current can flow and power can be produced. With only one type of thermoelectric material, a voltage would be induced but current would never flow. The n-type and p-type semiconductors together form a thermoelectric “couple,” but do not form a p-n junction. They must be configured within the module such that they are electrically in series, but thermally in parallel as depicted in Fig. 1-3 (b).

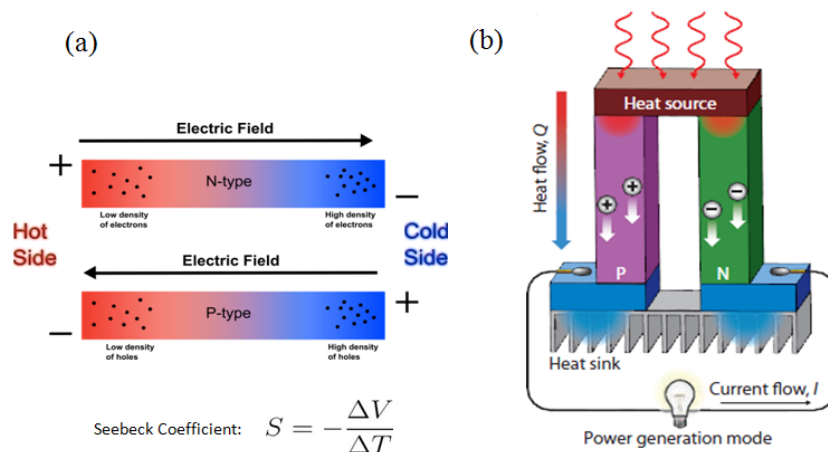


Figure 1-3. (a) Seebeck effect: Electric potential formation in response to the temperature gradient applied along the materials. The polarity of the generated electric field depends on the type of the majority carriers in the materials as indicated by n-type (electrons) and p-type (holes) in the figure. (b) Schematic of a thermoelectric power generation module consisted of an n-type and p-type materials connected electrically in series but thermally in parallel.

The key parameter that defines the efficiency of TEG is the thermoelectric dimensionless figure of merit ZT . ZT is primarily dependent on three physical properties: thermal conductivity (k), electrical conductivity (σ), and Seebeck coefficient (S). ZT equation is given by

$$ZT = \frac{S^2\sigma}{\kappa} T \quad (1-2)$$

Here, $T = (\frac{1}{2})(T_C + T_H)$ is the average temperature with T_H and T_C being the temperature of the hot and cold sides, respectively. The quantity $S^2\sigma$ is known as the power factor. For a high ZT thermoelectric material, a large power factor $S^2\sigma$ and a low thermal conductivity k is required.

To derive the thermodynamic efficiency of a thermoelectric generator, we need to build a circuit that can deliver power to a load, as illustrated in Fig. 1-3(b). In this case, a resistor R_L is used as the circuit load. The thermodynamic efficiency of the thermoelectric generator is given by

$$\eta = \frac{\text{Power supplied to the load}}{\text{Heat absorbed at hot junction}} \quad (1-3)$$

The power supplied to the load is just the Joule heating of the load resistor R_L which is equal to I^2R_L . The heat absorbed at the hot junction is the Peltier term plus the heat withdrawn from the hot junction as described. By combining these terms and assuming that the power supplied to the load is only through Joule heating, it can be shown that the maximum efficiency of a TE module for electricity generation is²⁸:

$$\eta_{max} = \left(1 - \frac{T_c}{T_h}\right) \frac{\sqrt{1 + ZT} - 1}{\sqrt{1 + ZT} + \frac{T_c}{T_h}} \quad (1-4)$$

Where T_H is the temperature at the hot junction, T_C is the temperature at the surface being cooled, and ZT is the figure of merit for thermoelectrics as given in equation (1-2).

As can be seen, the first term in Eq. (1-4) is the familiar term for the Carnot efficiency, which puts a limit on the maximum possible efficiency of thermoelectric materials. The second part accounts for losses and irreversible processes, which reduce as the dimensionless figure of merit ZT increases in value.

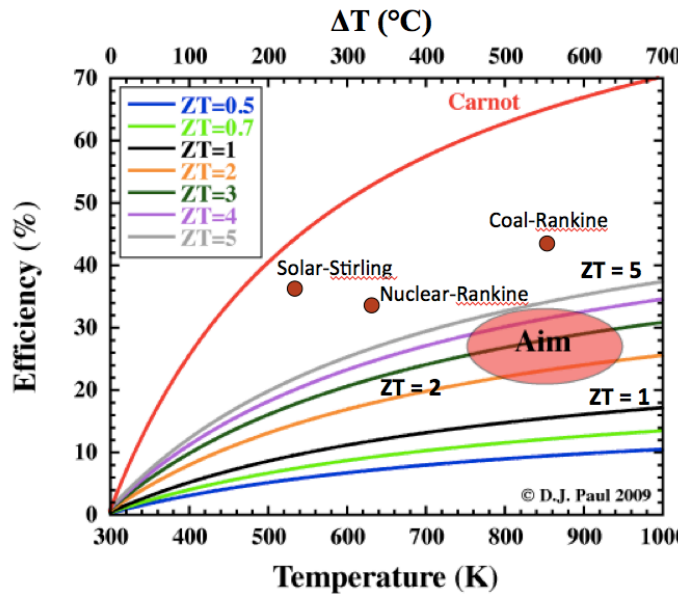


Figure 1-4. The thermodynamic efficiency of thermoelectric materials with different ZT values and the typical efficiencies for Rankine and Stirling thermodynamic cycles in different thermal heating schemes as a function of ΔT . The cold side temperature is assumed to be 298 K (25 °C). © 2014, Douglas Paul. Adapted from {Thermoelectric Energy Harvesting, ICT - Energy - Concepts Towards Zero - Power Information and Communication Technology, Dr. Giorgos Fagas (Ed.), InTech, DOI: 10.5772/57092}

Fig. 1-4 demonstrates the maximum thermoelectric efficiencies for different ZT s and the typical efficiencies for other thermodynamic cycles as a function of ΔT . As seen, today's thermoelectric

generators, with the thermodynamic efficiency of $\sim 8\text{-}12\%$ ($\cong ZT < 1$), have significantly less efficiency than other power generation technologies based on Rankine or Stirling cycles ($\eta > 30\%$). Most of thermodynamic cycles used in thermal power plants are suitable for power generation at the large scales (fluids become more viscous or lossy below a certain length scale decreasing the total efficiency of the cycle). Hence, for small-scale power generation, e.g. below ~ 100 W, thermoelectrics offer some advantages over other thermal cycles. In addition to being flexible in size, they have no moving mechanical parts and are significantly more reliable than other heat engines that usually require the installation of additional equipment such as compressors and turbines.

Thus, it is of an utmost advantage to have thermoelectric materials with higher efficiencies. According to Eq. (1-4), in order to increase the efficiency of a TE generator, one needs to improve the ZT figure of merit of the TE materials in that module. Currently, the goal for having advanced TE materials is set at a ZT of ~ 2 ($\eta \approx 20\%$); however, to be competitive with other power generation technologies, a ZT of higher than 3 is desired. Several approaches for increasing the ZT of thermoelectric materials are reviewed in the following section.

1.3 Enhancing ZT of thermoelectric materials

In order to achieve high-performance TE materials with a high ZT, a combination of a high power factor ($S^2\sigma$) and a low thermal conductivity is required. Despite having multiple parameters to adjust to get a higher ZT, optimizing all the parameters together cannot be achieved easily since the electrical and thermal parameters in bulk materials are coupled through the Wiedemann-Franz law given by $\sigma T/k = (3/\pi)^2 (q/k_B)^2$, where q is the carrier charge and k_B is Boltzmann constant. As a result, simply improving one parameter does not necessarily result in

higher ZT. For example, if the electrical conductivity of a material is too low, we might want to increase the carrier concentration; however, increasing the carrier concentration will decrease the Seebeck coefficient and also increase the electronic contribution to the thermal conductivity. Fig. 1-5 illustrates these conflicting trends for n-type $\text{Si}_{80}\text{Ge}_{20}$ at 300 K.²⁹ These changes in properties will not lead to a net increase in ZT as any changes in favor of one property is accompanied by an unfavorable change in the other properties.

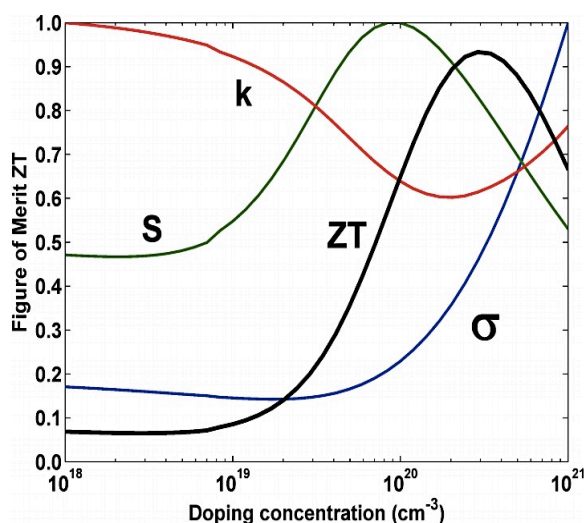


Figure 1-5. Normalized thermoelectric properties and ZT versus doping concentration at 300K for n-type $\text{Si}_{80}\text{Ge}_{20}$. Curves are calculated from a numerical model developed by the authors. In the figure k refers to thermal conductivity, S refers to the Seebeck coefficient, and σ refers to the electrical conductivity. Reprinted from [29] with permission. Copyright © 2009, Royal Society of Chemistry.

Therefore, alternative approaches for enhancing ZT of TE materials are required. Until recently, a primary pathway to enhancing ZT was centered on the idea of slowing the heat diffusion. This was done by decoupling the lattice thermal conductivity, k_L , from the electronic thermal conductivity, k_e through introducing phonon scattering interfaces and rattling centers^{30,31}. For an optimum result, all phonons with short, medium, and long mean free path (MFP) must be targeted. The point defects created through the introduction of dopant atoms on lattice sites

defects can scatter short MFP phonons due to either mass contrast or local bond strain induced by the defects.³² The scattering of medium MFP phonons is best achieved through nanostructuring. In this case, scattering occurs at the interfaces between the precipitates and the matrix and from the mass contrast between the two phases. To scatter the long MFP phonons additional mechanisms are needed. This is usually achieved through introduction of mesoscale grain boundaries by breaking down the crystals of samples to mesoscopic particles in the range of 100 nm to 5 μm. The finite size in a given grain can limit the propagation of phonons with long MFP.³³ To scatter all MFP ranges from nano- to micro-length scales, all of the above techniques must be integrated in a single sample to make an all-scale hierarchical architecture, as shown in Fig. 1-6. Such material architecture has the potential to significantly reduce the thermal conductivity down to the minimum theoretical limit.

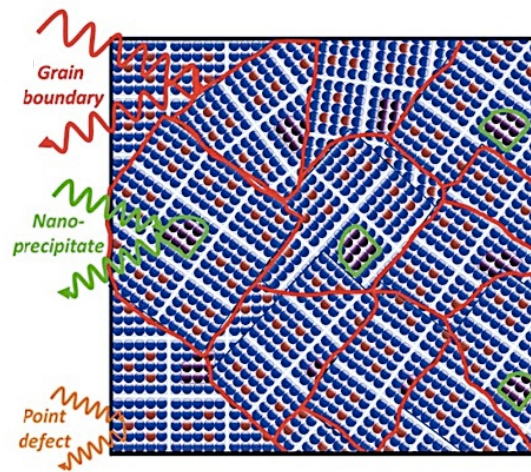


Figure 1-6. All-scale hierarchical architecture to achieve low lattice thermal conductivity down to theoretical limit. Reprinted from [33] with permission. Copyright © 2014, Royal Society of Chemistry.

With the lattice thermal conductivity, k_L already approaching the fundamental (amorphous materials) limit, the focus has shifted toward optimizing the TE power factor $S^2\sigma$, by modifying the density of states, band structure engineering, and by means of quantum confinement.^{34–36}

Recent advances in creating nanostructured materials such as superlattices, quantum dots, nanowires, and nano-composites have made remarkable progress in the field of thermoelectrics²⁹. These materials are able to obtain enhancements in thermoelectric properties, which cannot be achieved in traditional bulk materials. Exploiting nanoscale effects would result in large increases in the thermoelectric figure of merit, ZT . This is possible because at lower dimensional structures, the Wiedemann-Franz rule breaks down and quantum effects can be used to optimize the ZT value.^{28,29} Dresselhaus's pioneering work³⁴ has shed light on various low-dimensional systems, including superlattices, nanowires and quantum dots. Venkatasubramanian et al³⁷ reported $\text{Bi}_2\text{Te}_3/\text{Sb}_2\text{Te}_3$ superlattices with a high- ZT value of up to 2.4. Subsequently, Harman et al.³⁸ reported $\text{PbTe}/\text{PbTeSe}$ quantum dot superlattices with a ZT value of greater than 3.0 at 600 K.

While record high ZT values of 2 were achieved in lower dimensional structures, the slow fabrication process along with the high cost of mass production have made these nanostructured materials impractical for commercial applications. As a result, bulk nanostructured materials have become demanding new break-through in thermoelectric materials and device engineering^{29,39}. These materials are fabricated using a bulk process rather than a nanofabrication process, and could be produced in large quantities, making them a suitable fit to commercial setting. Fig.1-7 shows the figure of merit ZT for the current state of the art thermoelectric materials versus temperature. As seen, the reported ZT values for bulk nanostructured materials are improved compared with their bulk counterparts, and the highest ZT obtained at room temperatures slightly exceeds 1.5.

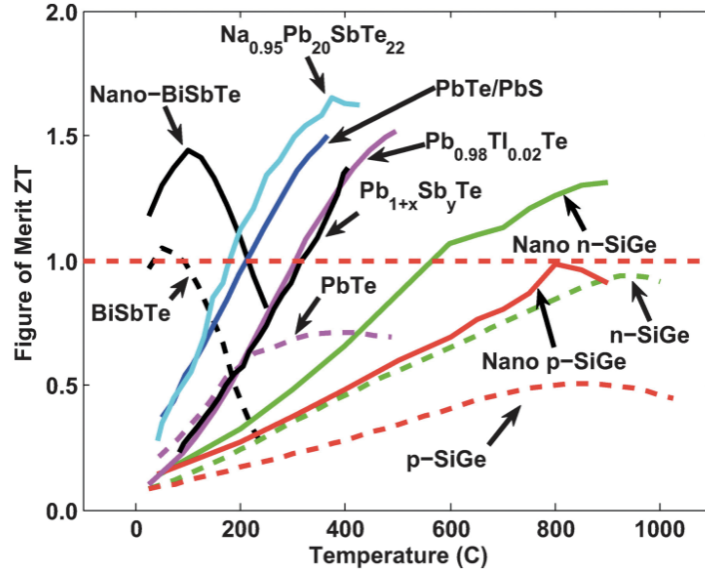


Figure 1-7. Figure of merit ZT of current state of the art thermoelectric materials versus temperature. The dashed lines show the maximum ZT values for bulk state of the art materials, and the solid lines show recently reported ZT values, many of which were obtained in bulk nanostructured materials.²⁹ Reprinted from [29] with permission. Copyright © 2009, Royal Society of Chemistry.

As implicated above, nano-engineering approaches represent the primary pathway to enhancing the ZT; yet, they rely on the same classes of materials that are already known as bulk thermoelectric materials. Along with the efforts to improve the thermoelectric properties of existing materials, the search for alternative solutions to increasing ZT and uncovering new thermoelectric materials continues. In the next section some of these new materials classes and strategies are presented and discussed.

1.4 Emerging materials for thermoelectric applications

The most investigated candidates for thermoelectric applications so far are doped semiconductors and semimetals. Mid last century, an extensive screening of materials led to the identification of several alloys and intermetallics based on elements like Bi, Te, Sb, Pb, etc., and ZT of unity at low temperatures (300–500 K) was achieved.^{40,41} Mixed composite structures with

increased thermoelectric properties have also been reported. For example, it has been shown that alloying Bi_2Te_3 with other isoelectronic cations and anions would lower the thermal conductivity while maintaining the electrical conductivity.⁴² Alloying the binary tellurides (Bi_2Te_3 , Sb_2Te_3 , PbTe and GeTe) continues to be an active area of research.^{43–46} There has also been a remarkable progress in organic thermoelectric (OTE) materials and devices in the past several years.^{41,47,48} The majority of organic thermoelectric materials reported to date are based on conductive polymers, including conjugated polymers and certain coordination polymers.^{49–52} The scalability, mechanical flexibility, and stability of semiconducting polymers up to 200 °C have made OTE materials suitable for economically viable TE generators (TEG). As-synthesized PA: I_x ^{53,54}, TDAE-reduced (22%) PEDOT: Tos⁵⁰, (24%) PEDOT: Tos⁵⁵, electrochemically-reduced PEDOS-C6: ClO_4 ⁵⁶, and spun-casted PEDOT: PSS⁵⁷ polymers have been reported to have a power factor of higher than 300 $\mu\text{W}/\text{mk}^2$

Another group of materials studied for thermoelectric applications are allotropes of carbon, graphene, and carbon nanotubes.^{58–63} Despite the high carrier mobility, high thermal conductivity up to 5,000 W/mK, and a poor Seebeck coefficient of $\sim 30\text{--}60 \mu\text{V}/\text{K}$, several studies have shown that the power factor of graphene could be increased by introducing grain boundaries into synthetic graphene through chemical vapor deposition (CVD) and band-structure modulation of graphene.⁶¹ Pure graphene thermoelectric devices with a Seebeck coefficient of $90 \mu\text{VK}^{-1}$,^{64,65} Graphene(rGO)/fullerene (C_{60}),⁶⁶ and graphene/CNT nano-composites^{67,68} prepared with PEDOT: PSS have been also studied by several groups. In almost all studies the composites showed a better performance compared to that of pure PEDOT: PSS.^{69,70} Polymer-based composites of carbon nanotubes and graphene also possess several properties^{71,72} that make them strong candidates for uses in low power waste heat recovery applications. CNTs, depending on their

sizes and diameters, could help enhance phonon scattering rates, while offering higher Seebeck coefficient, and electrical conductivity, whereas the polymer matrix is beneficial due to its very low thermal conductivity to achieving a high ZT .⁷³⁻⁷⁷ Ceramic oxide materials are another group of materials that was subject to investigation for potential use in thermoelectric applications. Ceramic TEs may enable use of higher service temperature because of their stability at high temperatures in oxidizing and corrosive environments. Example materials include $A_x \text{CoO}_2$ ^{78,79}, $\text{Ca}_3 \text{Co}_4 \text{O}_9$ ⁸⁰⁻⁸³, $\text{Sr}_x \text{Ba}_{1-x} \text{Nb}_2 \text{O}_{6-\delta}$ ⁸⁴ and the layered $\text{Sr}_2 \text{Nb}_2 \text{O}_7$ ⁸⁵.⁸⁶⁻⁸⁸

As mentioned earlier and demonstrated by the reported studies in this section, the unifying parameter to identifying high- ZT materials ($ZT > 1$), is a lattice thermal conductivity that should fall in the range of amorphous material limit without comprising the electrical conductivity, as well as a relatively large Seebeck coefficient. Such properties are not easily found at the same time in any given material, and as seen so far, usually some material engineering in the form of nanostructuring, alloying, creating complex crystal structures, or building superlattices is required. While these engineering techniques would result in enhanced thermoelectric properties, they would entail higher fabrication cost only to limit their potential for mass-scale deployment. Therefore, the key question would be whether there exists a material or a class of materials that possesses all the desired characteristics of a high efficiency thermoelectric material, i.e. large Seebeck coefficient, high electrical conductivity, and relatively low thermal conductivity, while offering easier processing and more economical mass production?

Very recently it has been discovered that in fact such materials, potentially, exist. In part thanks to the advances in the condensed matter physics for the discovery of topological insulators (TI).

In recent years, the discovery of a novel state of quantum matter known as topological insulator (TI)^{89,90} has created a surge of research activities in various fields of science. The topological

band structure of these materials gives rise to nontrivial electronic properties not found in other materials. As we will see in the following sections, such properties also enable the topological materials to hold great potential for high efficiency thermoelectric applications⁹¹⁻⁹⁴.

In the next section, a concise introduction to topological materials and their characteristics is presented, and their potential for high efficiency thermoelectric applications and room temperature waste heat recovery is discussed.

1.4.1 Topological Materials for Thermoelectric Applications

In condensed matter physics, the interest has always been in the discovery and classification of distinctive phases of matter. In the quantum world, atoms and electrons can form new and various states of matter such as crystalline solids, magnets, and superconductors. The discovery of quantum Hall (QH) state in 1980s⁹⁵ has led to a different classification paradigm based on the notion of topological order.^{96,97} QH provided the first example of a quantum state that had no broken symmetry. QH is realized in electrons confined in two dimensions in the presence of a strong magnetic field and dissipation-less current flows along the sample's edge. In recent years, topological insulators have been found to have similar metallic states to those of a QH system that are also transported in a low-dissipation state

The discovery of topological insulators (TIs) has provided a new research platform in several fields including thermoelectrics. TIs have attracted considerable attention in contemporary materials science showing gapless helical mass-less Dirac fermions on a two-dimensional (2D) surface or one dimensional (1D) edge along which spin-up and spin-down electrons counter-propagate.

TIs and good TE materials have common features in their properties. In fact, typical three dimensional TIs such as Bi_2Se_3 , Bi_2Te_3 and $\text{Bi}_{2-x}\text{Sb}_x\text{Te}_3$ have been studied as promising

candidates for TE materials. Recent theoretical studies suggested that additional nontrivial conduction channels existing in pure topological surface Dirac states in three-dimensional TIs may provide a unique route to enhance ZT. To gain a better understanding of the nontrivial topology of TIs, we first take a look at the conventional band theory.

In conventional band theory⁹⁸⁻¹⁰² materials are classified into insulators and metals based on the existence of a finite band gap. An important concept in the band theory is the Fermi level E_F . As depicted in Fig. 1-8, the position of the Fermi level with relation to the conduction/valance band is a crucial factor in determining electrical properties of materials. The general form of the dispersion relation can be written as

$$E(\vec{k}) = E(0) + \frac{\hbar^2 k^2}{2m^*} \quad (1-5)$$

Where E is the energy level of the electron, $E(0)$ is the energy of the electron at the ground state, k is the wave vector, \hbar is the Planck's constant, and m^* is the effective mass of the electron and is defined by

$$\frac{1}{m^*} \equiv \frac{\partial^2 E(\vec{k})}{\hbar^2 \partial k^2} \quad (1-6)$$

With some approximation, we can say that an electron in a solid moves like a free electron with an effective mass m^* . According to Eq. (1-6), as the band curvature becomes larger, the effective mass of the electron becomes smaller. The mean velocity of the electron is also given by

$$\vec{v}_k = \frac{1}{\hbar} \frac{\partial E(\vec{k})}{\partial \vec{k}} \quad (1-7)$$

Equations (1-6) and (1-7) imply that if we know the shape of the $E(\vec{k})$ curve, we would be able to estimate the velocity as well as the effective mass of the electrons. For this reason, the energy dispersion relation $E(\vec{k})$ becomes very important in determining the transport properties for carriers in solids. This concept will come in handy later when discussing the topological band structure.

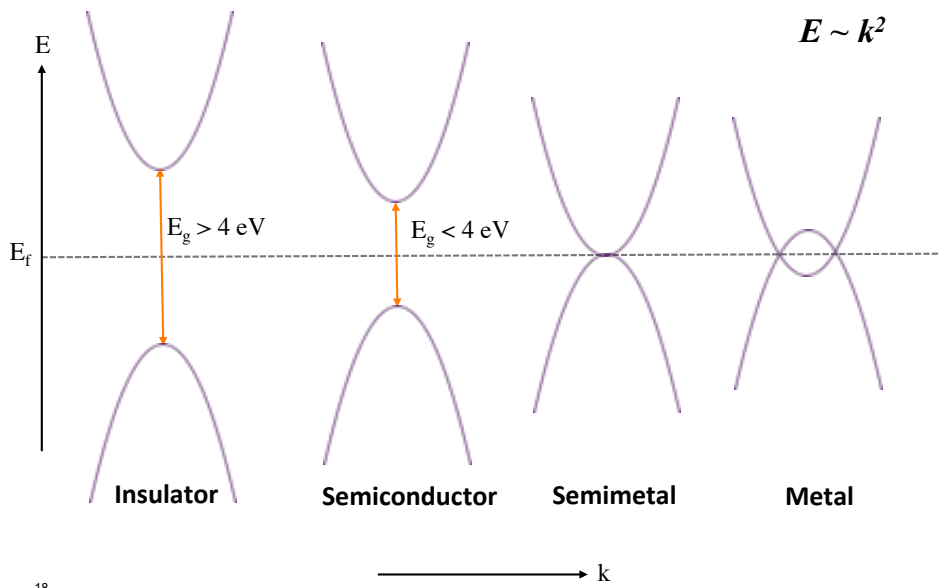


Figure 1-8. Classification of solids according to the conventional Band Theory. The electronic properties of materials depends on the existence of a finite band gap and the position of Fermi level with respect to the conduction and valance bands. In the conventional Band Theory, the energy dispersion relation $E(\vec{k})$ of solids assumes a quadratic form.

In recent years, it has been realized that in transition from insulators to metals, there exists an intermediate state in which the conduction and valence band touch only at discrete points, leading to a zero band gap and singular points at the Fermi surface. This has led to the emergence of a new class of insulators known as topological insulators.¹⁰³

Topological insulators are materials with a bulk band gap generated by strong spin-orbit coupling (SOC) and topologically protected metallic surface states. This makes these materials

insulating in the bulk, but metallic at the surface. A TI can be identified by a few rules: SOC, an odd number of band inversions (BIs) between the conduction and the valence band by increasing the average nuclear charge, and a sign change of the symmetry of the molecular orbitals. Such properties give rise to nontrivial electronic behavior in TIs, and make them excellent candidates for thermoelectric studies.^{89,104}

In contrast to conventional band insulator, Fig. 1-9 (a), for a topological insulator the spin-orbit coupling effect causes the energy of the valence band to become higher than that of the conduction band at some k points¹⁰⁵, resulting in a “band inversion” in the electronic band structure of the TI, Fig. 1-9 (b).

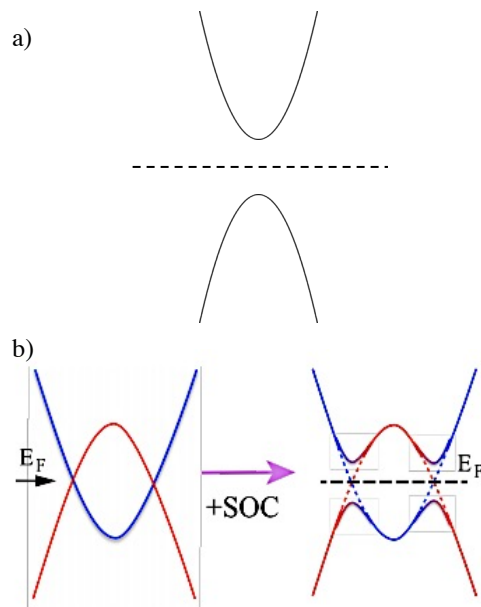


Figure 1-9. (a) For a conventional band insulator, the energy of the valence band will always remain lower than that of the conduction band at all k points throughout the Brillouin zone (BZ), and the insulator is topologically trivial. (b) Schematic plot for the band inversion mechanism. Band Inversion involves the energy order switching of low energy electronic bands around certain k points in the Brillouin zone. Assuming that the two bands do not couple when the SOC is absent, they must cross at certain k-points away from Γ . In the presence of the spin-orbit coupling (SOC), the two bands will, in general, couple together and open up a gap at the crossing point. As a result, the system becomes an insulator. Reprinted from [105] with permission. Copyright © 2014, Materials Research Society.

The presence of a band inversion is a necessary but not a sufficient condition for topological phases. A topological phase is defined by a topological number known as the Chern number^{89,106},

which is a global quantity calculated using the electronic wave function throughout the BZ. Although band inversion cannot rigorously define any topological phase, it is in fact very suggestive for identifying new topological materials and compounds, and also for understanding the topological nature in various topological materials¹⁰⁷⁻¹⁰⁹. To understand the remarkable properties of TIs, we will first review the charge transport in its predecessor, the quantum Hall state.

The QH effect, also known as the integer quantum Hall effect (IQH)¹¹⁰⁻¹¹² is a quantum version of the Hall effect, which is achieved by applying a strong magnetic field, \mathbf{B} in two-dimensional electron systems. The strong magnetic field \mathbf{B} in a QH system drives the electrons to circulate in quantized orbitals. In band theory, the quantization of the electrons' circular orbits leads to quantized Landau levels, and the skipping trajectory at the edges transforms into a quasi-one-dimensional edge channel encircling the interior of the system^{97,113}, Fig. 1-10 (a). As a result, the integer quantum Hall becomes an insulator in the bulk because the Fermi level is located in the middle of two Landau levels. On the other hand, the edges of the IQH state feature chiral 1D metallic state, leading to remarkable quantized charge transport phenomenon. The direction of the edge-state momentum, \mathbf{k} is determined by the orientation of the applied magnetic field.¹¹⁴ In other words, the direction of the momentum cannot be changed unless the direction of the magnetic field is changed. Under such circumstances, when an edge-state electron encounters an impurity, instead of being scattered back, i.e. $\mathbf{k} \rightarrow -\mathbf{k}$, it takes a detour and keeps going in the same direction as dictated by the direction of the magnetic field. This robust mechanism is called chirality, and it protects the edge-states against any system disorder, which is usually inevitable in any realistic state.

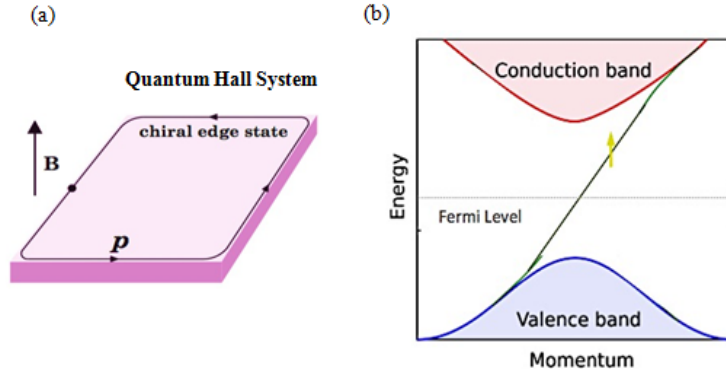


Figure 1-10. (a) Two-dimensional electron system in a perpendicular external magnetic field B forming a quantum Hall system; (b) The electronic band structure of a quantum Hall system. A single edge state connects the valence band to the conduction band.

Even at low temperatures, there are some random fluctuations of the electrostatic background that tend to induce elastic momentum scattering leading to resistance. However, for an edge-state, such backscattering processes are not allowed as there is not any other available counter-propagating state. Such dissipation-less transport mechanism is the essence of the quantum Hall effect, and is extremely attractive for electronic devices. The necessary condition for such charge transport is the absence of the mobile bulk carriers. Therefore, the edge modes of a quantum Hall system must occur in the energy gap between the bulk bands, as shown in Fig. 1-10(b). The quantum Hall effect is robust against continuous deformations of the band structure as long as the bulk band gap and the edge modes remain intact.¹¹⁴ It is noteworthy that the quantum Hall phenomenon is in fact a consequence of breaking the time-reversal symmetry (TRS) as a result of the presence of a large external magnetic field. In the QH system, the requirement of a large magnetic field, strictly limits the potential applications of the quantum Hall effect. The search for a QH-like state with a nonzero Chern number without the need for an external magnetic field led to the discovery of a new topological state called the quantum spin Hall (QSH)¹¹⁵⁻¹¹⁷ state, and subsequently the 2D topological insulators (2D-TIs). Topological insulators feature exotic edge-states in a zero magnetic field without breaking the TRS^{115,117}. This becomes possible due to the

intrinsic spin-orbit coupling effect¹¹⁸⁻¹²¹ in such materials. In a simple picture, the spin-orbit coupling can be viewed as an intrinsic effective magnetic field \mathbf{B}_{eff} that points in the opposite directions for the up- and down- spin particles, as illustrated in Fig. 1-11(a). Each spin subsystem resembles a quantum Hall insulator with a gapless edge-mode. Combining these two subsystems into a single system results in a pair of counter-propagating edge-states in a zero magnetic field, as depicted in Fig. 1-11(b).

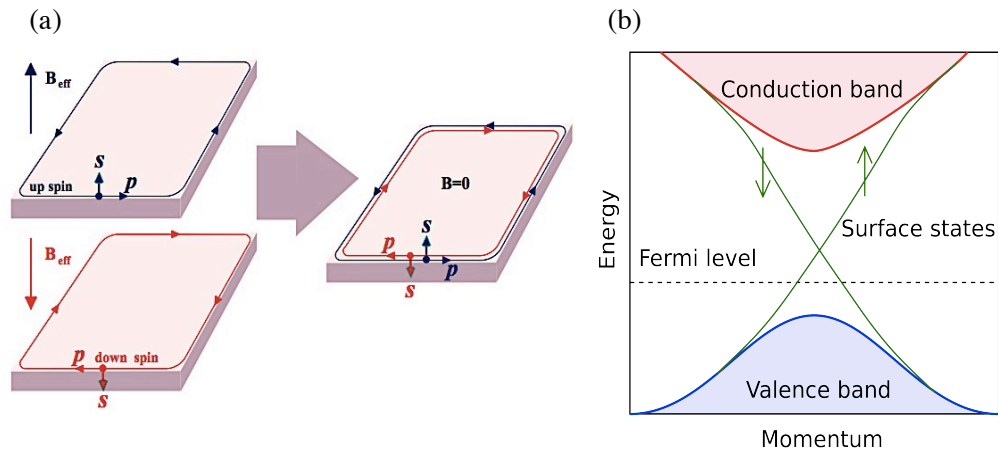


Figure 1-11. (a) The quantum-spin Hall system can be viewed as two copies of the quantum Hall system with an intrinsic effective magnetic field \mathbf{B}_{eff} that points in the opposite directions for the up- and down- spin species. (b) The electronic band structure of a quantum spin Hall system. Each quantum Hall subsystem shares a single edge state resulting in a pair of edge-states in a zero magnetic field.

Similar to the QH systems, 2D-TIs are also insulating in the bulk, but on the boundary they have gapless edge-states that are topologically protected and immune to impurities or geometric perturbations^{120,122-126}. The significance of this behavior becomes even more pronounced when they are compared with conventional conductors. In conventional systems, in the presence of any small perturbation, all propagating states become localized due to a phenomenon known as Anderson localization^{127,128}. In a 2D-TI, such localization is not allowed^{118,129,130} because of the robustness of the nontrivial edge-states against any disorder in the system. This is what makes the TI system stand out from the ordinary conductors.

Although all materials have spin-orbit coupling, only a few of them turn out to be topological insulators. The strong spin-orbit coupling in most topological insulators leads to a band inversion in the electronic band structure.^{131–135} The presence of band inversions in the electronic band structure of materials was proposed as the general mechanism for finding topological insulators¹⁰⁷, and it was theoretically predicted and experimentally observed in mercury telluride quantum wells¹¹⁹, bismuth antimony alloys^{136,137}, Bi_2Se_3 and Bi_2Te_3 bulk crystals^{108,138,139}. To date, the 2D topological insulators have mostly been realized at buried interfaces of ultraclean semiconductor heterostructures at very low temperatures.

A critical breakthrough in the experimental and material physics came in when the three-dimensional analogue of the QSH system was theoretically realized.^{89,103,140–142} This was a remarkable achievement as materials in nature are mostly in the 3D form and also the synthesis and fabrication of bulk materials is usually easier. The 3D topological insulators are insulating in the bulk region, but have gapless states on the surface of the bulk material, as shown in Fig. 1-12. Similar to the edge-states in 2D QSH systems, the metallic topological surface states in 3D-TIs are induced by spin-orbit coupling (SOC)^{143–145} and are protected by time-reversal symmetry. Time-reversal symmetry forbids the elastic backscattering of the surface states, and hence the dissipation-less transport of the topological surface states is robust against nonmagnetic weak disorders.

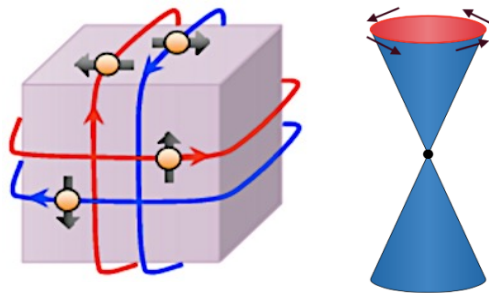


Figure 1-12. Schematic of a 3D topological insulator. 3D TIs support protected Dirac-like propagating states on the surface while the inner part of the system behaves as an insulator. Reprinted from [143] with permission. Copyright ©2013 The Physical Society of Japan.

On the surface of a 3D-TI, a carrier is free to move in two dimensions, but its spin is locked in the direction of the momentum \mathbf{k} . The dispersion relation of the surface states in a 3D-TI, $E_{\mathbf{k}}$ can be derived by solving the Schrödinger equation and will have the form of:

$$E_{\mathbf{k}} = \pm \frac{v}{\hbar} |\mathbf{k}| = \pm \frac{v}{\hbar} \sqrt{k_x^2 + k_y^2} \quad (1-8)$$

This equation is for a cone whose vertex is at $(k_x, k_y) = (0,0)$ and opens in the $E_{\mathbf{k}}$ direction, as illustrated in Fig. 1-13. The \pm signs correspond to the positive and negative energy branches.

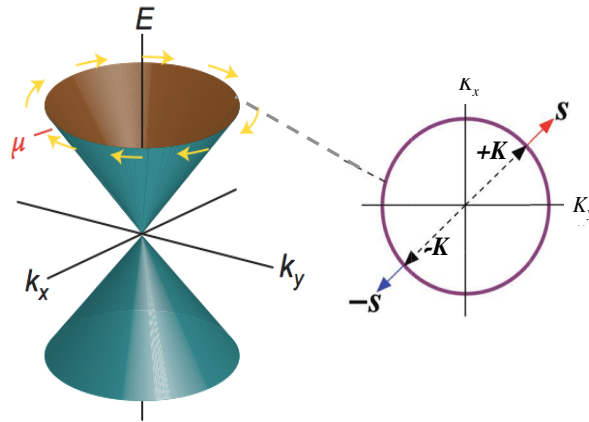


Figure 1-13. (Left) Plot of the dispersion relation, $E_{\mathbf{k}}$, for the surface-states of a 3D TI. $E_{\mathbf{k}}$ takes the form of cone. (Right) Example of the Kramer's pair on a constant-energy line. Arrows illustrate the locking of momentum \mathbf{k} and spin \mathbf{s} vectors.

It is important to note that the dispersion relation of the metallic surface states in 3D-TIs has a linear relation with \mathbf{k} , i.e. $E_{\mathbf{k}} \sim \mathbf{k}$. As we saw earlier, in the conventional band theory $E_{\mathbf{k}}$ has a quadratic form in the momentum space, i.e. $E_{\mathbf{k}} \sim \mathbf{k}^2$. This is another important feature that

distinguishes the topological energy bands from their conventional counterparts. The positive and negative cones of the surface-states play the role of the conduction and valence bands of the surface carriers. This conical energy spectrum is reminiscent of that of relativistic particles described by the Dirac equation for spin-1/2 particles^{146,147}. For this reason, the surface states in 3D-TIs are frequently referred as Dirac fermions¹⁴⁸⁻¹⁵¹.

The first experimental realization of a topologically nontrivial phase of matter in 3D bulk materials came in 2007 by identifying the strong 3D-TI phase in $\text{Bi}_{1-x}\text{Sb}_x$ semiconducting alloy system^{137,152,153}. Shortly after, with the aid of angle-resolved photo-emission spectroscopy (ARPES) technique, the 3D topological surface states were observed in other material systems including tetradymite compounds such as Bi_2Se_3 ¹⁵⁴, Bi_2Te_3 , and Sb_2Te_3 ¹³⁹, thallium-based ternary chalcogenides such as TlBiSe_2 ¹⁵⁵⁻¹⁵⁷, and TlBiTe_2 ¹⁵⁷ as well as Pb-based layered chalcogenides such as $\text{Pb}(\text{Bi}_{1-x}\text{Sb}_x)_2\text{Te}_4$ ¹⁵⁸, and PbBi_2Te_4 ¹⁵⁹. Other candidate materials that have been identified to host a three-dimensional TI phase include strained layers of α -Sn and strained HgTe.^{136,160}

The nontrivial properties of topological insulators make them extremely attractive for electronic and optoelectronic applications. The suppression of backscattering of the surface states corresponds to exceptional transport mobility and reduced energy consumption, which make TIs great candidates for Ultra low power electronics. Other potential applications of TIs include novel spintronic devices, optoelectronics such as transparent conductors and wideband photodetectors, catalysis applications, and high efficiency thermoelectric applications.

It is intriguing to note that almost all currently known topological insulators are good thermoelectric materials. Advanced thermoelectric materials have an optimized efficiency through low thermal conductivity and excellent electrical conductivity. Consequently, heavy-element compounds tend to have a better performance, because a large atomic mass reduces the

thermal conductivity. Moreover, the optimal bandgap of semiconductors for thermoelectric applications is typically one order of magnitude higher than the thermal energy of the operation temperature, so room-temperature thermoelectric materials are usually narrow-gap semiconductors. For topological insulators, spin–orbit coupling must be strong enough to modify the electronic structure – as spin–orbit coupling strength increases with atomic mass – this indicates that narrow-bandgap compounds consisting of heavy elements are the most promising candidates. It is therefore natural to explore the potential impact of the surface states of topological insulators.

However, current topological insulators typically have excessive bulk carrier, which prevent the bulk from being insulating. This will mask the subtle topological effects from the surface electrons; and the small bulk energy gap also prevents them from being used in room temperature electronic devices. Therefore, to access the remarkable properties of the surface carriers, it is necessary to controllably suppress the bulk conductivity by constraining the chemical potential to the bulk bandgap. Although doping of these materials has been investigated extensively for thermoelectric applications, the strategy cannot be directly adopted for quasi-insulating crystals owing to their different doping-level requirements (high-performance thermoelectric materials are typically doped to a high level to give metallic bulk conductivity).

The exotic properties of TIs and the limitations in accessing their metallic surface states prompted an immense interest in finding new materials other than insulators that could possess linear Dirac-like dispersion in their bulk region, i.e. 3D Dirac fermions.

Through careful studies of topological states, it was revealed that in the transition from a 3D topological insulator to a normal insulator, there exists an intermediate state in which the co-existence of certain crystallographic symmetries^{161,162} – time-reversal symmetry (TRS), inversion

symmetry (IS), and uniaxial rotational symmetry – protects the degeneracy of the band crossings giving rise to protected linearly dispersing valence and conduction bands that cross in the electronic structure of the bulk material^{163–166} and form a stable 3D Dirac semimetal phase.^{162,163,165,167,168} In this topological state, the bulk conduction and valence bands touch only at discrete (Dirac) points and disperse linearly along all three momentum directions leading to the formation of 3D Dirac fermions^{163,168,169} Being in a semimetallic phase and possessing bulk Dirac fermions, these materials are classified as “topological Dirac Semimetals (TDS)”^{162,170,171}. A conceptual illustration of the difference between a TI and a Dirac semimetal is given in Fig. 1-14.

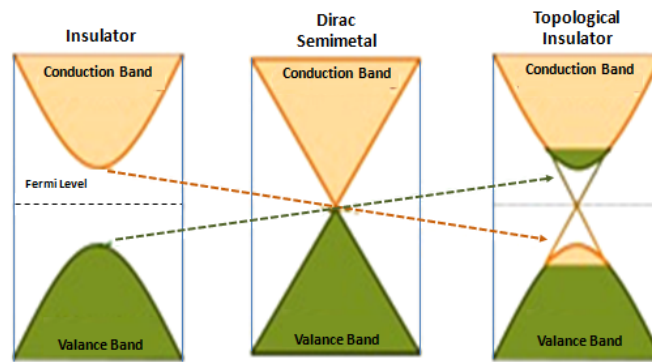


Figure 1-14. A conceptual diagram of the electronic band structure in different phases. In a topological insulator an energy gap opens in the bulk region. In Dirac semimetals the bulk conduction and valence bands touch only at discrete (Dirac) points and disperse linearly along all three momentum directions leading to the formation of 3D Dirac fermions.

The most famous material belonging to the class of TDS is graphene. The geometry of an sp^2 -hybridized carbon in graphene is responsible for the formation of the hexagonal honeycomb lattice that determines its extraordinary mechanical and electronic properties¹⁷², Fig. 1-15(a). Intrinsic graphene is a 2D Dirac semimetal in the absence of spin-orbit coupling¹⁶³. The electronic dispersion relation around the Fermi energy in graphene is linear for low energies near

the six corners of the two-dimensional hexagonal Brillouin zone^{173,174} and is given by $E = \hbar v_F |\mathbf{k}|$ ^{173,175} where the Fermi velocity $v_F \sim 10^6$ m/s. Therefore, 2D Dirac particles in graphene travel effectively as massless particles, allowing them to reach much higher speeds than ordinary electrons – as high as 10^6 m s⁻¹. As a result, the electron mobility in graphene is about 10^5 cm²/Vs, compared with about 1400 cm²/Vs in silicon^{176,177}. Each of the two equivalent carbon atoms within one unit cell of graphene contributes one cosine-shaped band to the electronic structure. These bands cross exactly at the Fermi level, where they form a Dirac cone with a linear electronic dispersion^{171,172}, Fig. 1-15 (b)

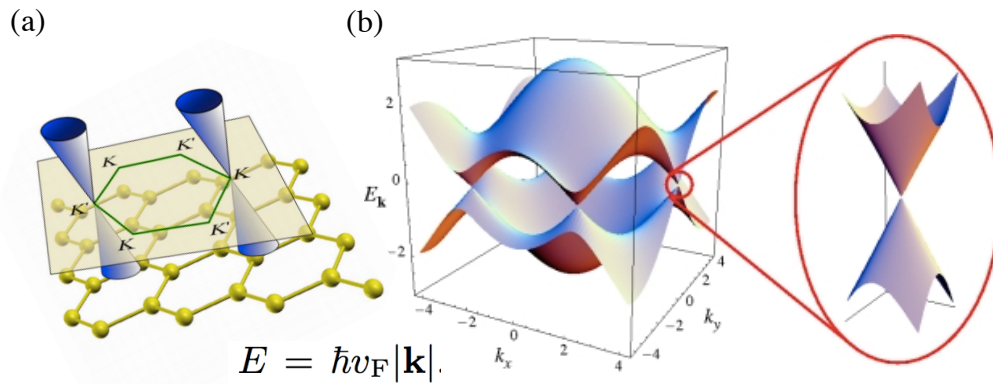


Figure 1-15. (a) Carbon atoms in graphene form a honeycomb lattice with two atoms in the unit cell. The first Brillouin zone of the reciprocal lattice contains two nonequivalent Dirac points, K and K' . The relevant states at the Fermi level form two touching cones with the tips at K and K' . (b) Each of the two equivalent carbon atoms within one unit cell of graphene contributes one cosine-shaped band to the electronic structure that cross exactly at the Fermi level forming a Dirac cone with a linear electronic dispersion. Reprinted from [171] with permission. Copyright ©2009 American Physical Society.

After the explosion of research in graphene, interest was piqued in realizing this state in a 3D system. In general, 3D Dirac semimetals could be obtained by fine-tuning those materials that are near the 3D Dirac semimetal state. This could be done through changing their chemical composition, tuning the strength of spin-orbit coupling, or with external variables such as temperature and pressure.¹⁷⁸ Some examples include $\text{TlBiSe}_{2-x}\text{S}_x$ ^{179,180}, $\text{Hg}_{1-x}\text{Cd}_x\text{Te}$ ¹⁸¹, Bi_{2-x}

In_xSe_3 , $\text{Pb}_{1-x}\text{Sn}_x\text{Se}$, $\text{Pb}_{1-x}\text{Sn}_x\text{Te}$, $\text{Bi}_{1-x}\text{Sb}_x$, and $\text{Hg}_{1-x}\text{Cd}_x\text{Se}$ ^{90,104,182} all for a specific value of x . However, such Dirac semimetals are usually sensitive to temperature, pressure, and composition homogeneity. Therefore, alternative types of 3D Dirac semimetals that are not so sensitive to the environmental conditions or the compounds ratio are desired.

The breakthrough in the search for stable 3D Dirac semimetals has been achieved in the recent studies on Na_3Bi ^{178,183-185} and Cd_3As_2 ^{169-171,186-188} compounds. In both compounds, a pair of intrinsic 3D Dirac points stably exists on the k_z axis protected by crystalline rotational symmetry, C_4 in Cd_3As_2 and C_3 in Na_3Bi , as shown in Fig. 1-16. Both of these materials possess stable, robust 3D Dirac semimetal states as the crossing points in their band structure are not dependent on temperature or a specific compositional parameter that could vary at different points in a single crystal.^{185,186,188-191}

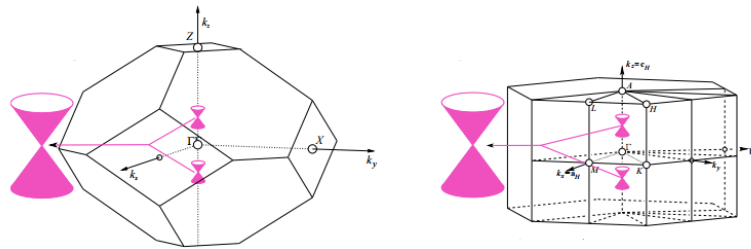


Figure 1-16. Schematic electronic structures showing the location of 3D Dirac cones in the Brillouin zone in (a) Cd_3As_2 , and (b) Na_3Bi . Reprinted from [178] with permission. Copyright ©2015 American Physical Society.

Compared with the air-sensitive Na_3Bi , Cd_3As_2 tends to be much more stable at room temperature with a high chemical stability against oxidation which makes it an ideal system for experimental studies¹⁹².

1.4.2 Crystalline Cd_3As_2 for Thermoelectric Applications

Among the $\text{II}_3\text{-V}_2$ types narrow gap semiconductors, Cd_3As_2 has drawn a lot of attention, in part because it was believed to have inverted band structure^{169,188,193,194}, whereas all other compounds

Cd_3P_2 , Zn_3As_2 , and Zn_3P_2 have normal band ordering. Crystal structure of Cd_3As_2 ¹⁶⁹⁻¹⁷¹ has a tetragonal unit cell with $a=12.67 \text{ \AA}$; and $c= 25.48 \text{ \AA}$; for $Z=32$ with symmetry of space group $I4_1cd$, Fig. 1-17 (a,b). In this structure, arsenic ions are approximately cubic close-packed and Cd ions are tetrahedrally coordinated, which can be described in parallel to a fluorite structure of systematic Cd/As vacancies. There are four layers per unit and the missing Cd-As₄ tetrahedra are arranged without the central symmetry as shown with the (001) projection view in Fig. 1-17(b), with the two vacant sites being at diagonally opposite corners of a cube face. The corresponding BZ is shown in Fig. 1-17(c). The center of the BZ is the G point, the centers of the top and bottom square surfaces are the Z points, and other high-symmetry points are also noted.

Similar to most of the semiconductors with antiferite¹⁹⁵ or zinc-blende structures, the low energy electronic properties of Cd_3As_2 are mostly determined by the Cd-5s states (conduction bands) and the As-4p states (valence bands), as shown in Fig. 1-17(d). There are two distinct features in the band structure of Cd_3As_2 . First, a band inversion occurs around the Γ -point with the s state lower than the p states, which is an important sign of nontrivial topology. Also, the band structure is semimetallic with a band crossing along the Γ -Z direction^{170,186,188}.

The C_4 rotational symmetry around the k_z axis in the Cd_3As_2 crystal results in two different representations, Λ_6 and Λ_7 , of the crossing bands. This prohibits hybridization between them and prevents the formation of a full band gap in the electronic structure, resulting in the protected band crossing. As such, two Dirac points at $\pm k_z$ are observed in this material. As a result, Cd_3As_2 has a stable symmetry-protected bulk (3D) semimetal phase¹⁸⁷ with the Fermi surface consisting of a single pair of Fermi points;^{169,194} and hence it is considered to be the 3D analogue of graphene.

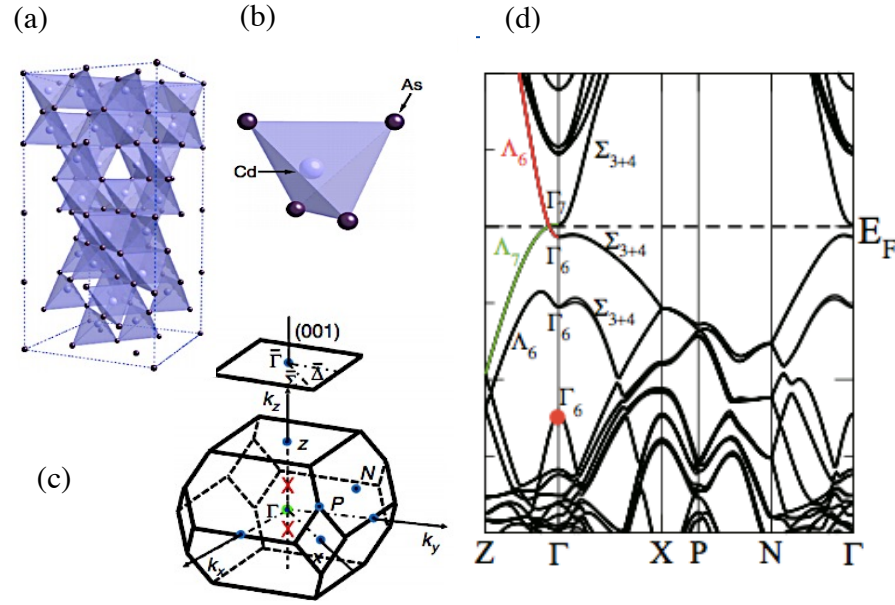


Figure 1-17. Brillouin zone symmetry and 3D Dirac cone. (a) Cd_3As_2 crystallizes in a tetragonal body centre structure with space group of $I41cd$, which has 32 number of formula units in the unit cell. The tetragonal structure has lattice constant of $a \approx 12.670 \text{ \AA}$, $b \approx 12.670 \text{ \AA}$ and $c \approx 25.480 \text{ \AA}$. (b) The basic structure unit is a four corner-sharing CdAs_3 -trigonal pyramid. Reprinted from [170] with permission. Copyright ©2013 American Physical Society (c) The bulk BZ and the projected surface BZ along the (001) direction. The red crossings locate at $(k_x, k_y, k_z) \approx (0, 0, 0.15(2p)/(c^*))$ ($c^* \approx c/a$). They denote the two special k points along the Γ -Z momentum space cut-direction, where 3D Dirac band-touching points are protected by the crystalline C_4 symmetry along the k_z axis. (d) The band structure of Cd_3As_2 . A band inversion occurs around the Γ -point with the s state (red solid circle) lower than the p states, resulting in the nontrivial topology. The band structure is semimetallic with a band crossing along the Γ -Z direction. Reprinted from [186] with permission. Copyright © 2014, Rights Managed by Nature Publishing Group.

The high in-plane Fermi velocity along with the massless Dirac fermions in crystalline Cd_3As_2 results in a natural high carrier mobility of $\sim 10^5 \text{ cm}^2 \text{ V}^{-1} \text{ S}^{-1}$.¹⁹⁶ Transport experiments have revealed a hidden protection mechanism that strongly suppresses the backscattering of electrons in the absence of magnetic field, leading to an exceptionally long electron mean free path up to hundreds of micron meters at low temperatures, thus holding a great prospect for the high TE performance.^{186,197} The carrier back-scattering remains suppressed and the electrical transport is dominated by high-energy carriers that favorably affect the thermo-power of Cd_3As_2 .^{198–201} Since the power factor is to increase with the carrier mobility, μ , and weighted density-of- states

effective mass, i.e. $S^2\sigma = \mu m_D^{*1.5}$, and the lattice thermal conductivity is predicted to be very low, Cd_3As_2 shows a strong potential for demonstrating high, device-favorable S , and in turn ZT . In this work, we perform a fully experimental investigation to confirm that crystalline Cd_3As_2 would be indeed an exceptional candidate for advanced high efficiency room temperature TE technologies. A reduced-temperature vapor-based crystallization pathway was developed in this work to produce free-standing, stoichiometric 2D cm-size crystals of Cd_3As_2 . Following the synthesis of single-crystal Cd_3As_2 platelets, a thorough structural characterization was performed to confirm the formation and the quality of our crystals. The method and synthesis procedure as well as the results of several structural studies are provided in chapter 2. The study of thermoelectric properties of Cd_3As_2 starts in chapter 3 by analyzing the results of temperature-dependent transport measurement on Cd_3As_2 platelets. Using these results, the electrical conductivity, Seebeck coefficient, and subsequently the thermo-power of crystalline platelets are calculated. Finally, in chapter 4, the 1ω method for measuring the thermal conductivity of materials is explained, and its result for the synthesized Cd_3As_2 samples is reported. Using this information, we will assess the ZT figure of merit of our crystalline platelets to make a conclusion about the thermoelectric properties of Cd_3As_2 . Chapter 5 will wrap up the work, and suggests a few pathways for future studies.

References

1. Statistical Review of World Energy | Energy economics | BP Global. *bp.com* Available at: <http://www.bp.com/en/global/corporate/energy-economics/statistical-review-of-world-energy.html>. (Accessed: 12th March 2017)
2. Kanellos, M. Will Waste Heat Be Bigger Than Solar? (2009). Available at: <https://www.greentechmedia.com/articles/read/will-waste-heat-be-bigger-than-solar-5577>. (Accessed: 12th March 2017)
3. Bent, H. A. The second law of thermodynamics: Introduction for beginners at any level. *J. Chem. Educ.* **39**, 491 (1962).
4. Wilming, H., Gallego, R. & Eisert, J. Second law of thermodynamics under control restrictions. *Phys. Rev. E* **93**, 042126 (2016).
5. Kolasiński, P. & Kolasińska, E. Direct waste heat recovery via thermoelectric materials - chosen issues of the thermodynamic description. *IOP Conf. Ser. Mater. Sci. Eng.* **113**, 012022 (2016).
6. C.E.M, A. T., P. E. & Ph.D, D. P. M. *Handbook of Energy Engineering, 7th Edition*. (Lulu Press, Inc, 2014).
7. Pub52953.pdf.
8. van de Bor, D. M., Infante Ferreira, C. A. & Kiss, A. A. Low grade waste heat recovery using heat pumps and power cycles. *Energy* **89**, 864–873 (2015).
9. Härtel, A., Janssen, M., Weingarh, D., Presser, V. & Roij, R. van. Heat-to-current conversion of low-grade heat from a thermocapacitive cycle by supercapacitors. *Energy Environ. Sci.* **8**, 2396–2401 (2015).
10. 68 IJAET Vol III Issue I 2012.pdf.
11. Mirolli, M. D. The Kalina cycle for cement kiln waste heat recovery power plants. in *Conference Record Cement Industry Technical Conference, 2005*. 330–336 (2005). doi:10.1109/CITCON.2005.1516374
12. Kalina Cycle power systems in waste heat recovery applications. Available at: <http://www.globalcement.com/magazine/articles/721-kalina-cycle-power-systems-in-waste-heat-recovery-applications>. (Accessed: 12th March 2017)
13. Huang, X. Y., Wang, H. Y., Wu, Z., Zhu, T. & Wu, J. Z. Selection of working fluids for organic rankine cycle (ORC) in waste heat power generation system. in *2013 International Conference on Materials for Renewable Energy and Environment* **3**, 774–779 (2013).

14. Zhang, X., Wu, L., Wang, X. & Ju, G. Comparative study of waste heat steam SRC, ORC and S-ORC power generation systems in medium-low temperature. *Appl. Therm. Eng.* **106**, 1427–1439 (2016).
15. Wei, D., Lu, X., Lu, Z. & Gu, J. Performance analysis and optimization of organic Rankine cycle (ORC) for waste heat recovery. *Energy Convers. Manag.* **48**, 1113–1119 (2007).
16. Larjola, J. Electricity from industrial waste heat using high-speed organic Rankine cycle (ORC). *Int. J. Prod. Econ.* **41**, 227–235 (1995).
17. Hung, T. C., Shai, T. Y. & Wang, S. K. A review of organic rankine cycles (ORCs) for the recovery of low-grade waste heat. *Energy* **22**, 661–667 (1997).
18. Liu, B.-T., Chien, K.-H. & Wang, C.-C. Effect of working fluids on organic Rankine cycle for waste heat recovery. *Energy* **29**, 1207–1217 (2004).
19. Yang, J. & Caillat, T. Thermoelectric Materials for Space and Automotive Power Generation. *MRS Bull.* **31**, 224–229 (2006).
20. Martínez, I. A. *et al.* Brownian Carnot engine. *Nat. Phys.* **12**, 67–70 (2016).
21. Verley, G., Esposito, M., Willaert, T. & Broeck, C. V. den. The unlikely Carnot efficiency. *Nat. Commun.* **5**, 4721 (2014).
22. Quan, H. T. Maximum efficiency of ideal heat engines based on a small system: Correction to the Carnot efficiency at the nanoscale. *Phys. Rev. E* **89**, 062134 (2014).
23. Thermodynamics: An Engineering Approach - With DVD 7th edition (9780077366742) - Textbooks.com. Available at: <http://www.textbooks.com/Thermodynamics-An-Engineering-Approach---With-DVD-7th-Edition/9780077366742/Yunus-Cengel.php>. (Accessed: 12th March 2017)
24. Sears, F. W. & Salinger, G. L. *Thermodynamics, Kinetic Theory, and Statistical Thermodynamics*. (Addison Wesley, 1975).
25. Giordano, N. *College Physics: Reasoning and Relationships*. (Cengage Learning, 2009).
26. Clarke, D. R., Oechsner, M. & Padture, N. P. Thermal-barrier coatings for more efficient gas-turbine engines. *MRS Bull.* **37**, 891–898 (2012).
27. Boyce, M. P. *Gas Turbine Engineering Handbook*. (Gulf Professional Publishing, 2002).
28. Paul, D. Thermoelectric Energy Harvesting. (2014). doi:10.5772/57092
29. Minnich, A. J., Dresselhaus, M. S., Ren, Z. F. & Chen, G. Bulk nanostructured thermoelectric materials: current research and future prospects. *Energy Environ. Sci.* **2**, 466–479 (2009).

30. Thermal Conductivity - Theory, Properties, and Applications | Terry M. Tritt | Springer.
31. Harman, T. C., Taylor, P. J., Walsh, M. P. & LaForge, B. E. Quantum dot superlattice thermoelectric materials and devices. *Science* **297**, 2229–2232 (2002).
32. Effective scattering cross-section in lattice thermal conductivity calculation with differential effective medium method. *AIP Adv.* **3**, 082116 (2013).
33. Zhao, L.-D., Dravid, V. P. & Kanatzidis, M. G. The panoscopic approach to high performance thermoelectrics. *Energy Environ. Sci.* **7**, 251–268 (2013).
34. Hicks, L. D. & Dresselhaus, M. S. Effect of quantum-well structures on the thermoelectric figure of merit. *Phys. Rev. B* **47**, 12727–12731 (1993).
35. Ohta, H. *et al.* Giant thermoelectric Seebeck coefficient of a two-dimensional electron gas in SrTiO₃. *Nat. Mater.* **6**, 129–134 (2007).
36. Electronic structure and thermoelectric properties of orthorhombic SrLiAs. *J. Appl. Phys.* **116**, 033705 (2014).
37. Thermoelectrics Handbook: Macro to Nano. *CRC Press* (2005). Available at: <https://www.crcpress.com/Thermoelectrics-Handbook-Macro-to-Nano/Rowe/p/book/9780849322648>. (Accessed: 12th March 2017)
38. Ma, Y. *et al.* Enhanced Thermoelectric Figure-of-Merit in p-Type Nanostructured Bismuth Antimony Tellurium Alloys Made from Elemental Chunks. *Nano Lett.* **8**, 2580–2584 (2008).
39. Bux, S. K., Fleurial, J.-P. & Kaner, R. B. Nanostructured materials for thermoelectric applications. *Chem. Commun.* **46**, 8311–8324 (2010).
40. Polarization field engineering of GaN/AlN/AlGaN superlattices for enhanced thermoelectric properties. *Appl. Phys. Lett.* **104**, 042106 (2014).
41. Zhang, Q., Sun, Y., Xu, W. & Zhu, D. Organic Thermoelectric Materials: Emerging Green Energy Materials Converting Heat to Electricity Directly and Efficiently. *Adv. Mater.* **26**, 6829–6851 (2014).
42. Wright, D. A. Thermoelectric Properties of Bismuth Telluride and its Alloys. *Nature* **181**, 834–834 (1958).
43. Thermoelectric Properties of n Type Bi₂Te₃ PbSe_{0.5}Te_{0.5} Segmented - Technische Informationsbibliothek (TIB). Available at: [https://www.tib.eu/en/search/id/BLSE%3ARN345765061/Thermoelectric-Properties-of-n-Type-Bi₂Te₃-PbSe_{0.5}-Te_{0.5}](https://www.tib.eu/en/search/id/BLSE%3ARN345765061/Thermoelectric-Properties-of-n-Type-Bi2Te3-PbSe0.5-Te0.5). (Accessed: 13th March 2017)
44. Zhu, P. *et al.* Enhanced thermoelectric properties of PbTe alloyed with Sb₂Te₃. *J. Phys. Condens. Matter* **17**, 7319 (2005).

45. Poudeu, P. F. P. *et al.* Nanostructures versus solid solutions: low lattice thermal conductivity and enhanced thermoelectric figure of merit in $\text{Pb}_{9.6}\text{Sb}_{0.2}\text{Te}_{10-x}\text{Se}_x$ bulk materials. *J. Am. Chem. Soc.* **128**, 14347–14355 (2006).
46. Poudeu, P. F. P. *et al.* High thermoelectric figure of merit and nanostructuring in bulk p-type $\text{Na}_{1-x}\text{Pb}_m\text{Sb}_y\text{Te}_{m+2}$. *Angew. Chem. Int. Ed Engl.* **45**, 3835–3839 (2006).
47. Russ, B., Glaudell, A., Urban, J. J., Chabinyk, M. L. & Segalman, R. A. Organic thermoelectric materials for energy harvesting and temperature control. *Nat. Rev. Mater.* **1**, 16050 (2016).
48. Bubnova, O. & Crispin, X. Towards polymer-based organic thermoelectric generators. *Energy Environ. Sci.* **5**, 9345–9362 (2012).
49. Hwang, S. *et al.* Solution-processed organic thermoelectric materials exhibiting doping-concentration-dependent polarity. *Phys. Chem. Chem. Phys.* **18**, 29199–29207 (2016).
50. Bubnova, O. *et al.* Optimization of the thermoelectric figure of merit in the conducting polymer poly(3,4-ethylenedioxythiophene). *Nat. Mater.* **10**, 429–433 (2011).
51. Kamarudin, M. A. *et al.* A Review on the Fabrication of Polymer-Based Thermoelectric Materials and Fabrication Methods. *Sci. World J.* **2013**, e713640 (2013).
52. Yoo, D., Lee, J. J., Park, C., Choi, H. H. & Kim, J.-H. N-type organic thermoelectric materials based on polyaniline doped with the aprotic ionic liquid 1-ethyl-3-methylimidazolium ethyl sulfate. *RSC Adv.* **6**, 37130–37135 (2016).
53. Moses, D. & Denenstien, A. Experimental determination of the thermal conductivity of a conducting polymer: Pure and heavily doped polyacetylene. *Phys. Rev. B* **30**, 2090–2097 (1984).
54. Skotheim, T. A. *Handbook of Conducting Polymers, Second Edition*,. (CRC Press, 1997).
55. Zhang, K., Qiu, J. & Wang, S. Thermoelectric properties of PEDOT nanowire/PEDOT hybrids. *Nanoscale* **8**, 8033–8041 (2016).
56. Kim, B., Shin, H., Park, T., Lim, H. & Kim, E. NIR-sensitive poly(3,4-ethylenedioxy-selenophene) derivatives for transparent photo-thermo-electric converters. *Adv. Mater. Deerfield Beach Fla* **25**, 5483–5489 (2013).
57. Kim, G.-H., Shao, L., Zhang, K. & Pipe, K. P. Engineered doping of organic semiconductors for enhanced thermoelectric efficiency. *Nat. Mater.* **12**, 719–723 (2013).
58. Hosseini, T., Omari, M. & Kouklin, N. A. Carbon Nanotube IR Photothermovoltaic Devices: Power, Fill Factor, and Transient Response. *IEEE Electron Device Lett.* **34**, 924–926 (2013).

59. On plasmon-induced photocurrent and doping of metal-patterned graphene. *Appl. Phys. Lett.* **105**, 043104 (2014).
60. Hossain, M. S., Al-Dirini, F., Hossain, F. M. & Skafidas, E. High Performance Graphene Nano-ribbon Thermoelectric Devices by Incorporation and Dimensional Tuning of Nanopores. *Sci. Rep.* **5**, 11297 (2015).
61. Mahmoud, L. *et al.* Characterization of a Graphene-Based Thermoelectric Generator Using a Cost-Effective Fabrication Process. *Energy Procedia* **75**, 615–620 (2015).
62. Hewitt, C. A. & Carroll, D. L. Carbon Nanotube-Based Polymer Composite Thermoelectric Generators. in *Polymer Composites for Energy Harvesting, Conversion, and Storage* **1161**, 191–211 (American Chemical Society, 2014).
63. Al-Saleh, M. H. Electrical and mechanical properties of graphene/carbon nanotube hybrid nanocomposites. *Synth. Met.* **209**, 41–46 (2015).
64. Sevinçli, H., Sevik, C., Çağın, T. & Cuniberti, G. A bottom-up route to enhance thermoelectric figures of merit in graphene nanoribbons. *Sci. Rep.* **3**, 1228 (2013).
65. Anno, Y., Imakita, Y., Takei, K., Akita, S. & Arie, T. Enhancement of graphene thermoelectric performance through defect engineering. *2D Mater.* **4**, 025019 (2017).
66. Yang, J. *et al.* Reduced Graphene Oxide (rGO)-Wrapped Fullerene (C60) Wires. *ACS Nano* **5**, 8365–8371 (2011).
67. Estili, M., Wu, W.-W., Khazaei, M. & Sakka, Y. Mechanically reliable thermoelectric (TE) nanocomposites by dispersing and embedding TE-nanostructures inside a tetragonal ZrO₂ matrix: the concept and experimental demonstration in graphene oxide–3YSZ system. *Sci. Technol. Adv. Mater.* **15**, 014201 (2014).
68. Eslamian, M. Inorganic and Organic Solution-Processed Thin Film Devices. *Nano-Micro Lett.* **9**, 3 (2017).
69. Bae, E. J., Kang, Y. H., Jang, K.-S. & Cho, S. Y. Enhancement of Thermoelectric Properties of PEDOT:PSS and Tellurium-PEDOT:PSS Hybrid Composites by Simple Chemical Treatment. *Sci. Rep.* **6**, 18805 (2016).
70. Zhu, Z., Liu, C., Jiang, F., Xu, J. & Liu, E. Effective treatment methods on PEDOT:PSS to enhance its thermoelectric performance. *Synth. Met.* **225**, 31–40 (2017).
71. Cowen, L. M., Atoyo, J., Carnie, M. J., Baran, D. & Schroeder, B. C. Review—Organic Materials for Thermoelectric Energy Generation. *ECS J. Solid State Sci. Technol.* **6**, N3080–N3088 (2017).
72. Yoo, D., Kim, J. & Kim, J. H. Direct synthesis of highly conductive poly(3,4-ethylenedioxythiophene):poly(4-styrenesulfonate) (PEDOT:PSS)/graphene composites and their applications in energy harvesting systems. *Nano Res.* **7**, 717–730 (2014).

73. Nakai, Y. *et al.* Giant Seebeck coefficient in semiconducting single-wall carbon nanotube film. *Appl. Phys. Express* **7**, 025103 (2014).
74. Xu, B., Yin, J. & Liu, Z. Phonon Scattering and Electron Transport in Single Wall Carbon Nanotube. (2013). doi:10.5772/51451
75. Benchirouf, A. *et al.* Electrical properties of multi-walled carbon nanotubes/PEDOT:PSS nanocomposites thin films under temperature and humidity effects. *Sens. Actuators B Chem.* **224**, 344–350 (2016).
76. Yu, C., Choi, K., Yin, L. & Grunlan, J. C. Correction to Light-Weight Flexible Carbon Nanotube Based Organic Composites with Large Thermoelectric Power Factors. *ACS Nano* **7**, 9506–9506 (2013).
77. Toshima, N. *et al.* Novel Hybrid Organic Thermoelectric Materials: Three-Component Hybrid Films Consisting of a Nanoparticle Polymer Complex, Carbon Nanotubes, and Vinyl Polymer. *Adv. Mater.* **27**, 2246–2251 (2015).
78. Cho, J. *et al.* Electrochemically tunable thermal conductivity of lithium cobalt oxide. *Nat. Commun.* **5**, 4035 (2014).
79. Roger, M. *et al.* Patterning of sodium ions and the control of electrons in sodium cobaltate. *Nature* **445**, 631–634 (2007).
80. Wu, T., Tyson, T., Zhang, H. & Abeykoon, M. Temperature Dependent Structure of Thermoelectric $\text{Ca}_3\text{Co}_4\text{O}_9$. (2016).
81. Lemal, S., Varignon, J., Bilc, D. I. & Ghosez, P. Thermoelectric properties of layered calcium cobaltite $\text{Ca}_3\text{Co}_4\text{O}_9$ from hybrid functional first-principles calculations. *Phys. Rev. B* **95**, 075205 (2017).
82. Park, K., Hakeem, D. A. & Cha, J. S. Synthesis and structural properties of thermoelectric $\text{Ca}_{3-x}\text{Ag}_x\text{Co}_4\text{O}_{9+\delta}$ powders. *Dalton Trans.* **45**, 6990–6997 (2016).
83. Lu, Q. M., Zhang, J. X., Zhang, Q. Y., Liu, Y. Q. & Liu, D. M. Improved Thermoelectric Properties of $\text{Ca}_{3-x}\text{Ba}_x\text{Co}_4\text{O}_9$ ($x=0-0.4$) Bulks by Sol-Gel and SPS Method. in *2006 25th International Conference on Thermoelectrics* 66–69 (2006). doi:10.1109/ICT.2006.331271
84. Lee, S., Wilke, R. H. T., Trolier-McKinstry, S., Zhang, S. & Randall, C. A. $\text{Sr}_x\text{Ba}_{1-x}\text{Nb}_2\text{O}_{6-\delta}$ Ferroelectric-thermoelectrics: Crystal anisotropy, conduction mechanism, and power factor. *Appl. Phys. Lett.* **96**, 031910 (2010).
85. Liou, Y.-C., Tsai, W.-C., Yu, J.-Y. & Tsai, H.-C. Effects of Ti addition on properties of $\text{Sr}_2\text{Nb}_2\text{O}_7$ thermoelectric ceramics. *Ceram. Int.* **41**, 7036–7041 (2015).
86. Fergus, J. W. Oxide materials for high temperature thermoelectric energy conversion. *J. Eur. Ceram. Soc.* **32**, 525–540 (2012).

87. Terasaki, I. High-temperature oxide thermoelectrics. *J. Appl. Phys.* **110**, 053705 (2011).
88. Ohtaki, M. Oxide Thermoelectric Materials for Heat-to-Electricity Direct Energy Conversion. (2009).
89. Hasan, M. Z. & Kane, C. L. Colloquium. *Rev. Mod. Phys.* **82**, 3045–3067 (2010).
90. Topological Insulator Materials. *J. Phys. Soc. Jpn.* **82**, 102001 (2013).
91. Takahashi, R. & Murakami, S. Thermoelectric transport in topological insulators. *Semicond. Sci. Technol.* **27**, 124005 (2012).
92. Pal, K., Anand, S. & Waghmare, U. V. Thermoelectric properties of materials with nontrivial electronic topology. *J. Mater. Chem. C* **3**, 12130–12139 (2015).
93. Guo, S.-D. & Qiu, L. Thermoelectric properties of topological insulator BaSn 2. *J. Phys. Appl. Phys.* **50**, 015101 (2017).
94. Thermoelectric properties of topological insulator Bi₂Te₃, Sb₂Te₃, and Bi₂Se₃ thin film quantum wells. *Appl. Phys. Lett.* **105**, 123117 (2014).
95. Klitzing, K. v., Dorda, G. & Pepper, M. New Method for High-Accuracy Determination of the Fine-Structure Constant Based on Quantized Hall Resistance. *Phys. Rev. Lett.* **45**, 494–497 (1980).
96. Wen, X.-G. Topological orders and edge excitations in fractional quantum Hall states. *Adv. Phys.* **44**, 405–473 (1995).
97. Thouless, D. J., Kohmoto, M., Nightingale, M. P. & den Nijs, M. Quantized Hall Conductance in a Two-Dimensional Periodic Potential. *Phys. Rev. Lett.* **49**, 405–408 (1982).
98. Singleton, J. *Band Theory and Electronic Properties of Solids*. (Oxford University Press, 2001).
99. Band Theory and Electronic Properties of Solids. *Phys. Today* **55**, 61–62 (2002).
100. Butcher, P. N., March, N. H. & Tosi, M. P. *Crystalline Semiconducting Materials and Devices*. (Springer Science & Business Media, 2013).
101. Ziman, J. M. *Principles of the Theory of Solids*. (Cambridge University Press, 1979).
102. (Solid State Physics) Neil W. Ashcroft, N. David Mermin-Brooks Cole (1976) | Electron | Metals. *Scribd* Available at: <https://www.scribd.com/doc/207078972/Solid-State-Physics-Neil-W-Ashcroft-N-David-Mermin-Brooks-Cole-1976>. (Accessed: 13th March 2017)
103. Qi, X.-L. & Zhang, S.-C. Topological insulators and superconductors. *Rev. Mod. Phys.* **83**, 1057–1110 (2011).

104. Bansil, A., Lin, H. & Das, T. Colloquium. *Rev. Mod. Phys.* **88**, 021004 (2016).
105. Weng, H., Dai, X. & Fang, Z. Exploration and prediction of topological electronic materials based on first-principles calculations. *MRS Bull.* **39**, 849–858 (2014).
106. *A Short Course on Topological Insulators - Band Structure* | János K. Asbóth | Springer.
107. Zhu, Z., Cheng, Y. & Schwingenschlögl, U. Band inversion mechanism in topological insulators: A guideline for materials design. *Phys. Rev. B* **85**, 235401 (2012).
108. Zhang, H. *et al.* Topological insulators in Bi₂Se₃, Bi₂Te₃ and Sb₂Te₃ with a single Dirac cone on the surface. *Nat. Phys.* **5**, 438–442 (2009).
109. Yan, B. *et al.* Theoretical prediction of topological insulators in thallium-based III-V-VI 2 ternary chalcogenides. *EPL Europhys. Lett.* **90**, 37002 (2010).
110. Hatsugai, Y. Chern number and edge states in the integer quantum Hall effect. *Phys. Rev. Lett.* **71**, 3697–3700 (1993).
111. Huckestein, B. Scaling theory of the integer quantum Hall effect. *Rev. Mod. Phys.* **67**, 357–396 (1995).
112. Gumbs, G. & Huang, D. Integer Quantum Hall Effect. in *Properties of Interacting Low-Dimensional Systems* 197–213 (Wiley-VCH Verlag GmbH & Co. KGaA, 2011). doi:10.1002/9783527638154.ch9
113. MacDonald, A. H. & Středa, P. Quantized Hall effect and edge currents. *Phys. Rev. B* **29**, 1616–1619 (1984).
114. Topological Insulators: The Physics of Spin Helicity in Quantum Transport. *CRC Press* (2015). Available at: <https://www.crcpress.com/Topological-Insulators-The-Physics-of-Spin-Helicity-in-Quantum-Transport/Tkachov/p/book/9789814613255>. (Accessed: 13th March 2017)
115. The quantum spin Hall effect and topological insulators. *Phys. Today* **63**, 33–38 (2009).
116. The Quantum Spin Hall Effect: Theory and Experiment. *J. Phys. Soc. Jpn.* **77**, 031007 (2008).
117. Yang, Y. *et al.* Time-Reversal-Symmetry-Broken Quantum Spin Hall Effect. *Phys. Rev. Lett.* **107**, 066602 (2011).
118. Moore, J. E. The birth of topological insulators. *Nature* **464**, 194–198 (2010).
119. Bernevig, B. A., Hughes, T. L. & Zhang, S.-C. Quantum Spin Hall Effect and Topological Phase Transition in HgTe Quantum Wells. *Science* **314**, 1757–1761 (2006).

120. Kato, Y. K., Myers, R. C., Gossard, A. C. & Awschalom, D. D. Observation of the Spin Hall Effect in Semiconductors. *Science* **306**, 1910–1913 (2004).
121. Bernevig, B. A. & Zhang, S.-C. Quantum Spin Hall Effect. *Phys. Rev. Lett.* **96**, 106802 (2006).
122. Kane, C. L. & Mele, E. J. Z_2 Topological Order and the Quantum Spin Hall Effect. *Phys. Rev. Lett.* **95**, 146802 (2005).
123. Wu, C., Bernevig, B. A. & Zhang, S.-C. Helical Liquid and the Edge of Quantum Spin Hall Systems. *Phys. Rev. Lett.* **96**, 106401 (2006).
124. Sheng, D. N., Weng, Z. Y., Sheng, L. & Haldane, F. D. M. Quantum Spin-Hall Effect and Topologically Invariant Chern Numbers. *Phys. Rev. Lett.* **97**, 036808 (2006).
125. Moore, J. E. & Balents, L. Topological invariants of time-reversal-invariant band structures. *Phys. Rev. B* **75**, 121306 (2007).
126. Roy, R. Z_2 classification of quantum spin Hall systems: An approach using time-reversal invariance. *Phys. Rev. B* **79**, 195321 (2009).
127. Stolz, G. An Introduction to the Mathematics of Anderson Localization. *ArXiv11042317 Math-Ph* (2011).
128. Hundertmark, D. A Short Introduction to Anderson Localization. in *Analysis and Stochastics of Growth Processes and Interface Models* (eds. Mörters, P., Moser, R., Penrose, M., Schwetlick, H. & Zimmer, J.) 194–218 (Oxford University Press, 2008). doi:10.1093/acprof:oso/9780199239252.003.0009
129. Castro, E. V., López-Sancho, M. P. & Vozmediano, M. A. H. Anderson localization and topological transition in Chern insulators. *Phys. Rev. B* **92**, 085410 (2015).
130. Classification of Topological Insulators and Superconductors. *AIP Conf. Proc.* **1134**, 10–21 (2009).
131. Dresselhaus, G. Spin-Orbit Coupling Effects in Zinc Blende Structures. *Phys. Rev.* **100**, 580–586 (1955).
132. Gmitra, M., Konschuh, S., Ertler, C., Ambrosch-Draxl, C. & Fabian, J. Band-structure topologies of graphene: Spin-orbit coupling effects from first principles. *Phys. Rev. B* **80**, 235431 (2009).
133. Kokurin, I. A. Effect of spin-orbit coupling on spectral and transport properties of tubular electron gas in InAs nanowires. *Phys. E Low-Dimens. Syst. Nanostructures* **74**, 264–269 (2015).

134. Dai, D. *et al.* Analysis of the effect of spin-orbit coupling on the electronic structure and excitation spectrum of the Bi_2^{2-} anion in $(\text{K-crypt})_2\text{Bi}_2$ on the basis of relativistic electronic structure calculations. *J. Phys. Chem. A* **109**, 1675–1683 (2005).
135. Li, Y.-D., Shen, Y., Li, Y., Zhao, J. & Chen, G. The effect of spin-orbit coupling on the effective-spin correlation in YbMgGaO_4 . *ArXiv160806445 Cond-Mat* (2016).
136. Fu, L. & Kane, C. L. Topological insulators with inversion symmetry. *Phys. Rev. B* **76**, 045302 (2007).
137. Hsieh, D. *et al.* A topological Dirac insulator in a quantum spin Hall phase. *Nature* **452**, 970–974 (2008).
138. Qu, D.-X., Hor, Y. S., Xiong, J., Cava, R. J. & Ong, N. P. Quantum Oscillations and Hall Anomaly of Surface States in the Topological Insulator Bi_2Te_3 . *Science* **329**, 821–824 (2010).
139. Chen, Y. L. *et al.* Experimental realization of a three-dimensional topological insulator, Bi_2Te_3 . *Science* **325**, 178–181 (2009).
140. Neupane, M. *et al.* Oscillatory surface dichroism of the insulating topological insulator $\text{Bi}_2\text{Te}_2\text{Se}$. *Phys. Rev. B* **88**, 165129 (2013).
141. Okada, Y. *et al.* Observation of Dirac Node Formation and Mass Acquisition in a Topological Crystalline Insulator. *Science* **341**, 1496–1499 (2013).
142. Wray, L. A. *et al.* Chemically gated electronic structure of a superconducting doped topological insulator system. *J. Phys. Conf. Ser.* **449**, 012037 (2013).
143. Bonderson, P., Nayak, C. & Qi, X.-L. A time-reversal invariant topological phase at the surface of a 3D topological insulator. *J. Stat. Mech. Theory Exp.* **2013**, P09016 (2013).
144. Hasan, M. Z. & Moore, J. E. Three-Dimensional Topological Insulators. <http://dx.doi.org/10.1146/annurev-conmatphys-062910-140432> (2011). Available at: <http://www.annualreviews.org/doi/10.1146/annurev-conmatphys-062910-140432>. (Accessed: 13th March 2017)
145. Liu, Z., Jiang, L. & Zheng, Y. Band structure of a three-dimensional topological insulator quantum wire in the presence of a magnetic field. *J. Phys. Condens. Matter* **28**, 275501 (2016).
146. Particles with Spin 1/2 and the Dirac Equation. in *Quantum Physics* 505–572 (Springer Berlin Heidelberg, 2007). doi:10.1007/978-3-540-49972-5_9
147. Greiner, P. D. W. A Wave Equation for Spin-1/2 Particles: The Dirac Equation. in *Relativistic Quantum Mechanics* 99–126 (Springer Berlin Heidelberg, 1997). doi:10.1007/978-3-662-03425-5_2

148. Pariari, A. & Mandal, P. Coexistence of topological Dirac fermions on the surface and three-dimensional Dirac cone state in the bulk of ZrTe_5 single crystal. *Sci. Rep.* **7**, 40327 (2017).
149. Kalesaki, E. *et al.* Dirac Cones, Topological Edge States, and Nontrivial Flat Bands in Two-Dimensional Semiconductors with a Honeycomb Nanogeometry. *Phys. Rev. X* **4**, 011010 (2014).
150. Li, G., Yan, B., Thomale, R. & Hanke, W. Topological nature and the multiple Dirac cones hidden in Bismuth high-Tc superconductors. *Sci. Rep.* **5**, 10435 (2015).
151. Lin, H. *et al.* Single-Dirac-Cone topological surface states in TlBiSe₂ class of Topological Insulators. *Phys. Rev. Lett.* **105**, (2010).
152. Cao, H. *et al.* Structural and electronic properties of highly doped topological insulator Bi₂Se₃ crystals. *Phys. Status Solidi RRL – Rapid Res. Lett.* **7**, 133–135 (2013).
153. Neupane, M. *et al.* Fermi-surface topology and low-lying electronic structure of the iron-based superconductor $\text{Ca}_{10}(\text{Pt}_3\text{As}_8)(\text{Fe}_2\text{As}_2)_5$. *Phys. Rev. B* **85**, 094510 (2012).
154. Xia, Y. *et al.* Observation of a large-gap topological-insulator class with a single Dirac cone on the surface. *Nat. Phys.* **5**, 398–402 (2009).
155. Sato, T. *et al.* Direct Evidence for the Dirac-Cone Topological Surface States in the Ternary Chalcogenide TlBiSe₂. *Phys. Rev. Lett.* **105**, 136802 (2010).
156. Kuroda, K. *et al.* Experimental Realization of a Three-Dimensional Topological Insulator Phase in Ternary Chalcogenide TlBiSe₂. *Phys. Rev. Lett.* **105**, 146801 (2010).
157. Chen, Y. L. *et al.* Single Dirac Cone Topological Surface State and Unusual Thermoelectric Property of Compounds from a New Topological Insulator Family. *Phys. Rev. Lett.* **105**, 266401 (2010).
158. Souma, S. *et al.* Topological Surface States in Lead-Based Ternary Telluride $\text{Pb}(\text{Bi}_{1-x}\text{Sb}_x)_2\text{Te}_4$. *Phys. Rev. Lett.* **108**, 116801 (2012).
159. Kuroda, K. *et al.* Experimental Verification of PbBi_2Te_4 as a 3D Topological Insulator. *Phys. Rev. Lett.* **108**, 206803 (2012).
160. Brüne, C. *et al.* Quantum Hall Effect from the Topological Surface States of Strained Bulk HgTe. *Phys. Rev. Lett.* **106**, 126803 (2011).
161. Steed, J. W. Should solid-state molecular packing have to obey the rules of crystallographic symmetry? *CrystEngComm* **5**, 169–179 (2003).
162. Yang, B.-J. & Nagaosa, N. Classification of stable three-dimensional Dirac semimetals with nontrivial topology. *Nat. Commun.* **5**, 4898 (2014).

163. Young, S. M. & Kane, C. L. Dirac Semimetals in Two Dimensions. *Phys. Rev. Lett.* **115**, 126803 (2015).
164. Li, G., Yan, B., Wang, Z. & Held, K. Topological Dirac semimetal phase in Pd and Pt oxides. *Phys. Rev. B* **95**, 035102 (2017).
165. Young, S. M. *et al.* Dirac Semimetal in Three Dimensions. *Phys. Rev. Lett.* **108**, 140405 (2012).
166. Wieder, B. J., Kim, Y., Rappe, A. M. & Kane, C. L. Double Dirac Semimetals in Three Dimensions. *Phys. Rev. Lett.* **116**, 186402 (2016).
167. Tominaga, J., Kolobov, A. V., Fons, P., Nakano, T. & Murakami, S. Ferroelectric Order Control of the Dirac-Semimetal Phase in GeTe-Sb₂Te₃ Superlattices. *Adv. Mater. Interfaces* **1**, (2014).
168. Gibson, Q. D. *et al.* Three-dimensional Dirac semimetals: Design principles and predictions of new materials. *Phys. Rev. B* **91**, 205128 (2015).
169. Liu, Z. K. *et al.* A stable three-dimensional topological Dirac semimetal Cd₃As₂. *Nat. Mater.* **13**, 677–681 (2014).
170. Neupane, M. *et al.* Observation of a three-dimensional topological Dirac semimetal phase in high-mobility Cd₃As₂. *Nat. Commun.* **5**, 3786 (2014).
171. Ali, M. N. *et al.* The Crystal and Electronic Structures of Cd₃As₂, the Three-Dimensional Electronic Analogue of Graphene. *Inorg. Chem.* **53**, 4062–4067 (2014).
172. Madou, M. J., Perez-Gonzalez, V. H. & Pramanick, B. *Carbon: The Next Silicon?: Book 1 - Fundamentals*. (Momentum Press, 2016).
173. Castro Neto, A. H., Guinea, F., Peres, N. M. R., Novoselov, K. S. & Geim, A. K. The electronic properties of graphene. *Rev. Mod. Phys.* **81**, 109–162 (2009).
174. Resources, M. A., Information. *Nanotechnology: Concepts, Methodologies, Tools, and Applications: Concepts, Methodologies, Tools, and Applications*. (IGI Global, 2014).
175. Kunschuh, S., Gmitra, M. & Fabian, J. Tight-binding theory of the spin-orbit coupling in graphene. *Phys. Rev. B* **82**, 245412 (2010).
176. Bolotin, K. I. *et al.* Ultrahigh electron mobility in suspended graphene. *Solid State Commun.* **146**, 351–355 (2008).
177. Electron mobility calculation for graphene on substrates. *J. Appl. Phys.* **116**, 083703 (2014).
178. Liu, Z. K. *et al.* Discovery of a Three-Dimensional Topological Dirac Semimetal, Na₃Bi. *Science* **343**, 864–867 (2014).

179. Singh, B. *et al.* Topological electronic structure and Weyl semimetal in the $\text{TlBiSe}_{1-x}\text{Sb}_x$ class of semiconductors. *Phys. Rev. B* **86**, 115208 (2012).
180. Novak, M., Sasaki, S., Segawa, K. & Ando, Y. Large linear magnetoresistance in the Dirac semimetal TlBiSSe . *Phys. Rev. B* **91**, 041203 (2015).
181. Orlita, M. *et al.* Observation of three-dimensional massless Kane fermions in a zinc-blende crystal. *Nat. Phys.* **10**, 233–238 (2014).
182. Magneto-transport studies on $\text{Bi}_2\text{Te}_{2+x}\text{Se}_{1-x}$ ($x = 0.05$ and 0.10) topological insulators. *AIP Adv.* **6**, 095215 (2016).
183. Bulk crystal growth and electronic characterization of the 3D Dirac semimetal Na_3Bi . *APL Mater.* **3**, 041504 (2015).
184. Xiong, J. *et al.* Evidence for the chiral anomaly in the Dirac semimetal Na_3Bi . *Science* **350**, 413–416 (2015).
185. Wang, Z. *et al.* Dirac semimetal and topological phase transitions in A_3Bi ($\text{A}=\text{Na}, \text{K}, \text{Rb}$). *Phys. Rev. B* **85**, 195320 (2012).
186. Liang, T. *et al.* Ultrahigh mobility and giant magnetoresistance in the Dirac semimetal Cd_3As_2 . *Nat. Mater.* **14**, 280–284 (2015).
187. Yi, H. *et al.* Evidence of Topological Surface State in Three-Dimensional Dirac Semimetal Cd_3As_2 . *Sci. Rep.* **4**, 6106 (2014).
188. Wang, Z., Weng, H., Wu, Q., Dai, X. & Fang, Z. Three-dimensional Dirac semimetal and quantum transport in Cd_3As_2 . *Phys. Rev. B* **88**, 125427 (2013).
189. Brahlek, M. *et al.* Topological-Metal to Band-Insulator Transition in $(\text{Bi}_{1-x}\text{In}_x)_2\text{Se}_3$ Thin Films. *Phys. Rev. Lett.* **109**, 186403 (2012).
190. Guo, S.-D. Pressure-induced semiconductor-to-metal transition in Mg_2Sn with the modified Becke-Johnson potential. *EPL Europhys. Lett.* **109**, 57002 (2015).
191. Dziawa, P. *et al.* Topological crystalline insulator states in $\text{Pb}_{1-x}\text{Sn}_x\text{Se}$. *Nat. Mater.* **11**, 1023–1027 (2012).
192. Chen, Z.-G. *et al.* Scalable Growth of High Mobility Dirac Semimetal Cd_3As_2 Microbelts. *Nano Lett.* **15**, 5830–5834 (2015).
193. Dowgiałło-Plenkiewicz, B. & Plenkiewicz, P. Inverted band structure of Cd_3As_2 . *Phys. Status Solidi B* **94**, K57–K60 (1979).
194. Aubin, M. J., Caron, L. G. & Jay-Gerin, J. P. Band structure of cadmium arsenide at room temperature. *Phys. Rev. B* **15**, 3872–3878 (1977).

195. Wood, D. M. & Zunger, A. Electronic structure of generic semiconductors: Antifluorite silicide and III-V compounds. *Phys. Rev. B* **34**, 4105–4120 (1986).
196. Jay-Gerin, J.-P., Aubin, M. J. & Caron, L. G. The electron mobility and the static dielectric constant of Cd₃As₂ at 4.2 K. *Solid State Commun.* **21**, 771–774 (1977).
197. Zhou, T., Zhang, C., Zhang, H., Xiu, F. & Yang, Z. Enhanced thermoelectric properties of the Dirac semimetal Cd₃As₂. *Inorg. Chem. Front.* **3**, 1637–1643 (2016).
198. Zhang, C. *et al.* Unexpected low thermal conductivity and large power factor in Dirac semimetal Cd₃As₂. *Chin. Phys. B* **25**, 017202 (2016).
199. Das Sarma, S., Hwang, E. H. & Min, H. Carrier screening, transport, and relaxation in three-dimensional Dirac semimetals. *Phys. Rev. B* **91**, 035201 (2015).
200. Pariari, A., Khan, N., Singha, R., Satpati, B. & Mandal, P. Tuning the scattering mechanism in the three-dimensional Dirac semimetal Cd₃As₂. *Phys. Rev. B* **94**, 165139 (2016).
201. Enhanced boundary-scattering of electrons and phonons in nanograined zinc oxide. *J. Appl. Phys.* **108**, 053721 (2010).

Chapter 2.

Synthesis of crystalline Cd_3As_2 platelets

2.1 Background

As discussed in Chapter 1, the unique band structure and inherent exotic physical properties originated from Dirac fermions with linear band dispersion has made Dirac materials, such as graphene¹ and topological insulators,² promising candidates for the next generation electronic and spintronic devices. Among the Dirac materials, the emerging three-dimensional (3D) Dirac semimetals, in particular Cd_3As_2 ³ and Na_3Bi ⁴ have become the subject of increasing interest due to the fact that not only do they exhibit unexpected properties as a result of their nontrivial electronic band structure, but they can also be a versatile platform for the systematic study of unusual quantum phase transitions between rich topological quantum states by breaking time reversal symmetry or inversion symmetry.⁴⁻⁸ Compared with the air-sensitive Na_3Bi , Cd_3As_2 tends to be much stable at room temperature with a high chemical stability against oxidation,⁹ making it an ideal system for synthesis and studying 3D Dirac materials.

Soon after the unique properties of Cd_3As_2 were identified theoretically, such as ultrahigh electron mobility,^{10,11} large thermopower, quantum linear magnetoresistance up to room temperature, large negative magnetoresistance due to its novel bulk band structure,^{3,12-14} quantum spin Hall effect in its quantum-well structure,^{12,15} and possible topological superconductivity when doped,^{3,16} several experimental methods were employed to verify these exotic properties. The angle-resolved photoemission spectroscopy (ARPES),^{4,17-19} scanning tunneling microscopy (STM) experiments,²⁰ point contact experiments^{21,22}, and the high-pressure resistance measurements^{7,23-25} are among the techniques used and reported prior.

All these studies relied on the high-quality crystals prepared through various techniques such as flux method,^{11,26–29} static sublimation and Piper-Polich methods³⁰, and crystallization from the melt faces (Bridgman Method)³¹. However, in addition to be time consuming, the need for solvent (flux method), cracking and disintegration of crystals (static sublimation and Piper-Polich methods), phase change and formation of polycrystals with grains of various dimensions (Bridgman Method), and other drawbacks had hindered the research expansion and future practical applications. In general, there are many technical difficulties in realizing single crystals of the II_3V_2 compounds, especially Cd_3As_2 due to the solid-solid phase transitions and decomposition at the melting temperature.³² Given the melting point of 721 °C for Cd_3As_2 , melt-based crystal growth techniques have to be ruled out from consideration. Pulsed-laser evaporation was offered by Dubowski and Williams as an alternative route³³, but the resultant samples showed highly reduced, i.e., polycrystalline and amorphous quality.

Among the suggested alternative methods, synthesis methods based on vapor deposition have shown to be a promising pathway towards scalable fabrication of high quality Cd_3As_2 crystals. Hrubý and Petrová described a method of preparation of Cd_3As_2 single crystals employing transport reaction in vapor phase without transport gas, and determined optimum conditions for growth of the crystals with the average temperature and the temperature gradient of 535 °C and 3.3 °C/cm, respectively.³⁴ More recently, Chen et al. reported a chemical vapor deposition (CVD) method to fabricate high-quality Cd_3As_2 belt-like crystals exhibiting a length up to millimeter with smooth surfaces by placing the Cd_3As_2 precursor at around 760 °C.²⁶ In another study, Li et al. fabricated crystalline Cd_3As_2 nanostructures with various morphologies, including triangular, hexagonal, octahedral, and star-like shapes with lateral dimensions ranging from several hundred nanometers to tens of micrometers via a vapor–solid growth mechanism.³⁵

Binary cadmium arsenide that solidifies as Cd_3As_2 is known to undergo multiple polymorphic solid–solid transitions $\beta \rightarrow \alpha'' \rightarrow \alpha' \rightarrow \alpha$ at temperatures of 578, 475, and 225 °C, respectively; therefore, to avoid any phase transitions during the growth process, the growth temperature should be limited to 225 °C.

With the above considerations, in this work, a low- T chemical-vapor deposition route was used to grow Cd_3As_2 platelets up to cm size in a horizontally oriented hot-wall atmospheric pressure chemical vapor deposition (CVD) reactor. The resultant products were subject to visual and optical microscope investigation followed by a series of elemental and structural analysis through energy dispersive X-ray spectroscopy (EDS), Raman spectroscopy, and transmission electron microscopy (TEM), the results of which are presented in the following sections. Before extending on the details of the synthesis and characterization of Cd_3As_2 crystal, we first briefly review the chemical vapor deposition method in the following subsection.

2.1.1 Chemical Vapor Deposition technique

The chemical vapor deposition (CVD) is a widely used material-processing technology that combines different scientific disciplines such as chemistry, physics, materials science, engineering and microelectronics to produce high quality, high-performance, solid materials such as thin films, nanostructures like nanowires and quantum dots, high purity bulk crystalline materials and powders, as well as composite materials from chemical precursors in the vapor phase. The chemical reactions of precursor species occur both in the gas phase and on the substrate. Reactions can be promoted or initiated by heat (thermal CVD), higher frequency radiation such as UV (photo-assisted CVD) or plasma (plasma-enhanced CVD).

In its simplest incarnation, CVD involves flowing a precursor gas or gases into a chamber containing one or more heated objects to be coated. Chemical reactions occur on and near the hot surfaces, resulting in the deposition of a thin film on the surface. This is accompanied by the production of chemical by-products that are exhausted out of the chamber along with unreacted precursor gases. The key steps of the basic physicochemical steps in an overall CVD reaction are as follows:^{36,37}

1. Evaporation and transport of reagents (i.e. precursors) in the bulk gas flow region into the reactor;
2. Gas phase reactions of precursors in the reaction zone to produce reactive intermediates and gaseous by-products;
3. Mass transport of reactants to the substrate surface;
4. Adsorption of the reactants on the substrate surface;
5. Surface diffusion to growth sites, nucleation and surface chemical reactions leading to film or nanostructure formation;
6. Desorption and mass transport of remaining fragments of the decomposition away from the reaction zone.

There are many variants of CVD. It is done in hot-wall reactors and cold-wall reactors, at sub-Torr total pressures to above-atmospheric pressures, with and without carrier gases, and at temperatures typically ranging from 200-1600°C. A number of forms of CVD are in wide use and these processes differ in the means by which chemical reactions are initiated (e.g., activation process) and process conditions. CVD encompasses a variety of deposition techniques, including a range of thermal processes, enhanced processes involving ions, lasers, hot filaments, or combustion reactions to increase deposition rates and/or lower deposition temperatures, plasma

enhanced CVD (PECVD), photon- initiated CVD, and atomic layer deposition (ALD),³⁶ CVD has a number of advantages as a method for depositing thin films. One of the primary advantages is that CVD is generally more conformal than physical vapor deposition, meaning that it covers a rough surface relatively uniformly, tracking the morphology rather than resulting in thin, low quality coatings on vertical walls of the substrate, as is the case for physical vapor deposition (PVD) techniques, such as sputtering or evaporation, which generally require a line-of-sight between the surface to be coated and the source. Another advantage of CVD is that, in addition to the wide variety of materials that can be deposited, they can be deposited with very high purity. This results from the relative ease with which impurities are removed from gaseous precursors using distillation techniques. Other advantages of CVD technique include relatively high deposition rates, and that it does not require very high vacuum levels, it can generally process substrates in larger batches than evaporation, and is more forgiving in terms of its tolerance for precision in the process conditions.³⁹

CVD also has a number of disadvantages. One of the primary disadvantages of the CVD method lies in the properties of the precursors. Ideally, the precursors need to be volatile at near-room temperatures. This is non-trivial for a number of elements in the periodic table, although the use of metal-organic precursors has eased this situation. CVD precursors can also be highly toxic ($\text{Ni}(\text{CO})_4$), explosive (B_2H_6), or corrosive (SiCl_4). The byproducts of CVD reactions can also be hazardous (CO , H_2 , or HF). Some of these precursors, especially the metal-organic precursors, can also be quite costly. The other major disadvantage is the fact that the films are usually deposited at elevated temperatures. This puts some restrictions on the kind of substrates that can be coated. More importantly, it leads to stresses in films deposited on materials with different thermal expansion coefficients, which can cause mechanical instabilities in the deposited films.⁴⁰

For microelectronics manufacturing the benefits generally outweigh the problems. Thus, most device makers use CVD when possible rather than, for example, MBE.

2.2 Experimental Procedure

In this work a low temperature chemical-vapor deposition (CVD) route was used to grow crystalline Cd_3As_2 platelets up to cm size in a horizontally oriented hot-wall chemical vapor deposition (CVD) reactor in atmospheric pressure. Pure, polycrystalline Cd_3As_2 chunks were used as a precursor, quartz and alumina wafers served as growth substrates, and argon was used as the carrier gas inside the horizontal CVD tube. Prior to the growth, the furnace was pumped and flushed with Argon several times by bringing the base pressure down to ~ 1 mTorr and refilling it with 99% pure argon gas to lower the residual pressure of oxygen and remove water. The temperature of the furnace was gradually ramped up from ~ 25 to 700 °C (measured at the middle point of the quartz tube) within an hour, and held constantly for ~ 1 h. To facilitate transport of Cd and As vapors, a steady argon flow was maintained within the reactor at the rate of ~ 0.2 SCCM. As schematically shown in Fig. 2-1, the precursor boat was placed in the ~ 600 - 700 °C zone of the furnace while the substrates were placed downstream closer to the exit end of the tube with the temperatures ranging from 150 to 200 °C (measured by a IR-thermometer). Except for the tube end points, the temperature gradient along the tube main axis, $|\nabla T|$ was on average a few degrees per cm. Upon completion, the heater was shut down and the reactor was left to cool down naturally at the average rate of ~ 5 °C min^{-1} in the presence of argon flow.

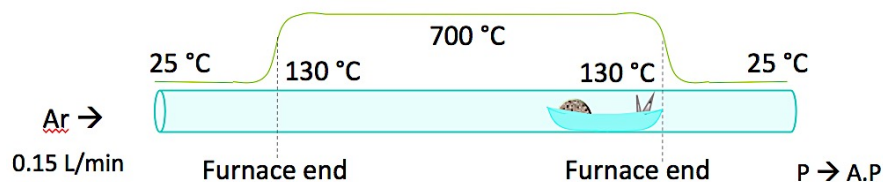


Figure. 2-1. Schematic of the CVD furnace horizontal tube and T-profile.

The alumina substrate appeared shining to the naked eye, and high-density Cd_3As_2 needle/belt-like crystals grown on the inner walls of the quartz tube as well as and on the walls of the alumina boat. Loose, shiny pieces of Cd_3As_2 could be seen inside the boat at the growth zone as well. After the growth, the substrate as well as the reactor sidewalls was subject to visual and optical microscope inspections. The elemental composition, crystal structure and morphology of the grown samples were investigated and the results are provided and discussed in the following section.

2.3 Results and Discussion

2.3.1 Scanning Electron Microscopy of Cd_3As_2 Platelets

As a part of assessing the growth mechanism and influence of various conditions, upon the completion of the growth, the alumina substrate/boat and the quartz tube sidewalls were always subject to visual and optical inspections. The inspection revealed formation of a particulate film at the outlet locations. The film comprised mostly sub-mm diameter amorphous and polycrystalline clusters of Cd_3As_2 . Because at the outlet locations (not exceeding a few cm from the tube end) the temperature would not exceed $\sim 90^\circ\text{C}$, the entering vapors quickly became supersaturated with the condition strongly favoring precipitation of small size particulates over the crystal growth. In contrast, significantly larger, i.e., cm-size crystals were found ~ 15 cm away from the tube end. At threefold higher temperature, the vapors would be less saturated and the rate of crystal nucleation drops with the distance from the reactor ends. Increase in the flow rate or reduction of the base pressure were observed to adversely affect the yield (number) and size of the platelets.

Visual inspections reveal that samples crystallize in two different morphologies: needle- and platelet-like, with the latter featuring microscopically flat, highly reflecting top surfaces. A further examination of the platelets with $\sim 500\times$ optical microscope confirmed a presence of micrometer size crystallites at one of the terminal points, indicating that the platelets originate on a seed. Under the above specified conditions, the platelets had length and width of ~ 1 cm and ~ 2 mm, respectively, with the fastest growth rate approaching $\sim 50 \mu\text{m min}^{-1}$ along the main axis. According to scanning electron microscope (SEM) measurements, Fig. 2-2, performed in a Hitachi S4800 Ultra-High Resolution Field Emission SEM, the thickness of these platelets approaches only $\sim 10 \mu\text{m}$, with an inter-planar growth rate orders of magnitude slower.

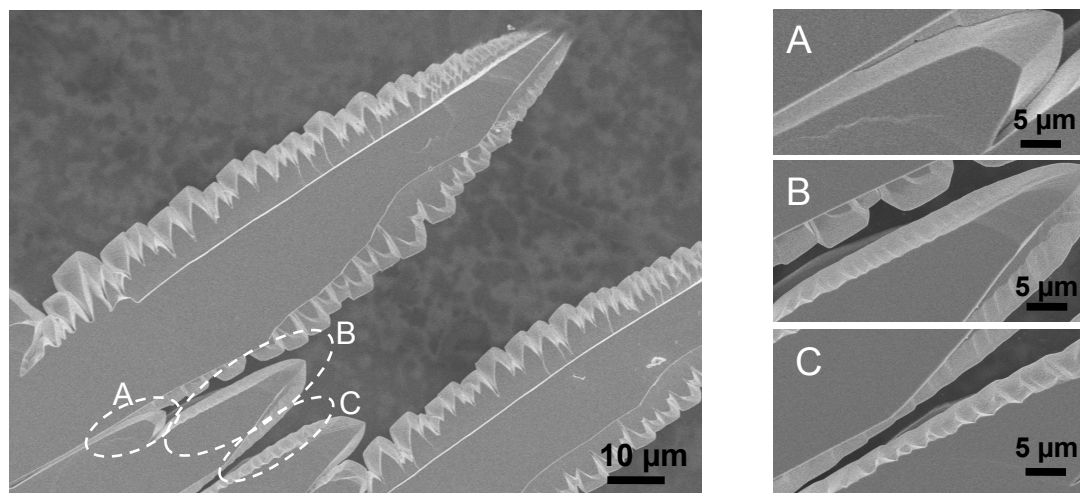


Figure 2-2. SEM images of the platelets grown by low- T CVD with panels A–C showing different stages of secondary platelet growth initiated along the sidewalls.

2.3.2 Energy Dispersive X-ray Spectroscopy Cd_3As_2 Platelets

The site-selected energy dispersive X-ray spectroscopy (EDS) spectra were collected to probe chemical composition along the main platelet axis. Except for the tip, the X-ray intensity ratio showed only a slight deviation from the ideal, i.e. 60:40 Cd to As atomic percentage split/ratio, Fig. 2-3 left, indicating that the platelets are Cd_3As_2 . The Cd composition at the platelet edges

where the growth of additional platelets is observed, Fig. 2-3 spot e, approaches $\sim 55\%$, implying that the formation of secondary structures might be triggered by Cd deficiency; the latter is a result of the target becoming Cd- depleted past the initial growth stage. While the exact mechanism controlling the growth of the secondary platelets is unknown, the micro-loading effect is likely to control the growth at later stages. It is worth noting that Cd content rose to $\sim 69\%$ at the platelet tip, which is likely a result of the precipitation of metallic Cd from Cd-rich vapors within the first hour of the growth.

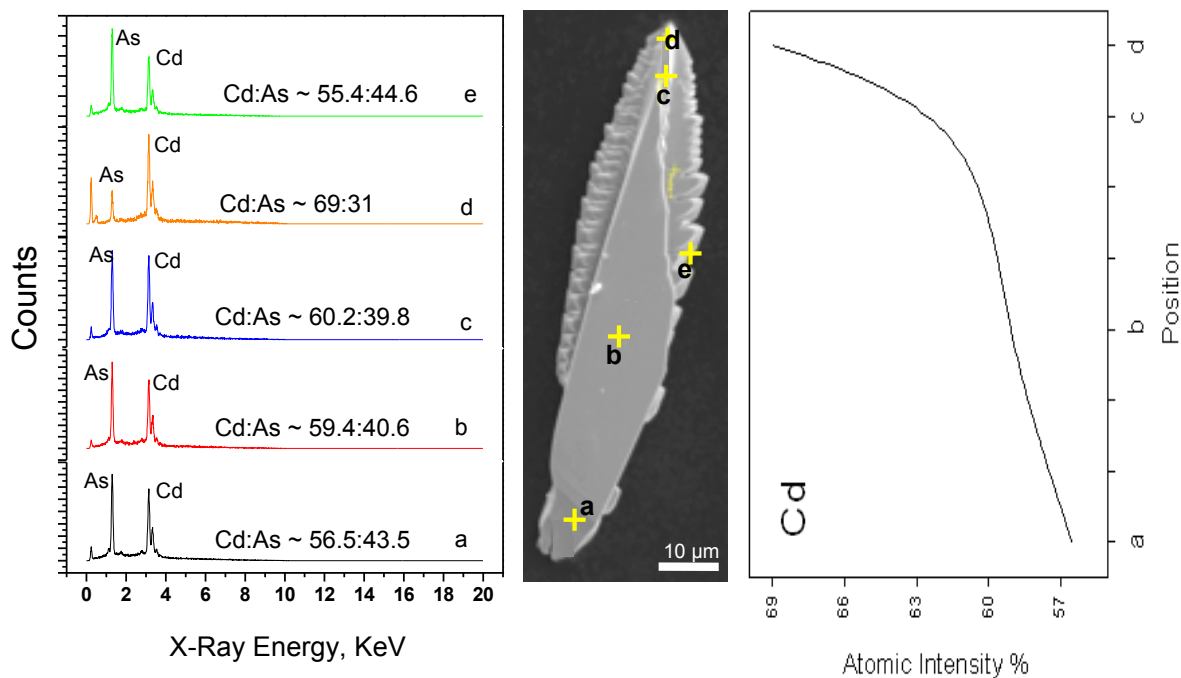


Figure 2-3. Left: site-selected EDS spectra of Cd_3As_2 platelets; middle: low-magnification SEM image of the platelet; right: Cd composition taken along the main axis of the platelet.

Due to overall low T, the entire crystallization process remains kinetically limited, which rules out flow rate and profile as regulating the growth of the platelets. On the other hand, the vapors entering the outlet region cannot cool down abruptly, so the excess Cd present at the very tip of the platelets, similar to the case of nanowires⁴¹ is likely to act as a catalyst, potentially explaining the elongated geometry of the crystals.

2.3.3 Micro-Raman Spectroscopy

To probe the sample quality, Raman spectroscopy was performed on the platelets using a Renishaw Raman spectrometer that operates in conjunction with a 20X optical microscope and edge filter. The sample was excited using 632.8 nm He–Ne laser line. The backscattered light was collected and dispersed by a spectrometer onto a thermoelectrically cooled charge-coupled device (CCD) detector array. While Raman phonon bands are expected to be weak in semimetals, several strong bands were readily registered in the frequency range of $\sim 1500\text{ cm}^{-1}$ with their peaks at 210, 265, 412, 669, and 821 cm^{-1} , Fig. 2-4 pointing to a high crystal quality of the material. Two prominent Raman bands at 210 and 265 cm^{-1} with full-widths at half maximum of 18 and 10 cm^{-1} , respectively mimic 195 and 249 cm^{-1} peaks of bulk Cd_3As_2 and are thus attributed to Raman-allowed phonon modes of bulk Cd_3As_2 . A consistent blue-shift of $\sim 15\text{ cm}^{-1}$ that is evident for both modes points to a residual compressive strain induced as a result of platelet cooling, Fig. 2-5, the inset. The lowest, high intensity mode at 210 cm^{-1} (195 cm^{-1} in target) coincides with 196 cm^{-1} phonon-allowed mode reported by Jandl et al.⁴² and Weszka et al.⁴³, whereas the largest intensity mode at 265 cm^{-1} (249 cm^{-1} in target) was also predicted and reported to exist in $\alpha\text{-Cd}_3\text{As}_2$ by Weszka.⁴³

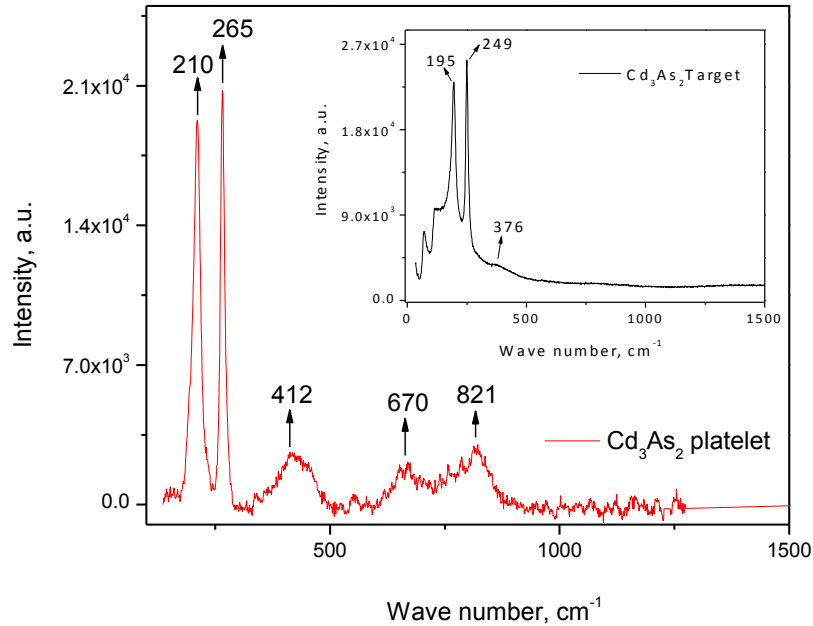


Figure 2-4. Room-temperature Raman spectrum of Cd₃As₂ platelet; the inset shows Raman spectrum of the Cd₃As₂ target.

2.3.4 Transmission Electron Microscopy of Cd₃As₂ Platelets

The bulk crystal structure of Cd₃As₂ ($a = 1.267$ nm and $c = 2.548$ nm) comprises a face-centered cubic lattice for As with six Cd atoms occupying the eight corners of an inner cube (two diagonally opposite corners of a cubic face remain empty). Its space group belongs to a noncentro-symmetric $\bar{C}_{4v}^{12}(I4_1cd)$ structure.^{44,45}

To confirm the formation of single crystals and assess the crystal quality, the platelets were subject to transmission electron microscope (TEM) analysis (Hitachi H9000NAR, 300 keV). Fig.2-5 presents typical bright field (a) and high-resolution (b) TEM images and selected area electron diffraction (SAED) pattern (c) obtained on the platelet in a thin area that includes side growth. The patterns obtained from various locations of a flat platelet were identical and quasi-hexagonal, confirming that samples are single crystals that are terminated with the (112) plane. By performing Fourier Transform of high-resolution transmission electron microscopy

(HRTEM) images, like the one shown in Fig. 2-5(b), with the aid of existing X-ray powder diffraction data, we confirm the average lattice spacing of 0.222 nm for the $\{440\}$ type reflections, and a spacing of 0.225 nm for the $\{408\}$ type reflections, with an average angle of 60° . A square-like pattern is seen as a secondary feature, especially in the areas of the secondary platelet growth. This pattern can be indexed in the Cd_3As_2 tetragonal framework as composed of $\{220\}$ and $\{221\}$ perpendicular planes, in epitaxial orientation relationship to the hexagonal pattern as labeled on Fig. 2-5(c). The crystal planes identified in Figure 4b correspond to $[221]$ ones of the tetragonal lattice of Cd_3As_2 .⁴⁵

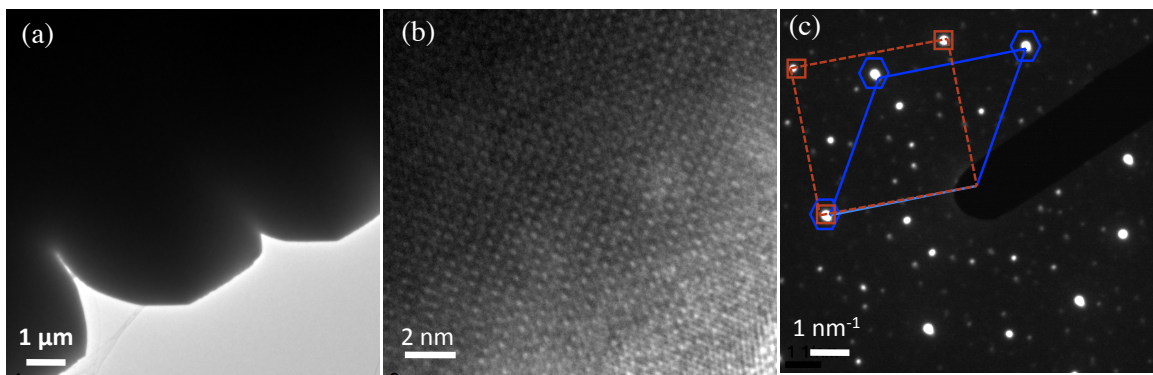


Figure 2-5. a,b) Low- and high-resolution TEM images of the platelet; c) a corresponding SAED pattern.

References

1. Novoselov, K. S. *et al.* Two-dimensional gas of massless Dirac fermions in graphene. *Nature* **438**, 197–200 (2005).
2. Zhang, H. *et al.* Topological insulators in Bi_2Se_3 , Bi_2Te_3 and Sb_2Te_3 with a single Dirac cone on the surface. *Nat. Phys.* **5**, 438–442 (2009).
3. Wang, Z., Weng, H., Wu, Q., Dai, X. & Fang, Z. Three-dimensional Dirac semimetal and quantum transport in Cd_3As_2 . *Phys. Rev. B* **88**, 125427 (2013).
4. Liu, Z. K. *et al.* Discovery of a Three-Dimensional Topological Dirac Semimetal, Na_3Bi . *Science* **343**, 864–867 (2014).
5. Burkov, A. A. & Balents, L. Weyl Semimetal in a Topological Insulator Multilayer. *Phys. Rev. Lett.* **107**, 127205 (2011).
6. Hasan, M. Z. & Kane, C. L. Colloquium. *Rev. Mod. Phys.* **82**, 3045–3067 (2010).
7. He, L. *et al.* Pressure-induced superconductivity in the three-dimensional topological Dirac semimetal Cd_3As_2 . *Npj Quantum Mater.* **1**, 16014 (2016).
8. Cao, J. *et al.* Landau level splitting in Cd_3As_2 under high magnetic fields. *Nat. Commun.* **6**, 7779 (2015).
9. Zhu, Z. & Hoffman, J. E. Condensed-matter physics: Catching relativistic electrons. *Nature* **513**, 319–320 (2014).
10. Neupane, M. *et al.* Observation of a three-dimensional topological Dirac semimetal phase in high-mobility Cd_3As_2 . *Nat. Commun.* **5**, 3786 (2014).
11. Liang, T. *et al.* Ultrahigh mobility and giant magnetoresistance in the Dirac semimetal Cd_3As_2 . *Nat. Mater.* **14**, 280–284 (2015).
12. Wang, Z. *et al.* Dirac semimetal and topological phase transitions in A_3Bi ($\text{A}=\text{Na}, \text{K}, \text{Rb}$). *Phys. Rev. B* **85**, 195320 (2012).
13. Abrikosov, A. A. Quantum magnetoresistance. *Phys. Rev. B* **58**, 2788–2794 (1998).
14. Abrikosov, A. A. Quantum linear magnetoresistance. *EPL Europhys. Lett.* **49**, 789 (2000).
15. Liu, C.-X. *et al.* Oscillatory crossover from two-dimensional to three-dimensional topological insulators. *Phys. Rev. B* **81**, 041307 (2010).
16. Kobayashi, S. & Sato, M. Topological Superconductivity in Dirac Semimetals. *Phys. Rev. Lett.* **115**, 187001 (2015).

17. Xu, S.-Y. *et al.* Observation of Fermi arc surface states in a topological metal. *Science* **347**, 294–298 (2015).
18. Liu, Z. K. *et al.* A stable three-dimensional topological Dirac semimetal Cd₃As₂. *Nat. Mater.* **13**, 677–681 (2014).
19. Borisenko, S. *et al.* Experimental Realization of a Three-Dimensional Dirac Semimetal. *Phys. Rev. Lett.* **113**, 027603 (2014).
20. Jeon, S. *et al.* Landau quantization and quasiparticle interference in the three-dimensional Dirac semimetal Cd₃As₂. *Nat. Mater.* **13**, 851–856 (2014).
21. Aggarwal, L. *et al.* Unconventional superconductivity at mesoscopic point contacts on the 3D Dirac semimetal Cd₃As₂. *Nat. Mater.* **15**, 32–37 (2016).
22. Wang, H. *et al.* Observation of superconductivity induced by a point contact on 3D Dirac semimetal Cd₃As₂ crystals. *Nat. Mater.* **15**, 38–42 (2016).
23. Li, C.-Z. *et al.* Giant negative magnetoresistance induced by the chiral anomaly in individual Cd₃As₂ nanowires. *Nat. Commun.* **6**, 10137 (2015).
24. He, L.-P. & Li, S.-Y. Quantum transport properties of the three-dimensional Dirac semimetal Cd₃As₂ single crystals. *Chin. Phys. B* **25**, 117105 (2016).
25. Zhou, T., Zhang, C., Zhang, H., Xiu, F. & Yang, Z. Enhanced thermoelectric properties of the Dirac semimetal Cd₃As₂. *Inorg. Chem. Front.* **3**, 1637–1643 (2016).
26. Chen, Z.-G. *et al.* Scalable Growth of High Mobility Dirac Semimetal Cd₃As₂ Microbelts. *Nano Lett.* **15**, 5830–5834 (2015).
27. Moll, P. J. W. *et al.* Transport evidence for Fermi-arc-mediated chirality transfer in the Dirac semimetal Cd₃As₂. *Nature* **535**, 266–270 (2016).
28. Bulk crystal growth and electronic characterization of the 3D Dirac semimetal Na₃Bi. *APL Mater.* **3**, 041504 (2015).
29. He, L. P. *et al.* Quantum Transport Evidence for the Three-Dimensional Dirac Semimetal Phase in Cd₃As₂. *Phys. Rev. Lett.* **113**, 246402 (2014).
30. Kloc, K. & Żdanowicz, W. Growth and morphology of Zn₃P₂, Cd₃P₂ and Cd₃As₂ crystals. *J. Cryst. Growth* **66**, 451–458 (1984).
31. Hiscocks, S. E. R. & Elliott, C. T. On the preparation, growth and properties of Cd₃As₂. *J. Mater. Sci.* **4**, 784–788 (1969).
32. Arushanov, E. K. Crystal growth and characterization of II₃V₂ compounds. *Prog. Cryst. Growth Charact.* **3**, 211–255 (1980).

33. Dubowski, J. J. & Williams, D. F. Growth and properties of Cd₃As₂ films prepared by pulsed-laser evaporation. *Can. J. Phys.* **63**, 815–818 (1985).
34. Hrubý, A. & Petrová, J. Preparation of Cd₃As₂ and CdAs₂ crystals by transport reaction in vapour phase. *Czechoslov. J. Phys. B* **21**, 890–895 (1971).
35. Li, C.-Z. *et al.* Synthesis and Photovoltaic Properties of Cd₃As₂ Faceted Nanoplates and Nano-Octahedrons. *Cryst. Growth Des.* **15**, 3264–3270 (2015).
36. *Chemical Vapour Deposition.* (2008).
37. Jensen, K. F. Chemical Vapor Deposition. in *Microelectronics Processing* **221**, 199–263 (American Chemical Society, 1989).
38. Chemical Vapor Deposition. in *The Materials Science of Semiconductors* 573–609 (Springer US, 2008). doi:10.1007/978-0-387-68650-9_12
39. Sudarshan, E. by J.-H. P. and T. S. *Surface Engineering Series Volume 2: Chemical Vapor Deposition.* (ASM International, 2000).
40. Structural properties and growth mechanism of Cd₃As₂ nanowires. *Appl. Phys. Lett.* **106**, 013115 (2015).
41. Jandl, S., Desgreniers, S., Carlone, C. & Aubin, M. J. The Raman Spectrum of Cd₃As₂. *J. Raman Spectrosc.* **15**, 137–138 (1984).
42. Weszka, J., Renucci, M. & Zwick, A. Some aspects of Raman scattering in Cd₃As₂ single crystals. *Phys. Status Solidi B* **133**, 57–64 (1986).
43. Ali, M. N. *et al.* The Crystal and Electronic Structures of Cd₃As₂, the Three-Dimensional Electronic Analogue of Graphene. *Inorg. Chem.* **53**, 4062–4067 (2014).
44. LIN-CHUNG, P. J. Energy-Band Structures of Cd₃As₂ and Zn₃As₂. *Phys. Rev.* **188**, 1272–1280 (1969).

Chapter 3.

Transport Properties and Seebeck Coefficient Study of Cd₃As₂ Platelets

As discussed previously, the ZT expression shows that for good thermoelectric performance both the Seebeck coefficient and electrical conductivity are expected to be high (i.e. large power factor) while the thermal conductivity is expected to be low. The Cd₃As₂ crystal possesses Dirac fermions that disperse linearly in k-space and as a result it becomes a crystalline material with ultrahigh electron mobility, μ , of about $10^4 - 10^6 \text{ cm}^2 \text{ V}^{-1} \text{ s}^{-1}$.^{1,2} Since the power factor, $S^2\sigma$ strongly depends on the electron mobility i.e. $S^2\sigma \approx \mu \left(\frac{m^*}{m_e}\right)^{1.5}$ (where m^* is the energy-band electron effective mass and m_e is the free electron mass),³ Cd₃As₂ shows a great potential for high performance thermoelectric applications.

Several experimental methods such as the angle-resolved photoemission spectroscopy (ARPES)⁴⁻⁷, scanning tunneling microscopy (STM),⁸ the point contact experiments⁹, and the high-pressure resistance measurements^{10,11} have been employed to verify the predicted nontrivial properties of Cd₃As₂. In addition to these sophisticated experimental methods, it is also possible to indirectly measure some properties through simpler methods such as temperature dependent transport and electrical conductance measurements as well as the Hall effect measurements. In the case of thermoelectric studies, usually the first round of tests to investigate the TE properties of a material is based mainly on transport properties as well as ZT evaluation, which is achieved through measuring the thermopower, i.e the Seebeck coefficient of the material. Being the most stable 3D topological Dirac semimetal, Cd₃As₂ has the advantage of being suitable for transport measurements and assessing its potential for application in thermoelectrics.

In this chapter, the transport properties as well as the TE performance of our Cd_3As_2 , a series of temperature dependent transport measurements as well as thermopower measurements were carried out performed on the CVD-grown crystals of Cd_3As_2 . The measurement setup , test conditions and approach are given below; the power factor, , electrical conductivity and the Seebeck coefficient of the platelets are obtained as function of T. The data is modeled using a bipolar heat transport model, the T-dependent $|S|$ data is used to assess the band separation in the inverted band structure of Cd_3As_2 .

3.1 Experimental Procedures

To probe the charge-transport characteristics, the platelets were placed across a ~ 5 mm gap formed by two In electrodes on a Au-coated glass substrate, as illustrated in Fig. 3-1. For temperature dependent (T-dependent) transport measurements, the device was mounted in a heating/cooling stage (Instec HCS302), and the current–voltage (I–V) characteristics were acquired with a Keithley 236 Source–Measure Unit (SMU). The I–V characteristics were collected at the temperature range of ~ 220 - 620 K and bias range of ± 5 mV.

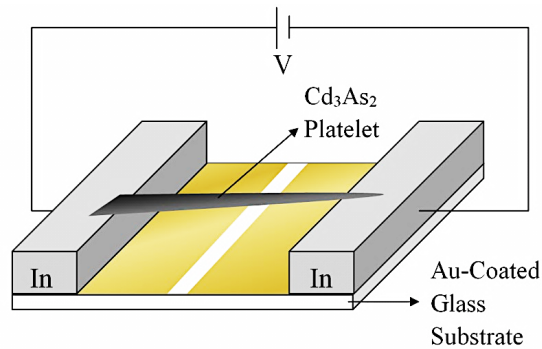


Figure 3-1. Schematic of device configuration for transport measurements. The Cd_3As_2 platelet was placed across a ~ 5 mm gap formed by two In electrodes.

The thermopower (the magnitude of Seebeck coefficient, S) measurements were carried out at the same temperature range by mounting the measurement module in a Janis closed-cycle cryostat featuring an optical access window and operating at a pressure of $\sim 10^{-4}$ Torr. The measurement setup is illustrated in Fig. 3-2. A T-differential of ~ 5 K (as registered by a thermocouple) was induced by illuminating one of the metal terminals with cw-1064 nm solid-state laser, and the I-V data was collected using Keithley 236 Source–Measure Unit (SMU). To limit the noise, these I-V plots were used to extract the thermally induced voltages that appeared as V_{oc} .

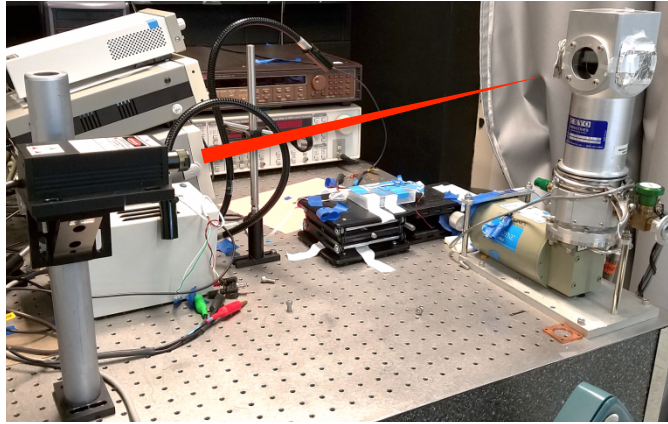


Figure 3-2. The measurement setup used for thermopower (S) measurement of Cd₃As₂ which consists of a cw-IR laser source, Janis closed-cycle cryostat system with optical access window operating under various vacuum conditions. The measurements were carried out at temperature range of ~ 220 - 620 K in vacuum. A T-differential of ~ 5 K was induced by illuminating one side of the sample with cw-1064 nm solid-state laser and the I-V data was collected at each temperature.

3.2 Results and Discussion

3.2.1 T-dependent current-voltage measurements

The I-V measurements were performed on two platelets, referred as to Sample A and sample B, from two different sample batches grown separately. The resultant I-V plots at various

temperatures had an Ohmic trend for both platelets. Fig. 3-3 (a) shows the I-Vs obtained from sample A. The T-dependent electrical conductance was calculated by differentiating the I-V plots, Fig.3-3 (b). The conductance was found to decay monotonically with T in both platelets, which is typical of both semimetals and degenerately doped semiconductors.

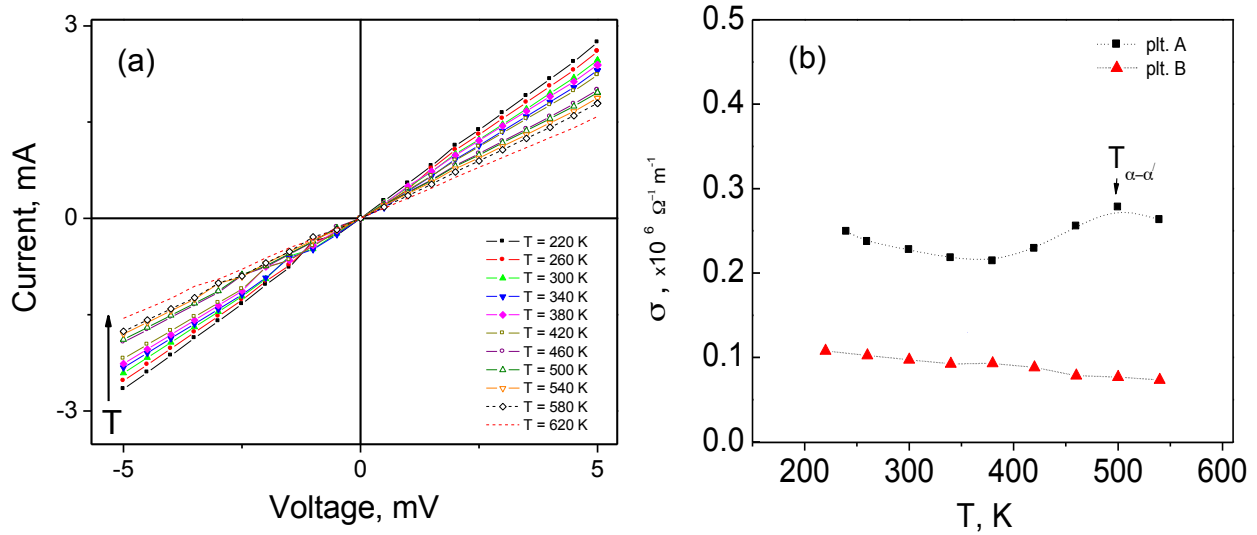


Figure 3-3. a) Typical I–V characteristics of Cd_3As_2 platelet (sample A) obtained in a temperature range of ~ 220 – 620K ; b) electrical conductance vs. T for samples A and B. The monotonic decay of the conductance with T in both platelets is typical of both semimetals and degenerately doped semiconductors.

As it is evident in Fig. 3-3 (b), a shoulder peak appears on the right shoulder of the conductance plot for platelet A around $\sim 500\text{K}$. This peak position coincides with the temperature of $\alpha \rightarrow \alpha'$ phase transition in Cd_3As_2 which is associated with an increase in the electron mobility.

3.2.2 Temperature dependent Thermo-power Measurements

Recall that the Seebeck coefficient —also known as thermopower, thermoelectric power, and thermoelectric sensitivity— of a material is a measure of the magnitude of an induced thermoelectric voltage ΔV in response to a temperature difference ΔT across that material, and it is defined as

$$S = -\frac{\Delta V}{\Delta T} \quad (3-1)$$

Therefore, in order to calculate the Seebeck coefficient, the thermoelectric voltage developed per unit temperature difference in the sample must be measured. As mentioned above, this was done by extracting the open circuit voltage V_{oc} from the I-V data collected from the sample while inducing a T-differential of $\sim 5K$ across the sample, as shown in Fig. 3-4.

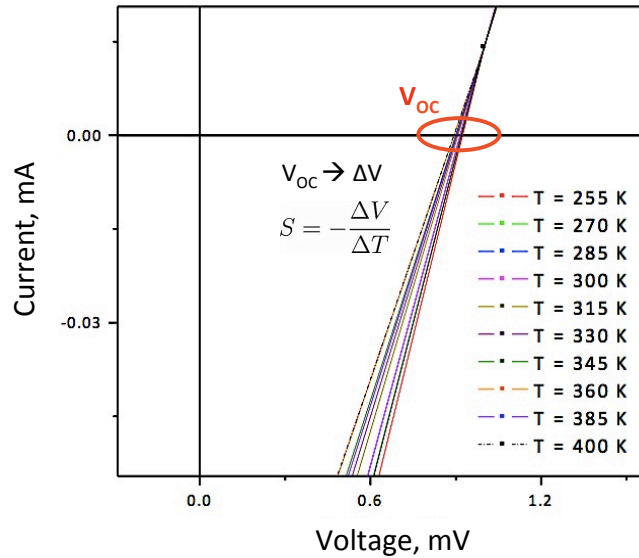


Figure 3-4. The Seebeck coefficient was calculated by extracting the thermoelectric voltage from the I-V data collected from the sample while inducing a T-differential of $\sim 5K$ across the sample using cw-1064 nm solid-state laser.

The generated thermoelectric voltage across the Cd_3As_2 platelet was positive resulting in a negative Seebeck coefficient S . As $S < 0$, the samples were confirmed to be n-type doped in line with the results of prior studies.^{12,13}

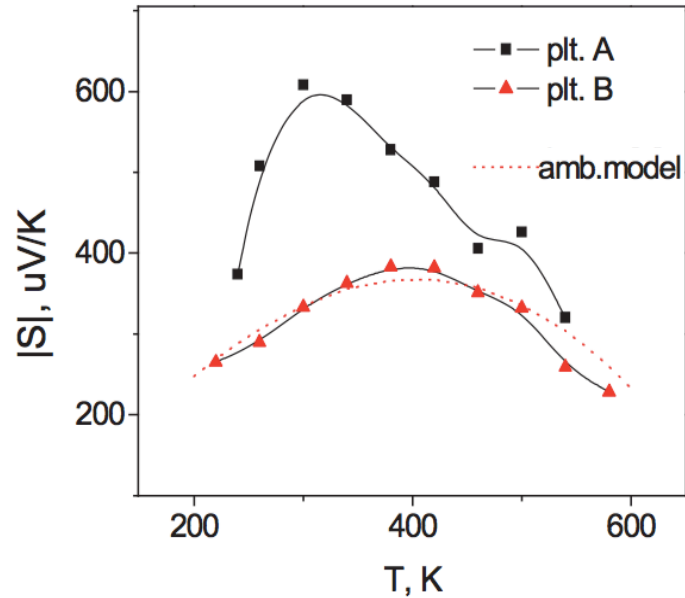


Figure 3-5. Magnitude of Seebeck coefficient vs. T . The $S < 0$ indicates that the samples were n-type doped in line with the reported results in previous studies. The dashed line is the ambipolar model fit to the experimental data of platelet B.

Figure 3-5 shows the T-dependent thermo-power for platelets A and B. As seen, S rises linearly with T until reaching a peak at T_{\max} after which it undergoes a gradual decrease. This behavior is typical of degenerate thermoelectric semiconductors.^{14,15} In such materials, the magnitude of the Seebeck coefficient, $|S|$ initially rises linearly with temperature followed by a decrease in thermopower explaining the peak-shape of $S(T)$ as seen in Fig. 3-5. In doped-semiconductors, due to small activation energy, extrinsic charge carriers can be readily excited and dominate the thermo-electric properties, and the magnitude of the Seebeck coefficient, $|S|$, rises with temperature as the Fermi levels shifts up or down from its intrinsic position (Dirac point in Dirac semimetals). When the temperature is increased further, the rate of interband electron-hole pair generation increases and $|S|$ starts to fall due to the opposing contribution of electrons and holes to thermopower.¹⁵ The peak of thermopower remains one of the key signatures of bipolar conduction mechanism facilitated by thermal interband excitation of free electrons and holes in

semiconductor systems. The strength of bipolar conduction is controlled by rate of interband e-h generation, and as a result, $|S|$ vs T data can be used to estimate the energy gap E_g of semiconductor materials.¹⁴⁻¹⁷ as discussed below.

Before we proceed with the calculation of the effective band separation, we should note the kink on the right shoulder of S , especially evident for platelet A, similar to what was observed in conductance plots of Fig. 3-3(b). As we shall see in the next subsection, the thermopower of a degenerate n-type semiconductor generally scales with the free electron density as $|S| \sim n^{-2/3}$. This requires us to attribute the shoulder peak in S at $T \sim 500K$ to an increase in the electron mobility as a result of the first $\alpha \rightarrow \alpha'$ phase transition in Cd_3As_2 . It should be also noted that since both $S_A > S_B$, Fig. 3-5, and $\sigma_A > \sigma_B$, Fig. 3-3(b), the electron mobility is estimated to be larger in platelet A.

3.2.3 Calculation of the band inversion in Cd_3As_2 using ambipolar heat transport model

As mentioned in previous chapters, Cd_3As_2 has drawn much attention recently because of its inverted band structure. The crystal structure of Cd_3As_2 is related to tetragonally-distorted anti-fluorite structure with 1/4 Cd site vacancy. Similar to most of the semiconductors with anti-fluorite or zinc-blende structures, the low energy electronic properties of Cd_3As_2 are mostly determined by the Cd-5s states (conduction bands) and the As-4p states (valence bands). The band structure of Cd_3As_2 has two distinct features: 1. There is a band-inversion around Γ point with the s-state lower than the p-states which is an important sign of non-trivial topology; and 2. It is semi-metallic with band crossing along the Γ -Z direction protected by C_4 rotational symmetry around k_z axis.¹⁸

Plenkiewicz et al.¹⁹ have implemented a perturbation method to and the results point to vacancy ordering and BZ folding as a origin of band-inversion in Cd₃As₂. Using first-principles calculations, Wang et al.¹⁸ showed that the existence of one Cd vacancy in cubic anti-fluorite structure is to give rise to an inverted band ordering at Γ -point. While theoretical^{19,20} and optical^{21,22} methods have been used to calculate the band inversion in Cd₃As₂, as a part of the |S| vs. T fitting we also attempt to assess the effective band separation in CVD-grown Cd₃As₂.

As mentioned earlier, the origin of the peak in |S| is the temperature-activated ambipolar heat transport. The contribution to the overall Seebeck coefficient (S) by both the positive and negative charge carriers can be described by the conductivity weighted average:

$$S = \frac{|\mu_p p S_p - \mu_n n S_n|}{\mu_n n + \mu_p p} \quad (3-2)$$

where μ_p and μ_n are the carriers' mobility, and p and n are the concentration of the two carriers.

The electrical conductivity of carriers is also given by $\sigma_p = \mu_p p$ and $\sigma_n = \mu_n n$.

According to Eq. (3-2), the density of the minority free carriers rises with T (thermally-activated electronic transitions), which in turn lowers the net thermopower. The onset and strength of minority carrier contribution to the thermopower depend on the semiconductor band-gap, E_g as well as the initial majority carrier (dopant) concentration. The peak value of Seebeck coefficient S_{max} and the temperature at which it is attained, T_{max} can be used to estimate the band gap using the Goldsmid-Sharp relation¹⁵

$$E_g = 2eS_{max}T_{max} \quad (3-3)$$

where $e = 1.6 \times 10^{-19}$ C is the electron charge.

The Goldsmid-Sharp gap was established based on two main assumptions. First, it was assumed that $E_g > 10 k_B T$ (the parameter $\epsilon_g = E_g / k_B T$ is called the dimensionless bandgap, which governs the strength of bipolar conduction), and second, the majority-to-minority weighted mobility ratio was assumed to be equal¹⁴. However, while the Goldsmid-Sharp relation can serve as a quick estimate of the effective band gap present in the vicinity of E_F , it can significantly deviate from the actual optical band gap value in heavily doped materials with a large majority to-minority weighted mobility ratio²³ or in narrow-gap semiconductors where usually $E_g < 10 k_B T$.

As a result, since Cd_3As_2 can be considered as a degenerate, narrow-gap (inverted band) semiconductor, the Goldsmid-Sharp relation could not be employed to calculate the band separation in our samples. Hence, to accurately model the temperature response in this study, the data was fitted directly by using Eq. (3-2) as follows.

For degenerate semiconductors at the low temperature limit of $T \lesssim E_g / k_B T$, the temperature dependence of the Seebeck coefficient is given by²⁴

$$S \cong \frac{8\pi^{8/3} k_B^2 m^*}{3^{5/3} e h^2 n^{2/3}} T \quad (3-4)$$

where m^* is the carrier effective mass, n is the carrier concentration, k_B is the Boltzmann constant, e is the electron charge, and h is the Planck's constant.

From Eq. (3-4) we see that the Seebeck coefficient is inversely proportional to carrier concentration, i.e. $S \sim n^{-2/3}$; therefore, since the minority carriers are fewer in number, they will have higher thermo-power contributions. However, at low temperatures, the population of minority carriers is small, so they will not contribute much to the overall S . At higher temperatures, though, a broadening Fermi distribution leads to an exponential increase in minority carrier conductivity resulting in a reduction in the thermopower, giving rise to the

formation of a peak in the $|S|$ curve.¹⁵ Eq. (3-4) provides a means to independently assess the majority carrier density by fitting the low- T portion of S versus T curve (linear regime) assuming that m^* on n dependence is established beforehand. The effective mass of Cd_3As_2 was evaluated within the concentration range of $\sim 10^{17}$ – 10^{18} cm^{-3} earlier, and m^*/m_0 was found to vary within ~ 0.02 – 0.03 .²⁵

Applying an order of magnitude estimate for effective mass of $m^*/m_0 \approx 10^{-2}$ the fitting results yields $n \approx 10^{17}$ cm^{-3} and the electron mobility of $\sim 10^5$ $\text{cm}^2\text{V}^{-1}\text{s}^{-1}$ for platelet B. At higher T , the Fermi level shifts down and the intrinsic behavior is recovered (ambipolar regime). The carrier density calculations accomplished within the framework of np-equation,²⁶ yield the effective band separation of ~ 90 meV, and S-T data matches reasonably well the experimental results as shown in Fig. 3-5. The attempts to fit the data for platelet A were not as successful, mostly because of the stronger contribution of the phase transition (right shoulder peak) to S at high T -range. Despite this, still the correct position of the ambipolar peak for sample A could only be attained for the effective band separation of ~ 370 meV. The obtained values generally agree with the results of prior optical absorption studies that point to the existence of multiple bandgaps of ~ 0.6 and ~ 0.13 eV in Cd_3As_2 .^{21,27} While the free carrier density is to rise as a result of thermally activated interband transitions, the carrier mobility and in turn electrical conductivity generally become suppressed as temperature rises due to an increase in the rate of the electron–phonon scattering, in line with the trends seen in Fig. 3-3(b).

To further confirm the unexpected TE properties of the Cd_3As_2 platelets, in the next chapter, we will measure the thermal conductivity of our samples and the ZT value will be assessed based on the findings for thermal conductivity.

References

1. Neupane, M. *et al.* Observation of a three-dimensional topological Dirac semimetal phase in high-mobility Cd₃As₂. *Nat. Commun.* **5**, 3786 (2014).
2. Liang, T. *et al.* Ultrahigh mobility and giant magnetoresistance in the Dirac semimetal Cd₃As₂. *Nat. Mater.* **14**, 280–284 (2015).
3. Pei, Y. *et al.* Convergence of electronic bands for high performance bulk thermoelectrics. *Nature* **473**, 66–69 (2011).
4. Liu, Z. K. *et al.* Discovery of a Three-Dimensional Topological Dirac Semimetal, Na₃Bi. *Science* **343**, 864–867 (2014).
5. Xu, S.-Y. *et al.* Observation of a bulk 3D Dirac multiplet, Lifshitz transition, and nested spin states in Na₃Bi. *ArXiv13127624 Cond-Mat* (2013).
6. Liu, Z. K. *et al.* A stable three-dimensional topological Dirac semimetal Cd₃As₂. *Nat. Mater.* **13**, 677–681 (2014).
7. Borisenko, S. *et al.* Experimental Realization of a Three-Dimensional Dirac Semimetal. *Phys. Rev. Lett.* **113**, 027603 (2014).
8. Jeon, S. *et al.* Landau quantization and quasiparticle interference in the three-dimensional Dirac semimetal Cd₃As₂. *Nat. Mater.* **13**, 851–856 (2014).
9. Aggarwal, L. *et al.* Unconventional superconductivity at mesoscopic point contacts on the 3D Dirac semimetal Cd₃As₂. *Nat. Mater.* **15**, 32–37 (2016).
10. He, L. *et al.* Pressure-induced superconductivity in the three-dimensional topological Dirac semimetal Cd₃As₂. *Npj Quantum Mater.* **1**, 16014 (2016).
11. Li, C.-Z. *et al.* Giant negative magnetoresistance induced by the chiral anomaly in individual Cd₃As₂ nanowires. *Nat. Commun.* **6**, 10137 (2015).
12. Armitage, D. & Goldsmid, H. J. The thermal conductivity of cadmium arsenide. *J. Phys. C Solid State Phys.* **2**, 2138 (1969).
13. Jandl, S., Desgreniers, S., Carlone, C. & Aubin, M. J. The Raman Spectrum of Cd₃As₂. *J. Raman Spectrosc.* **15**, 137–138 (1984).
14. Band gap estimation from temperature dependent Seebeck measurement—Deviations from the $2e|S|_{\max}T_{\max}$ relation. *Appl. Phys. Lett.* **106**, 022112 (2015).
15. Goldsmid, H. J. & Sharp, J. W. Estimation of the thermal band gap of a semiconductor from seebeck measurements. *J. Electron. Mater.* **28**, 869–872 (1999).
16. Shahi, P. *et al.* Bipolar Conduction is the Origin of the Electronic Transition in Pentatellurides: Metallic vs. Semiconducting Behavior. *ArXiv161106370 Cond-Mat* (2016).
17. Kaiser, A. B. Diffusion origin of thermopower peaks in spin-fluctuation alloys. *J. Phys. F Met. Phys.* **10**, 1419 (1980).
18. Wang, Z., Weng, H., Wu, Q., Dai, X. & Fang, Z. Three-dimensional Dirac semimetal and quantum transport in Cd₃As₂. *Phys. Rev. B* **88**, 125427 (2013).

19. Pleniewicz, B., Wallace, P. R. & Pleniewicz, P. The role of vacancies in the band structure of Cd₃As₂. *Solid State Commun.* **50**, 681–684 (1984).
20. LIN-CHUNG, P. J. Energy-Band Structures of Cd₃As₂ and Zn₃As₂. *Phys. Rev.* **188**, 1272–1280 (1969).
21. Żdanowicz, L. Some Optical Properties of Thin Evaporated Cd₃As₂Films. *Phys. Status Solidi B* **20**, 473–480 (1967).
22. Iwami, M., Yoshida, M. & Kawabe, K. Infrared Optical Absorption in Cd₃As₂. *Jpn. J. Appl. Phys.* **12**, 1276 (1973).
23. Schmitt, J., Gibbs, Z. M., Snyder, G. J. & Felser, C. Resolving the true band gap of ZrNiSn half-Heusler thermoelectric materials. *Mater. Horiz.* **2**, 68–75 (2014).
24. Zhao, W. *et al.* Multi-localization transport behaviour in bulk thermoelectric materials. *Nat. Commun.* **6**, 6197 (2015).
25. Iii/17e-17f-41c, C. A. and editors of the volumes. Cadmium arsenide (Cd₃As₂) effective masses. in *Non-Tetrahedrally Bonded Elements and Binary Compounds I* (eds. Madelung, O., Rössler, U. & Schulz, M.) 1–4 (Springer Berlin Heidelberg, 1998). doi:10.1007/10681727_253
26. Wiley: Physics of Semiconductor Devices, 2nd Edition - Simon M. Sze. Available at: <http://www.wiley.com/WileyCDA/WileyTitle/productCd-0471673242.html>. (Accessed: 24th March 2017)
27. Aubin, M. J., Caron, L. G. & Jay-Gerin, J. P. Band structure of cadmium arsenide at room temperature. *Phys. Rev. B* **15**, 3872–3878 (1977).

Chapter 4.

Thermal conductivity measurement of Cd₃As₂ Platelets

In previous chapters, we demonstrated that the crystalline Cd₃As₂ platelets grown through a low-T chemical vapor deposition (CVD) method exhibit Ohmic-like transport behavior with a high electrical conductance $\sigma \approx 10^5 \Omega^{-1}m^{-1}$ and a large thermo-power $S \approx 600 \mu VK^{-1}$ at room temperature. These two together will result in a large power factor $S^2\sigma$ indicating that Cd₃As₂ holds a great promise for high efficiency thermoelectric applications. In order to further confirm the significance of TE properties of crystalline Cd₃As₂, we would need to calculate its figure of merit ZT given by:

$$ZT = \frac{S^2\sigma}{\kappa} T \quad (4-1)$$

Therefore, in addition to the thermo-power S and the electrical resistance σ , calculating ZT also requires measuring the thermal conductivity of Cd₃As₂ platelets.

There are various techniques for measuring the thermal conductivity of both bulk¹, and thin film solid-state materials². Some of the most common measurement methods for bulk materials include: transient hot-wire method,³⁻⁵ steady-state resistivity method,⁶⁻⁸ laser flash diffusivity method,⁹⁻¹¹ transient plane source method.¹²⁻¹⁴

Similarly, for thin film and planar materials there are various electro-thermal and optical measurement techniques. The mostly used methods include, modulated methods such the 3ω technique,^{15,16} thermo-reflectance-based techniques in both time-domain (TDTR), and frequency-domain (FDTR),¹⁷⁻¹⁹ and methods based on Raman spectroscopy.^{20,21}

For electro-thermal methods, both DC and AC heating can be used. However, using the AC method has several advantages over the DC. A major advantage of AC heating is that the frequency can be chosen to localize the fluctuating temperature field within the film and substrate, whereas in the case of steady DC heating, all of the heat flows through the substrate and into the environment. Other advantages of AC method include less sensitivity to radiation and convection losses, insensitivity to DC voltage artifacts from thermoelectric effects and low-frequency drifts, and reducing the substrate contribution to the measurements if the sample is mounted on a substrate.²²

In general, selecting a specific measurement technique to characterize thermal properties of materials depends on the sample type, size, and configuration, the fundamentals and procedure of the testing technique and its limitations for each particular sample, and also the potential error sources in each technique, such as the convection and radiation heat losses that might affect the final results.²³

Among many experimental methods developed over the past centuries to measure the fundamental thermal properties of materials, the 3ω method has proven to be valuable for probing thermal properties of various crystals. The popularity of the 3ω method mostly stems from its better signal-to-noise ratio enabled by using a narrow-band detection technique, as well as the one's ability to obtain both thermal conductivity k and specific heat c of the sample. In this method, either the specimen (should be sufficiently electrically conductive and possess T-dependent resistivity) serves as both heater and the temperature sensor, or alternatively a metal strip is deposited on the surface of the specimen to serve as the heater and the sensor if the specimen has a very low or zero electrical conductivity.

In the basic 3ω method, the line heater (the specimen itself or the metal strip) is driven by an AC

electric current of the form $I_0 \sin \omega t$, causing a temperature fluctuation 2ω related to the thermal properties of the heater and/or its surrounding environment, and subsequently a resistance fluctuation at 2ω . The AC current at 1ω and the perturbation of the heater resistance at 2ω lead to the generation of a voltage signal at 3ω .

The 3ω method requires refined sample preparation and in most cases, some expertise in thin film patterning and microlithography, and it also assumes that the circuit is driven by an ideal current source. In addition, in order to increase the signal-to-noise ratio of the small 3^{rd} harmonic signal, the much larger Ohmic signal at 1ω needs to be cancelled. This is usually achieved by either nulling a bridge,^{24,25} or subtraction with a multiplying digital-to-analog converter,²⁶ or by using a digital lock-in amplifier with the capability of detecting higher harmonic signals. These requirements limit the use of the 3ω method for thermal properties measurements of some sample types and configurations although it is considered one of the finest methods available.

In 2005, Dames and Chen²⁷ presented a more general framework to measure thermal properties, applicable to any thermal system with a line heater/sensor. It was identified that the voltage signals at 1ω and 2ω frequencies contained the same information about the thermal properties as the 3ω signal did. They also derived and verified a correction factor that permitted the use of a voltage source instead of a current source, as it is a more common and more convenient option for performing the measurements.

Given the difficulty of implementing the 3ω method on the Cd_3As_2 platelets, we instead employed the method suggested by Dames and Chen (2005), which will be referred as the Dames-Chen method in the rest of this chapter, and used the 1ω signal to measure the thermal conductivity of Cd_3As_2 platelets. This allowed us to eliminate additional steps in the sample

preparation as well as the need for higher-harmonic detection. The theory and details of this technique are provided in the following section.

4.1 1ω Method for Measurement of Thermal Conductivity

In the Dames-Chen method for measurements of thermal properties, the various traditional 3ω methods as well as the dc-heating/ac-detection experiments are united under a more general framework of thermal and electrical transfer functions. As mentioned above, this framework can be applied to any thermal system with a line heater/temperature sensor, and in addition to the 3ω signal, it also enables the use of lower harmonic signals, i.e. 1ω and 2ω , to obtain the information related to the thermal properties of the specimen. Using the lower harmonic signals, in particular the same frequency response (1ω), can facilitate the experiment as no harmonic detection will be required, and the noise cancellation can be handled through a simple low pass filter.

4.1.1 General Transfer Function Framework

To achieve the general transfer function of an electro-thermal system, first the thermal transfer function and the electrical transfer function need to be derived separately. We will use the same notation as what Dames and Chen used in their paper²⁷ to stay consistent.

4.1.1.1 Thermal Transfer Function

A system with a single line heater that is also used as the temperature sensor by detecting the changes in the resistance, can be generally described by a linear thermal transfer function Z that relates the average temperature rise of the heater θ_{ave} to the heat input Q . In the frequency domain we can write:

$$\theta_{\omega} = Q_{\omega}Z \quad (4-2)$$

where the ω subscript denotes Fourier-transformed quantities. In the time domain, this will become:

$$\theta_{ave}(t) = Q(t) \otimes Z_t \quad (4-3)$$

where \otimes denotes convolution and Z_t is the inverse Fourier transform of Z . For example, a sinusoidal heating at frequency ω_H

$$Q(t) = Q_0 \sin(\omega_H t) \quad (4-4)$$

leads to a temperature response in the time domain

$$\theta_{ave}(t) = Q_0 \text{Re}[Z(\omega_H)] \sin(\omega_H t) + Q_0 \text{Im}[Z(\omega_H)] \cos(\omega_H t) \quad (4-5)$$

The thermal transfer function may be complex and frequency dependent. It contains information about the thermal properties of the system, such as thermal conductivity and/or specific heat of the heater and/or its surroundings.

4.1.1.2 Electrical Transfer Function

By measuring the electrical current I and voltage V across the heater, we can determine the thermal properties of the system. First the thermal transfer function must be related to an electrical transfer function.

In general, the electrical resistance of the heater is given by

$$R_e(t) = R_{e0}[1 + \alpha\theta_{ave}(t)] \quad (4-6)$$

where R is the electrical resistance in the limit of zero current and θ_{ave} is averaged over the length of the heater. The temperature fluctuations within the heater must be small enough to be able to treat it as a constant. It is easily shown that Eq. (4-6) holds even if the temperature profile $\theta(x)$ varies along the length of the heater, as long as the cross section is uniform. Since $\alpha\theta_{ave} \ll 1$, Q can be approximated as

$$Q(t) = I^2(t)R_{e0} \quad (4-7)$$

From Eqs. (4-6) and (4-7), for the voltage drop across the heater we get

$$V(t) = I(t)R_{e0}[1 + \alpha R_{e0}Z_t \otimes I^2(t)] \quad (4-8)$$

Finally, by applying the Fourier transform to Eq. (4-8), the voltage drop in the frequency domain for any current is given by

$$V_\omega = \left(\frac{R_{e0}}{2\pi}\right) I_\omega \otimes \left[2\pi\delta(\omega) + \alpha \left(\frac{R_{e0}}{2\pi}\right) (I_\omega \otimes I_\omega)Z\right] \quad (4-9)$$

where $\delta(\omega)$ is the Dirac delta function in the frequency domain.

The superposition method cannot be used here since Eq. (4-9) is nonlinear in I . Therefore, we proceed with a particular case where a sinusoidal current at frequency ω_1 with a dc offset I_{dc} is used for heating the line heater/sensor:

$$I(t) = I_{dc} + I_1 \sin(\omega_1 t) \quad (4-10)$$

If we define $\eta = \frac{I_{dc}}{I_1}$, then Eq. (4-10) in the frequency will becomes:

$$I_\omega = I_1\{\eta 2\pi\delta(\omega) + j\pi[\delta(\omega + \omega_1) - \delta(\omega - \omega_1)]\} \quad (4-11)$$

where $j = \sqrt{-1}$.

By substituting the I_ω in Eq. (4-9) by Eq. (4-11), we will get:

$$V(t) = V_{dc} + V_{1\omega}(t) + V_{2\omega}(t) + V_{3\omega}(t) \quad (4-12)$$

which indicates that the voltage response occurs at dc and three harmonics.

Eq. (4-12) can be also expressed as:

$$V(t) = \alpha R_{e0}^2 I_1^3 \sum_{n=0}^3 [X_n(\omega_1, \eta) \sin(n\omega_1 t) + Y_n(\omega_1, \eta) \cos(n\omega_1 t)] \quad (4-13)$$

Here the summation is done over the harmonics n , and X_n and Y_n are the in-phase and out-of-phase components of the electrical transfer function, respectively. In terms of rms quantities, which is what usually the lock-in amplifier measures, Eq. (4-13) becomes:

$$\frac{V_{n\omega, rms}}{2\alpha R_{e0}^2 I_{1, rms}^3} = X_n(\omega_1, \eta) + jY_n(\omega_1, \eta) \quad (4-14)$$

This equation is at the very heart of the Dames-Chen method, and it could be applied to any system with a line heater/sensor. It shows that, not only the 3rd harmonic, but other harmonics contain key information on the thermal transfer function.

Since in the present work the 1ω signal was used to obtain the thermal conductivity of Cd_3As_2 platelets, from now on we only focus our attention to the first harmonic. Detailed discussions

pertaining to using other harmonics can be found elsewhere [27]. The resulting in-phase X_n and out-of-phase Y_n components of the electrical transfer function for the 1st electrical harmonic are given as follows:

$$X_1 = \frac{1}{2\alpha R_{e0}^2 I_{1,rms}^3} + \left[\eta^2 + \frac{1}{2} \right] Z(0) + 2\eta^2 \text{Re}[Z(\omega_1)] + \frac{1}{4} \text{Re}[Z(2\omega_1)] \quad (4-15a)$$

$$Y_1 = \frac{1}{4} \text{Im}[Z(2\omega_1)] + 2\eta^2 \text{Im}[Z(\omega_1)] \quad (4-15b)$$

The in-phase 1ω voltage is more important because it also contains information on the dc thermal response in the high- frequency limit. Because of the thermal capacitance effects, most thermal transfer functions diminish at high frequencies. Thus $X_2, X_3, Y_1, Y_2,$ and Y_3 are die out at high frequencies. But X_1 retains a term multiplied by $Z(0)$ which allows the dc thermal response to be measured at high frequencies, as there is always a dc component in the I^2R heating, even at high frequencies. For example, with $I_{dc} = 0$ ($\eta = 0$), the high-frequency limit of X_1 has an Ohmic voltage plus $Z(0)/2$, while in the low-frequency limit the contribution is $3Z(0)/4$. The opposite limit is $I_{dc} \gg I_1$. In this case the high-frequency limit of X_1 is dominated by the contribution of $\eta^2 Z(0)$, while the dominant contribution at low frequency is $3\eta^2 Z(0)$. This means that in a general result, there is a factor of three difference between low- and high-frequency resistances.

Equations (4-15a) and (4-15b) are general solutions that apply to any specimen configuration, including a suspended-wire (SW) configuration, in which the specimen itself acts as the heater/sensor (for conductive specimen), or a line heater on a substrate (LHOS) setup featuring a line heater/sensor strip which can be deposited on the substrate (for low- or non-conductive

specimen). Each case requires that the associated theoretical thermal and electrical transfer functions are derived first.

Given that Cd_3As_2 platelet is highly conductive (transport measurement results), it can act as both the line heater and the temperature sensor in a 4-probe suspended-wire (SW) setup as illustrated in Fig. 4-1 (a), which was built and used to measure the thermal conductivity in this study.

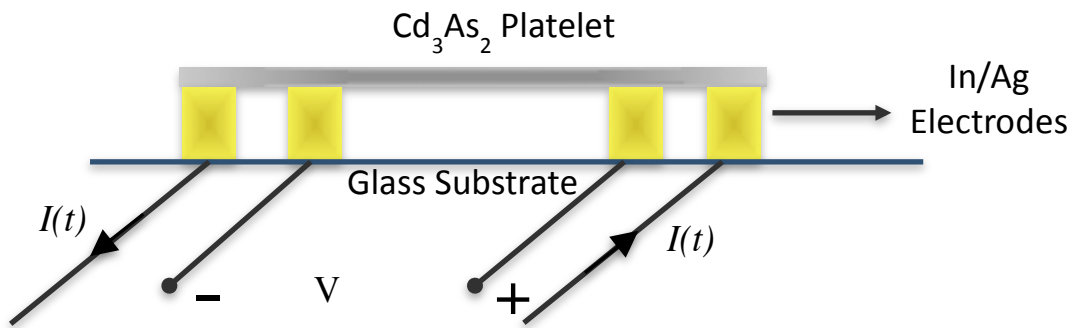


Figure 4-1. Illustration of the four-probe suspended wire (SW) configuration for measuring the thermal conductivity of a Cd_3As_2 platelet. The platelet is heat sunk to the glass substrate through the four electric contacts, but the part in between the two voltage contacts needs to be suspended, to allow the temperature variation.

To proceed, we first derive the thermal and electrical transfer functions for the SW configuration.

Further information on the LHOS setup can be found in work published by Dames and Chen (2005).²⁷

4.1.1.3 Theoretical Transfer Function for the Suspended-Wire Setup

The thermal transfer function for an isolated SW with thermally clamped ends was obtained by Lu *et al.* as a series solution.²⁸ Using a closed-form solution for the spatial temperature profile [27]. The resulting thermal transfer function for a wire of length $2l$ and a cross-sectional area S is given:

$$Z_{SW} = \frac{(\sinh \beta - \sin \beta) + j[\sinh \beta + \sin \beta - \beta (\cosh \beta + \cos \beta)]}{\beta C \omega_H (\cos \beta + \cosh \beta)} \quad (4-16)$$

where C is the thermal capacitance of the wire, β is given by

$$\beta = \sqrt{\frac{\omega_H \tau}{2}} \quad (4-17)$$

and the characteristic diffusion time is

$$\tau = \frac{4l^2}{\kappa} \quad (4-18)$$

where κ denotes the thermal diffusivity.

The shape of this transfer function is reminiscent of a first-order RC system, so it would be more convenient to work with an approximate transfer function $Z_{S,approx}$ instead of the actual, highly complicated transfer function of Eq. (4-16).

The transfer function can be simply written as

$$Z_{SW,approx}(\omega_H) = \frac{R_{th}}{12} \left[\frac{1 - j \omega_H \tau / 10}{1 + (\omega_H \tau / 10)^2} \right] \quad (4-19)$$

where the thermal resistance R_{th} is:

$$R_{th} = \frac{2l}{kS} \quad (4-20)$$

With this approximate transfer function, the resulting in-phase X_n and out-of-phase Y_n components for the 1st electrical harmonic are to become:

$$X_1 = \frac{R_{th}}{2\alpha R_{e0} I_{1,rms}^2} + \frac{R_{th}}{12} \left[\eta^2 + \frac{1}{2} \right] + \frac{R_{th}/48}{1 + 4(\omega_H \tau/10)^2} + \eta^2 \frac{R_{th}/6}{1 + (\omega_H \tau/10)^2} \quad (4-21a)$$

$$Y_1 = -\frac{(R_{th}/24)(\omega_H \tau/10)}{1 + 4(\omega_H \tau/10)^2} - \eta^2 \frac{(R_{th}/6)(\omega_H \tau/10)}{1 + (\omega_H \tau/10)^2} \quad (4-21b)$$

Equations (4-14), (4-21a), and (4-21b) will be used as the main model to fit the experimental in-phase and out-of-phase data. Using the value obtained from the experimental data for R_{th} along with the knowledge of the geometry of the test platelet, the thermal conductivity of the Cd_3As_2 platelet can be calculated using Eq. (4-20).

Finally, we need to address the distinction between using a current source and a voltage source. All the above-derived equations are valid under the assumption that the current source at 1ω is ideal. In practice; however, in the case of Cd_3As_2 platelets, since the resistance of the sample is generally small compared with that of the rest of the circuit, it is more convenient to use a voltage source, such as a function generator or the sine wave output of a lock-in amplifier, rather than an ideal current source.

4.2 Experimental procedure

A 4-probe single wire (SW) setup was used as illustrated in Fig. 4-1, to perform thermal conductivity measurements based on 1ω – approach. The schematic of the experimental setup is shown in Fig. 4-2. A Stanford Research Systems SR810 lock-in amplifier was used to measure

the 1st harmonic signal across the sample. The sine-out voltage output of the lock-in amplifier was used to provide the 1ω -driving signal. A 10Ω Vishay Dale precision resistor was used to measure amplitude of the 1ω current. No dc offset was necessary, hence $\eta = 0$.

The sample was mounted in a Janis closet-cycle cryostat and the temperature was kept stable at 300 K. The measurements were done in the vacuum of $\sim 10^{-4}$ Torr to minimize the convection losses. The cryostat features heat shielding surfaces which help keep the radiation losses at minimum. Furthermore, a care was taken to reduce thermal conduction losses by using small diameter Au/Ni wires (Aldrich 326526-500MG). The selected Cd_3As_2 platelet for the SW setup was a $4\text{mm}\times 2\text{mm}\times 100\mu\text{m}$ with approximately a rectangular cross section. The IV measurements showed a resistance of $R_{e0} \approx 3\Omega$ for the platelet. A 4-probe electrode pattern was prepared with the help of laser metal cutting system and the platelet was placed on top of the electrodes with the help of In. The temperature coefficient of resistivity (TCR) α was determined by obtaining the IV plots at several temperatures 300K, 305K, 310K, 315K.

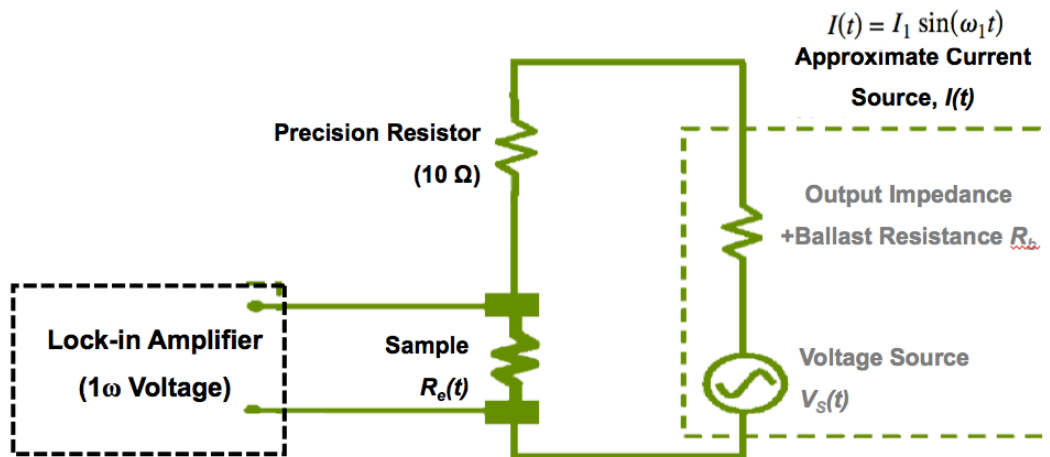


Figure 4-2. The diagram of the experimental setup for measuring the 1ω voltage. A voltage source was used to approximate a current source.

The lock-in amplifier gain was kept constant when sweeping frequency to avoid absolute errors between the various gain settings. All the line filters were turned off and the dc coupling was selected for the measurements. The 1ω voltage was recorded at each frequency in the frequency range of 0.1-100 Hz. To verify the measurement method and the experiment setup, a 6mm-long platinum wire (99.99% purity, $R_{e0} \approx 2 \Omega$) with a known thermal conductivity ($k \approx 71.4 \text{ W/mK}$) was used as a test sample.

4.3 Results and Discussion

The electrical transfer functions at 1ω was measured at constant current while sweeping the frequency. As lower frequencies required longer thermal diffusion time and hence longer settling time, the lowest frequency used was 1 Hz. The output signal was the 1ω voltage, $V_{1\omega,rms}$. Using Eq. (4-14) combined with the theoretical transfer functions given by (4-21a) and (4-21b), and factoring in zero dc offset, the in-phase ($V_{X1\omega,rms}$) and out-of-phase components ($V_{Y1\omega,rms}$) of $V_{1\omega,rms}$ would become:

$$V_{X1\omega,rms} = 2\alpha R_{e0}^2 I_{1,rms}^3 \left[\frac{R_{th}}{2\alpha R_{e0} I_{1,rms}^2} + \frac{R_{th}}{24} + \frac{R_{th}/48}{1 + 4(\omega_H \tau / 10)^2} \right] \quad (4-22a)$$

$$V_{Y1\omega,rms} = 2\alpha R_{e0}^2 I_{1,rms}^3 \left[-\frac{(R_{th}/24)(\omega_H \tau / 10)}{1 + 4(\omega_H \tau / 10)^2} \right] \quad (4-22b)$$

These equations were used to fit the experimental data. The thermal conductivity of the sample was then calculated by plugging experimental value for R_{th} in Eq. (4-20). The data collection was automated using a GUI interface based on MATLAB, and the data analysis was performed in

OriginLab v7.5 software.

As mentioned above, in order to verify the experimental setup, a piece of platinum wire was used as the test sample. The experimental results (points) and their fit to the theoretical equations (solid line) are presented in Fig. 4-3. The thermal conductivity of the platinum wire was then calculated to be ~ 66.7 W/mK. This value falls within $\sim 6\%$ of the value given in the literature for the thermal conductivity of platinum of 71.4 W/mK,²⁹.

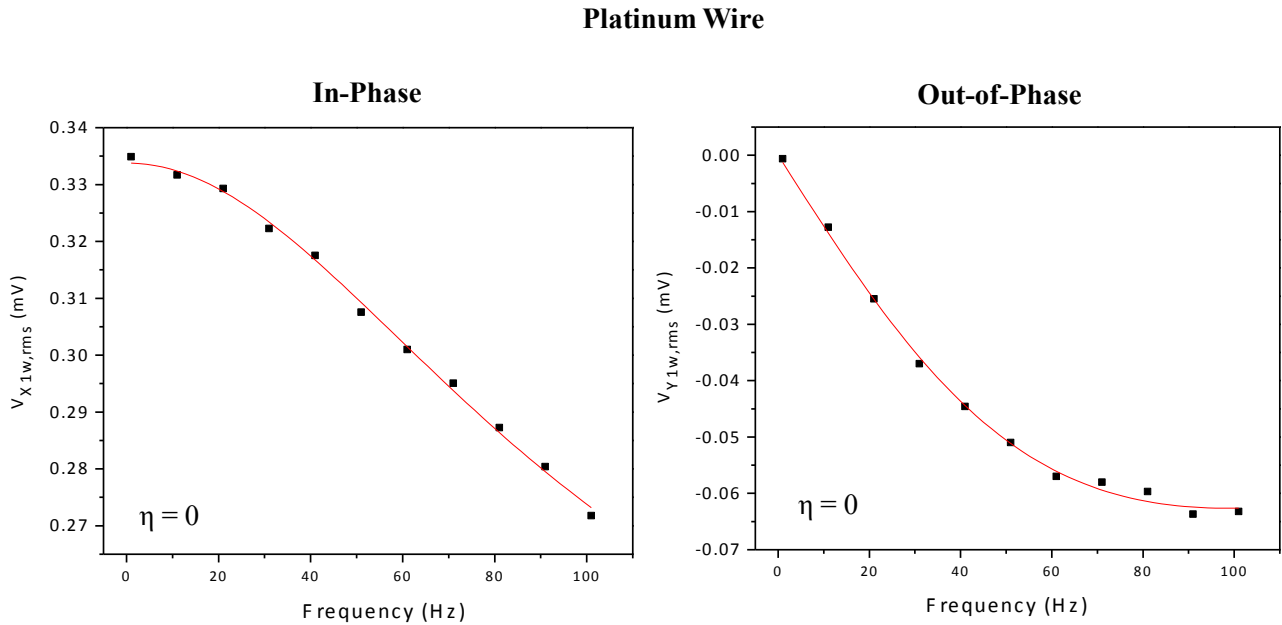


Figure 4-3. The 1ω voltage across the platinum wire sample in a suspended wire (SW) configuration. The solid lines are the theoretical solution obtained from the best approximation to the actual transfer function, and the points are the experimental data at 300 K. From this data, the value of the thermal conductivity of Platinum wire calculated to be ~ 66.7 W/mK, compared with the literature reported value of 71.4 W/mK.

Having confirmed the method and the experimental setup for the 1ω measurements, the Cd_3As_2 sample was prepared for thermal conductivity measurements. Before discussing the experimental conditions and the results for the Cd_3As_2 sample, we first examine the reported values for the thermal conductivity of Cd_3As_2 .

According to previous studies³⁵, at $T > 100$ K, thermal conductivity of single crystal platelets

exhibits only a weak, linear-like increase with T that can be closely approximated with by the following empirical equation

$$k = 0.75 + 2 \frac{T}{1000} \quad [W/mK] \quad (4-23)$$

Earlier, Armitage et al.³⁶ obtained a factor of 2–6 larger thermal conductivities for their polycrystalline ingots of Cd₃As₂ produced via a directional freezing, with average $k \approx 3.4 \pm 2.0$ W/mK at ~300 K, whereas the largest reported k was ~8.0 W/mK. On the other hand, lattice thermal conductivity as low as $\approx 0.3\text{--}0.4$ W/Km (amorphous limit) was reported by Spitzer³⁶ for undoped and doped Cd₃As₂, which was linked to a presence of lattice defects in the anion sublattice, in particular As-vacancy. In another recent study, Zhang et al.³² reported a thermal conductivity of 4.17 W/mK for Cd₃As₂ grown by a self-flux method.

To measure the thermal conductivity of the Cd₃As₂ platelet, the sample was mounted on the 4-probe SW module and placed in the vacuum chamber while the temperature was maintained at 300K. The 1ω voltage across the platelet was collected at each frequency between 1-100Hz. Fig. 4-4 presents the collected data (points) and the theoretical fit to the experimental data (solid line) for the Cd₃As₂ platelet.

Crystalline Cd_3As_2

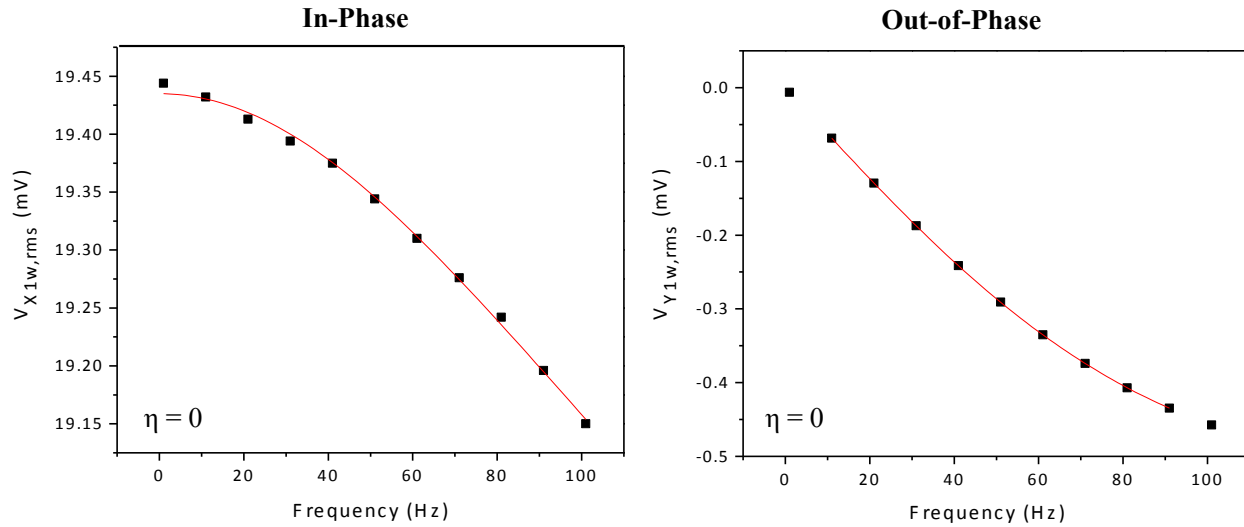


Figure 4-4. The 1ω voltage across the Cd_3As_2 sample in a suspended wire (SW) configuration. The solid lines are the theoretical solution obtained from the best approximation to the actual transfer function, and the points are the experimental data at 300 K. From this data, the value of the thermal conductivity of Cd_3As_2 platelet calculated to ~ 2.4 W/mK. This value is well within the range reported in literature for thermal conductivity of crystalline Cd_3As_2 .

Using equations (4-20), (4-22a), and (4-22b), the thermal conductivity of the Cd_3As_2 sample calculated to be ~ 2.4 W/mK, which falls well into the reported range for k of Cd_3As_2 , and it is comparable to the k of commercially available bulk TE generators based on Bi_2Te_3 ,^{37,38} and PbTe .

39-41

This result confirms that despite the high electron mobility and large power-factor discussed in chapter 3, the thermal conductivity of Cd_3As_2 anomalously stays near the amorphous range around the room temperature. Such properties favorably contribute to achieving a high figure of merit, ZT in this material.

4.4 ZT assessment for crystalline Cd₃As₂

To estimate ZT using the thermal conductivity obtained by the 1ω method, we assumed the thermal conductivity is constant with temperature over the measurements range. This would add a ± 0.2 W/m.K error to the measurements. For a more conservative ZT evaluation, we can consider the largest thermal conductivity, i.e. $k \approx 8.0$, reported so far in previous studies for Cd₃As₂, W/m.K. Using $ZT = \frac{S^2\sigma}{\kappa}$, as demonstrated in Fig. 4-5, the calculations for both platelets A and B yields peak ZT of at least ≈ 3.4 and 0.1 , respectively.

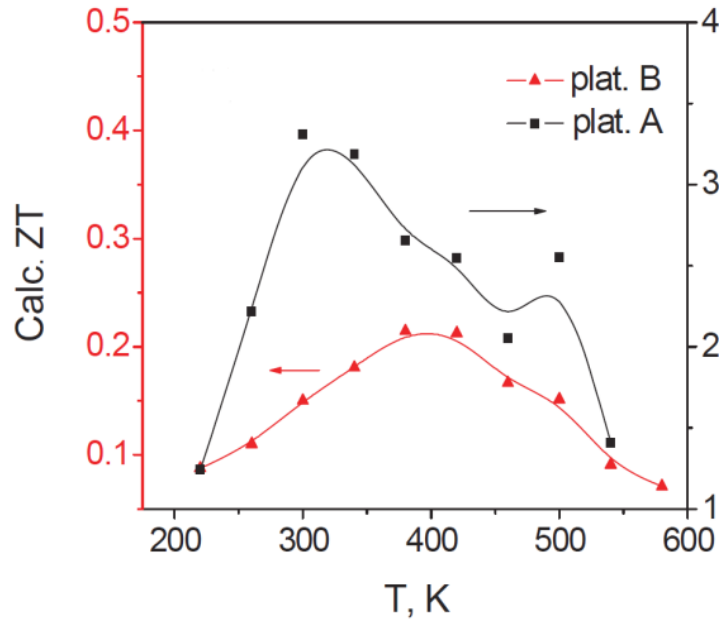


Figure 4-5. ZT versus T plot for platelets A and B considering a conservative thermal conductivity of $k \approx 8.0$ W/Km based on previous studies. The ZT peaks for platelets A and B are around ~ 3.4 and ~ 0.2 respectively.

It should be also noted that in case of tetragonal crystals, the thermal conductivity is to be anisotropic, yet the difference in the measured values of thermal conductivity for different directions is reportedly not to exceed $\approx 10\%$.³⁰ Also, as it is evident from Fig. 4-5 and Fig. 4-6, due to a stronger dependence of ZT on S ($ZT \sim S^2$) and with σ and k showing only a weak

dependence on T, similar to S, the peak ZT expectedly appears within the same low-temperature range of $\approx 300\text{--}400$ K for our samples.

It is further useful to point out that the kink on the right shoulder of the ZT plot, which is more pronounced for platelet A in Fig. 4-6, is similar to that of the S plot discussed in chapter 3. This shoulder peak that appears at ~ 500 K, similar to S and σ , can be attributed to an increase in the electron mobility as a result of the first, $\alpha \rightarrow \alpha'$ phase transition in Cd_3As_2 .

References

1. Tritt, T. M. & Weston, D. Measurement Techniques and Considerations for Determining Thermal Conductivity of Bulk Materials. in *Thermal Conductivity* (ed. Tritt, T. M.) 187–203 (Springer US, 2004). doi:10.1007/0-387-26017-X_8
2. Borca-Tasciuc, T. & Chen, G. Experimental Techniques for Thin-Film Thermal Conductivity Characterization. in *Thermal Conductivity* (ed. Tritt, T. M.) 205–237 (Springer US, 2004). doi:10.1007/0-387-26017-X_9
3. Healy, J. J., de Groot, J. J. & Kestin, J. The theory of the transient hot-wire method for measuring thermal conductivity. *Phys. BC* **82**, 392–408 (1976).
4. Franco, A. An apparatus for the routine measurement of thermal conductivity of materials for building application based on a transient hot-wire method. *Appl. Therm. Eng.* **27**, 2495–2504 (2007).
5. Xie, H., Gu, H., Fujii, M. & Zhang, X. Short hot wire technique for measuring thermal conductivity and thermal diffusivity of various materials. *Meas. Sci. Technol.* **17**, 208 (2006).
6. Reiter, M. & Hartman, H. A new steady-state method for determining thermal conductivity. *J. Geophys. Res.* **76**, 7047–7051 (1971).
7. Beck, A. A steady state method for the rapid measurement of the thermal conductivity of rocks. *J. Sci. Instrum.* **34**, 186 (1957).
8. A simple differential steady-state method to measure the thermal conductivity of solid bulk materials with high accuracy. *Rev. Sci. Instrum.* **85**, 025108 (2014).
9. Mehling, H. *et al.* Thermal Diffusivity of Semitransparent Materials Determined by the Laser-Flash Method Applying a New Analytical Model. *Int. J. Thermophys.* **19**, 941–949 (1998).

10. Corbin, S. F. & Turriff, D. M. Thermal Diffusivity by The Laser Flash Technique. in *Characterization of Materials* (John Wiley & Sons, Inc., 2002). doi:10.1002/0471266965.com102.pub2
11. Nunes dos Santos, W., Mummery, P. & Wallwork, A. Thermal diffusivity of polymers by the laser flash technique. *Polym. Test.* **24**, 628–634 (2005).
12. Transient plane source techniques for thermal conductivity and thermal diffusivity measurements of solid materials. *Rev. Sci. Instrum.* **62**, 797–804 (1991).
13. Li, Y. *et al.* Improving the accuracy of the transient plane source method by correcting probe heat capacity and resistance influences. *Meas. Sci. Technol.* **25**, 015006 (2014).
14. Al-Ajlan, S. A. Measurements of thermal properties of insulation materials by using transient plane source technique. *Appl. Therm. Eng.* **26**, 2184–2191 (2006).
15. Wang, H. & Sen, M. Analysis of the 3-omega method for thermal conductivity measurement. *Int. J. Heat Mass Transf.* **52**, 2102–2109 (2009).
16. Kim, D. J. *et al.* Measurement of Thermal Conductivity of TiO₂ Thin Films Using 3 ω Method. *Int. J. Thermophys.* **25**, 281–289 (2004).
17. Femtosecond pump–probe nondestructive examination of materials (invited). *Rev. Sci. Instrum.* **74**, 400–406 (2003).
18. Analysis of heat flow in layered structures for time-domain thermoreflectance. *Rev. Sci. Instrum.* **75**, 5119–5122 (2004).
19. Schmidt, A. J. PUMP-PROBE THERMOREFLECTANCE. *Annu. Rev. Heat Transf.* **16**, 159–181 (2013).
20. Balandin, A. A. *et al.* Superior Thermal Conductivity of Single-Layer Graphene. *Nano Lett.* **8**, 902–907 (2008).
21. Li, Q., Liu, C., Wang, X. & Fan, S. Measuring the thermal conductivity of individual carbon nanotubes by the Raman shift method. *Nanotechnology* **20**, 145702 (2009).
22. Dames, C. MEASURING THE THERMAL CONDUCTIVITY OF THIN FILMS: 3 OMEGA AND RELATED ELECTROTHERMAL METHODS. *Annu. Rev. Heat Transf.* **16**, 7–49 (2013).
23. Zhao, D., Qian, X., Gu, X., Jajja, S. A. & Yang, R. Measurement Techniques for Thermal Conductivity and Interfacial Thermal Conductance of Bulk and Thin Film Materials. *J. Electron. Packag.* **138**, 040802 (2016).
24. Tong, T. W. *Thermal Conductivity 22*. (CRC Press, 1994).
25. A 3 omega method to measure an arbitrary anisotropic thermal conductivity tensor. *Rev. Sci. Instrum.* **86**, 054902 (2015).
26. Thermal conductivity measurement from 30 to 750 K: the 3 ω method. *Rev. Sci. Instrum.* **61**, 802–808 (1990).
27. 1 ω , 2 ω , and 3 ω methods for measurements of thermal properties. *Rev. Sci. Instrum.* **76**, 124902 (2005).

28. 3ω method for specific heat and thermal conductivity measurements. *Rev. Sci. Instrum.* **72**, 2996–3003 (2001).
29. Touloukian, Y. S., Powell, R. W., Ho, C. Y. & Nicolaou, M. C. *Thermophysical Properties of Matter-The TPRC Data Series. Volume 10. Thermal Diffusivity.* (1974).
30. Armitage, D. & Goldsmid, H. J. The thermal conductivity of cadmium arsenide. *J. Phys. C Solid State Phys.* **2**, 2138 (1969).
31. Bartkowski, K., Rafalowicz, J. & Zdanowicz, W. Thermal conductivity and electrical resistivity of cadmium arsenide (Cd_3As_2) in the temperature range 4.2–40 K. *Int. J. Thermophys.* **7**, 765–772 (1986).
32. Zhang, C. *et al.* Unexpected low thermal conductivity and large power factor in Dirac semimetal Cd_3As_2 . *Chin. Phys. B* **25**, 017202 (2016).
33. Anomalous Thermal Conductivity of Cd_3As_2 and the Cd_3As_2 – Zn_3As_2 Alloys. *J. Appl. Phys.* **37**, 3795–3801 (1966).
34. Adachi, S. *Properties of Semiconductor Alloys: Group-IV, III-V and II-VI Semiconductors.* (John Wiley & Sons, 2009).
35. Pariari, A., Khan, N., Singha, R., Satpati, B. & Mandal, P. Tuning the scattering mechanism in three-dimensional Dirac semimetal Cd_3As_2 . *Phys. Rev. B* **94**, (2016).
36. Armitage, D. & Goldsmid, H. J. Magneto-Seebeck and Nernst effects in cadmium arsenide. *J. Phys. C Solid State Phys.* **2**, 2389 (1969).
37. Goldsmid, H. J. The Thermal Conductivity of Bismuth Telluride. *Proc. Phys. Soc. Sect. B* **69**, 203 (1956).
38. Satterthwaite, C. B. & Ure, R. W. Electrical and Thermal Properties of Bi_2Te_3 . *Phys. Rev.* **108**, 1164–1170 (1957).
39. Romero, A. H., Gross, E. K. U., Verstraete, M. J. & Hellman, O. Thermal conductivity in PbTe from first principles. *Phys. Rev. B* **91**, 214310 (2015).
40. Finefrock, S. W. *et al.* Measurement of Thermal Conductivity of PbTe Nanocrystal Coated Glass Fibers by the 3ω Method. *Nano Lett.* **13**, 5006–5012 (2013).
41. Beyer, H. *et al.* High thermoelectric figure of merit ZT in PbTe and Bi_2Te_3 -based superlattices by a reduction of the thermal conductivity. *Phys. E Low-Dimens. Syst. Nanostructures* **13**, 965–968 (2002).

Chapter 5.

Summary and Future Work

In this dissertation, we developed a low-T vapor-based method for the synthesis of stoichiometric single crystal Cd_3As_2 platelets. The formation of cm-size platelets of binary Cd_3As_2 was verified by scanning electron microscopy (SEM) images and energy dispersive X-ray spectroscopy (EDS). Raman spectroscopy demonstrated a high crystal quality of the material with several strong bands registered in the frequency range of $<1500\text{ cm}^{-1}$. The high-resolution transmission electron microscopy (HRTEM) confirmed that samples were single crystals with the average lattice spacing of 0.222 nm for the $\{440\}$ type reflections, and a spacing of 0.225 nm for the $\{408\}$ type reflections.

Upon confirming the formation of the crystals, a series of temperature dependent transport and Seebeck measurements were performed on the Cd_3As_2 platelets. The T-dependent I–V tests confirmed an Ohmic-like transport behavior and a monotonically decaying electrical conductance with T consistent with the semimetallic characteristic of the samples. The temperature dependent Seebeck, S measurements showed a high room-temperature thermo-power of up to $\sim 613\text{ uV K}^{-1}$. While the debate on whether Cd_3As_2 has inverted or zero band gap structure continues, the primary pathway of the minority carrier generation in our sample is phonon-assisted interband electronic transitions that likely involve E and A_1 electronic bands.

To further confirm the unexpected TE properties of the Cd_3As_2 platelets, the thermal conductivity of the Cd_3As_2 platelet was measured using the 1ω method at 300K. The resultant k was calculated to be $\sim 2.4\text{ W/m.K}$ in the confirmation that the thermal conductivity of Cd_3As_2 crystals is to approach the amorphous limit at the room temperature.

With combined high room-temperature thermo-powers of up to $\sim 613\text{ }\mu\text{VK}^{-1}$, high electrical

conductivity, and amorphous limit thermal conductivity of ~ 2.41 W/m.K, bulk Cd_3As_2 is identified as another, highly promising phonon-glass electron-crystal type TE material for application in a low-T high efficiency thermoelectric generators and refrigerators operating under normal conditions.

The research presented in this dissertation sets the ground for further investigation in TE properties of crystalline Cd_3As_2 . For example, it would be worthwhile to investigate the TE properties of nano-engineered composites of Cd_3As_2 and ordinary semiconductors such as Zn_3As_2 . In such composites, the vast phonon scattering at the interfaces between nano-particles or between the two constituents would further reduce the thermal conductivity while the presence of topological surface states and the bulk Dirac cones in Cd_3As_2 ensures excellent electrical conductivity, giving rise to improved ZT around room temperature, and subsequently, a high thermoelectric efficiency.

Another possibility would be the study of TE properties upon doping Cd_3As_2 with ferromagnetic materials such as Fe or Cr. It is known that in diluted magnetic semiconductors (DMSCs), the emergence of ferromagnetism as a result of the indirect exchange interaction of magnetic ions has good prospects in applications for controlling various properties of semiconductors including the thermoelectric properties with the help of a magnetic field¹. For example, it has been shown that doping of Bi_2Te_3 with iron increases the Seebeck coefficient of this material².

Finally, as discussed in chapter 3, the Cd_3As_2 crystals grown in this work are n-type whereas a thermoelectric generator module will need two types of TE materials, n-type and p-type that are electrically in series but thermally in parallel. The ZT of the whole TEG module will depend on

the ZT of each constituent material; hence, building a high performance TE generator using Cd_3A_2 will also require a high performance p-type TE material such as Bi_2Te_3 and Sb_2Te_3 .

References

1. P. M. Tarasov, V. A. Kulbachinskiĭ, and V. G. Kytin, Thermoelectric Properties and Ferromagnetism of Diluted Magnetic Semiconductors $\text{Sb}_2 - x\text{Cr}_x\text{Te}_3$, *Journal of Experimental and Theoretical Physics*, 2007, 105 (1), 21–26 (2007).
2. T. Jungwirth, Jairo Sinova, J. Maĵek, et al., *Rev. Mod. Phys.* 78, 809 (2006).

CURRICULUM VITAE

Tahereh Hosseini, PhD

<https://www.tahereh-hosseini.com/>

<https://www.linkedin.com/in/taherehosseini/>

Education

- **The University of Wisconsin – Milwaukee**
 - PhD in Electrical Engineering – Nanotechnology, December 2017.
 - Dissertation Title: Synthesis, Transport, and Thermoelectric Studies of Topological Dirac Semimetal Cd_3As_2 For Room Temperature Waste Heat Recovery And Energy Conversion.
 - GPA: 3.92/4.0
 - First UWM graduate student to receive Johnson Controls Inc. 3-year Research Fellowship.
 - **The University of Wisconsin – Milwaukee**
 - M.S. in Electrical Engineering – Nanotechnology, August 2012.
 - Thesis Title: Photoluminescence and Transport Characteristics of MEH-PPV Encapsulated Single-Walled Carbon Nanotube Films Synthesized By Unstable Micellization.
 - GPA: 3.87/4.0
 - **Tehran Polytechnic University– Tehran, Iran**
 - B.S. in Electrical Engineering
 - GPA: 3.2/4.0
-

Research Interests

- Development of novel nanomaterials/devices for energy conversion, energy harvesting, low-power electronics, biosensors.
 - Process development, nanofabrication and nanopatterning technologies, including self-assembly for device fabrication.
 - Emerging materials for energy conversion and sensing (e.g. Excitonics, topological materials).
 - Photonic Crystals for enhanced energy conversion and biomedical applications.
 - Flexible substrates for electronics, sensors, and energy conversion platforms.
 - Thin-film transistors.
 - Compound semiconductors, e.g. III-V, II-VI, for electronics and optoelectronics.
 - Nonvolatile memory.
-

Academic, Leadership, & Professional Experience

Research Experience

- **Nanotechnology Research Laboratory, The University of Wisconsin – Milwaukee**
- Graduate Researcher, 2011 – Present
- **Select research projects:**
 - Transient reflectance of photoexcited topological Dirac semimetal Cd_3As_2 .

- Low-T CVD-synthesis of topological Dirac semimetal Cd₃As₂ platelets.
- Investigating the thermal conductivity of crystalline Cd₃As₂ using a model based on the general transfer function (1 ω method).
- T-dependent transport and thermopower study of crystalline Cd₃As₂.
- Synthesis, Spectroscopic and Photoconduction Characteristics of MEH-PPV/SWCNT Films with Ohmic-like Transport Attributes.
- Transport and photoconduction characteristics of metal-graphene-4H-SiC (0001) heterojunction devices.
- CVD Growth and characterization of GeSbTe nanowires for phase change memory applications.
- Concrete Embedded Dye-Synthesized Photovoltaic Solar Cell.
- Fabrication and investigation of photoconduction properties of ZnO nano-wires grown by CVD-VLS route.
- Optical, Electrical, and Structural Properties of CdSe_{1-x}S_x/ZnS alloyed quantum dots.
- Thermo-electrical Characterization Of Semiconductor-Graphene Thin Films.
- Electrical and Optical Characterization of SiC-graphene FET.
- Thin film growth and characterization of TiO₂ and Cd₃As₂.
- Cleanroom fabrication of MOSFET & GaAs laser. Included photolithography, mask alignment, dry and wet etch.

Teaching Experience

- **The University of Wisconsin – Milwaukee**
- Instructor/Teaching Assistant, Department of Electrical Engineering, Fall Semesters 2011-2014.
 - Hybrid Nano-materials and Nano-devices.
 - Fabrication and characterization of dye-sensitized solar cell (DSSC).
 - Fabrication and photoconduction study of ZNO nanowires.
 - Advanced Material Characterizations
 - FTIR Spectroscopy; Raman Spectroscopy.
 - Fundamentals of Electrical Engineering.

Leadership Experience

- **The UWM Research Foundation**, The University of Wisconsin-Milwaukee
- Graduate Student Ambassador, 2012-2015
 - Organized Graduate Students Research Presentation quarterly events for multidisciplinary research presentation.
 - Organized visits to companies and industrial sites for graduate students.

Professional Experience

- **Johnson Controls Inc., Core Design Components & Subs**, Milwaukee, WI.
 - Engineering Graduate Intern, Summer 2014
 - Successfully completed lead-acid battery grid optimization to save cost while maintaining the battery performance.
 - Diagnostic optical investigation and troubleshooting of Absorbed Glass Mat (AGM) batteries.
- **SiTime Corporation, MEMS Development Group**, Santa Clara, CA
 - MEMS Engineering Intern, Summer 2016

- Provided MEMS resonator characterizations and process control monitor (PCM).
- Received recognition for negotiating vendor terms that produced significant budget saving for a low-budget proposal to upgrade the existing wafer probing system for through silicon NIR imaging.

Technical Skills

Synthesis & Fabrication:

- Chemical Vapor Deposition (CVD)
- Vacuum Sputtering
- Cleanroom Fabrication
- Photolithography
- E-Beam lithography
- ALD

- Photoluminescence Spectroscopy (PL)
- Scanning Electron Microscopy (SEM)
- Energy-dispersive X-ray Spectroscopy
- FTIR spectroscopy
- UV-Vis spectroscopy
- AFM

Characterization:

- Transport measurements/analysis
- Nano-scale Device Testing
- XRD
- Raman spectroscopy

Data Analysis and Programming:

- MATLAB, Python, OriginLab, Design of Experiment (DOE), Minitab, COMSOL

Areas of Expertise

- Development of novel nanomaterials for sensing and energy conversion applications
- Nanofabrication
- Semiconductor Processing & characterization
- Device physics
- Optoelectronics

Awards and Recognitions

- Johnson Controls Inc. 3-year Research Fellowship
- UWM Student Startup Challenge Winner for Architecture Information Modeling
- Scheinfeld Entrepreneurial Award
- Chancellor's Graduate Student Award
- New Venture Business Plan Competition

Publications

(9 peer reviewed journal articles, 1 book chapter)

- N.Yavarishad, T.Hosseini, E. Kheirandish, C.P.Weber, N. Kouklin, Room-temperature self-powered photo-detector based on the optically- induced Seebeck effect in Cd3As2 crystals, Applied Physic Express, 10(5), 052201, (2017).
- T. Hosseini, N. Yavarishad, J.Alward, N. Kouklin, M. Gajdardziska-Josifovska, "Large Thermopower, Crystalline Cd3As2 by Low Temperature Vapor Deposition for Room Temperature Waste Heat Recovery", Adv. Electron. Mater., 2 (1), 1500319, (2016).

- C. P. Weber, Ernest Arushanov, Bryan S. Berggren, Tahereh Hosseini, Nikolai Kouklin, and Alex Nateprov, "Transient reflectance of photoexcited Cd₃As₂", Applied Physics Letters, 106, 231904, (2015).
- T. Hosseini, D. Tomer, S. Rajput, L. Li, N. Kouklin, "Transport and photoconductive characteristics of metal-graphene-4H-SiC (0001) heterojunction devices", Applied Physics Letters, 105, 223107 (2014).
- T.Hosseini, N. Kouklin, "On plasmon-induced photocurrent and doping of metal-patterned graphene", Applied Physics Letters 105, 043104 (2014).
- T.Hosseini, N. Kouklin, "Synthesis and Spectroscopic and Photoconduction Characteristics of Coaxial Poly [2-methoxy-5-(20-ethylhexyloxy)21,4-phenylene vinylene] Single-Walled Carbon Nanotube Films with Ohmic-like Transport Attributes", J. APPL. POLYM. SCI., 400291-6, (2014).
- T. Hosseini, I. Flores-Vivian, K. Sobolev & N. Kouklin, "Concrete Embedded Dye-Synthesized Photovoltaic Solar Cell", Nature Scientific Report, 3: 2727 (2013).
- Hosseini T., Omari. M, Kouklin N., "Carbon Nanotube IR Photothermovoltaic Devices: Power, Fill Factor, and Transient Response", IEEE Electron Device Letters, 34, 7, 924-926 (2013).
- M. Omari, T. Hosseini, N. Kouklin, "Investigation of time-rated defect formation, infrared absorption and transport characteristics of single-walled carbon nanotubes wet-processed in phosphoric acid", NANO, 7, 4 1250026 (2012).
- **Book Chapter:**
- T. Hosseini, N. Kouklin (2016), "Carbon Nanotubes Polymer Composites: Properties and Photovoltaic Applications", In: M. Berber (Ed), "Carbon Nanotubes - Current Progress of their Polymer Composites", InTech, ISBN 978-953-51-4689-6

Presentations & Talks

- T. Hosseini, "Monolithic Concrete-based solar cell", The 5th International Symposium of Nanotechnology in Construction (NICOM 5), Chicago, IL, USA, 2015.
- T. Hosseini, Annual Research Presentation, IEEE Student Organization, UWM, May 2017.
- T. Hosseini, "Power Generation Technologies and Their Efficiency: A Comparative Study", Johnson Controls Inc., March 2016
- T. Hosseini, Graduate Students Talks, UWM Research Foundation, October 2017.
- T. Hosseini, Graduate Research Poster presentation, April 2014